Nanoindentation of YSZ-Alumina Ceramic Thin Films Grown by Combustion Chemical Vapor Deposition

A Dissertation
Presented to
the Academic Faculty

by

David Walter Stollberg

In Partial Fulfillment
of the Requirements of the Degree
Doctor of Philosophy
in Materials Science and Engineering

Georgia Institute of Technology

May 2000

Nanoindentation of YSZ-Alumina Ceramic Thin Films Grown by Combustion Chemical Vapor Deposition

APPROVED:

_____
W. B. Carter, Advisor

_____
J. M. Hampikian, Advisor

_____
J. K. Cochran, Jr.

_____
A. Saxena

_____
K. Breder

Date Approved_____

Acknowledgments

This research was sponsored by the U.S. Department of Energy under Cooperative Agreement No. DE-FC21-92MC29061. Additional support from the Assistant Secretary for Energy Efficiency and Renewable Energy, Office of Transportation Technologies, as part of the High Temperature Materials Laboratory User Program, Oak Ridge National Laboratory, managed by Lockheed Martin Energy Research Corp. for the U.S. Department of Energy, under contract number DE-AC05-96OR22464.

Special thanks to Laura Riester for her invaluable help with the Nanoindenter®. Thanks go to the Georgia Tech Microscopy Center for use of the electron microscopes and especially to Yolande Berta for her never ending help with the microscopes. And thanks to my dissertation committee members: Drs. Ashok Saxena, Joe K. Cochran and Kristin Breder for their time and insight during the preparation of my thesis.

I am also very grateful for my advisors Drs. W. Brent Carter and Janet M. Hampikian for their continuous guidance, help and encouragement throughout my career at Georgia Tech.

Many friends at Georgia Tech have made this whole experience more enjoyable, in particular Jud Ready, Carter Hamilton and Greg Book. Special thanks to Dan Chiang and Todd Polley for their friendship and extra efforts in daily distractions (which includes but

is not limited to basketball, lunches, epic trips and golf). I can't say too many good things about those guys. And thanks to Steve Russ, who I believe single-handedly got me to pass the qualifying exam.

Extra special thanks to Todd Polley, for being an exceptional person, labmate and friend; we did so many different things there in Bunger-Henry 115 and around Georgia Tech and Atlanta and had so much fun, it is truly amazing. I believe I had the greatest job I could ever have working at Tech with Todd for the last four years.

I also thank wholeheartedly my newest family of friends in the drum corps for the fun, friendship and musical outlet which had been so absent in my life for many years; particular recognition goes to Noel and Jonathan Thomas and, of course, Ken Huff.

The following individuals have always provided me with great friendship and encouragement for many, many years; I thank them from the bottom of my heart for always being there: Craig Carper, Joe Sardina, Dale Sutherland and Roy VanMeter. I also thank my great friend Alan Frantz for his great wit and friendship over the years.

Special recognition goes to Kathryn Pace for her friendship and for her help and encouragement with many different things over the last year or so. And I'd like to also mention Darrell Turner, a great friend and soul who is gone too soon, but who I will never forget.

Lastly, I thank my mother, father and brother for their unconditional support, encouragement and love.

Table of Contents

Approval ii

Acknowledgments iii

Table of Contents v

List of Tables viii

List of Figures ix

Summary xv

CHAPTER

I. INTRODUCTION 1

II. BACKGROUND 6

Film Deposition 6

Combustion CVD 6

Evolution of Combustion CVD 8

Similar Flame Techniques 11

CVD Film Growth 12

Yttria Stabilized Zirconia-Alumina 17

Nanoindenter® 22

Microhardness 23

Elastic Modulus 32

Fracture Toughness 35

III. EXPERIMENTAL PROCEDURE 41

Combustion CVD Deposition Apparatus 41

Deposition Parameters 43

Temperature 43

Solution Concentration 44

Substrates 44

Film Materials 44

Film thickness 44

YSZ-alumina Components 45

Repeatability Study 47

Characterization 48

Mechanical Properties Measurements 49
Microhardness 49
Elastic Modulus 50
Fracture Toughness 51
IV. RESULTS 53
Deposition Parameters 53
Characterization 53
Scanning Electron Microscopy 53
X-ray Diffraction 64
Residual Stress 66
Film Stress 66
Matrix Stress 67
Transmission Electron Microscopy 70
Energy Dispersive Spectroscopy 74
Quantitative Image Analysis 76
Nanoindentation 79
Bulk Material Specimens 80
YSZ-alumina 86
Data from Indents 86
Solution Concentration 88
Repeatability Study 91
Anneal Series 94
Compositional Study 95
Confidence in Fracture Toughness Data 100
V. DISCUSSION 107
Primary Goal 107
Deposition Parameters 107
Characterization 109
Scanning Electron Microscopy 109
Film Thickness 109
Anneal Series 110
X-ray Diffraction 113
Residual Stress 115
Film Stress 115
Matrix Stress 116
Transmission Electron Microscopy 116
Energy Dispersive Spectroscopy 118
Quantitative Image analysis 119
Nanoindentation 120
Bulk Material Specimens 120

YSZ-Alumina Films 122
Data from Indents 122
Elastic Modulus/Hardness Ratio 124
Solution Concentration 124
Fracture Toughness Crack Analysis 125
Repeatability Study 128
Anneal Series 129
Hardness and Elastic Modulus 130
Fracture Toughness 134
VI. FRACTURE TOUGHNESS MODELING 136
Phase Transformation Toughening 139
Microcracking 139
Crack Deflection 140
Residual Stress 151
Compositional Study 154
Uniform Particle Size and Spacing 154
Measured Particle Size and Spacing 157
Anneal Series 159
Grain Bridging 160
Anneal Series 161
Compositional Study 163
Model Total 165
Anneal Series 165
Compositional Study 168
VII. CONCLUSIONS 173
VIII. RECOMMENDATIONS FOR FUTURE WORK 177

REFERENCES 179

Vita 186

List of Tables

Table 1: Deposition Parameters 45

Table 2: Film Deposition Rates 56

Table 3: Material Properties 67

Table 4: Film Stress Determined by CTE Mismatch 69

Table 5: TEM-EDS Quantitative Analysis 75

Table 6: Film Composition and Particle Size 77

Table 7: Eutectic Composition Anneal Series: Particle size and Area/Volume Percentage 77

Table 8: Bulk Materials Tested with Nanoindentation. 80

Table 9: 100% YSZ Fracture Toughness Repeatability Comparison Chart 105

Table 10: 30 mol% Alumina Fracture Toughness Repeatability Comparison Chart . . 105

Table 11: Compositional Study Fracture Toughness Comparison Chart 106

Table 12: Effect of Yttria Content on Zirconia Lattice Parameters 114

Table 13: Bulk Materials Mechanical Properties, Nanoindentation and Literature . . . 121

Table 14: Comparison of 100% YSZ and 30 mol% Alumina Fracture Toughness . . . 129

Table 15: Properties and Parameters Used in the Model 166

List of Figures

Figure 1 Gaseous Fuel Combustion CVD System. 8

Figure 2 Liquid Fuel Combustion CVD System. 9

Figure 3 OCN (Oscillating Capillary Nebulizer) 10

Figure 4 High Performance Combustion CVD Nozzle. 11

Figure 5 Surface Energy of Deposition. 13

Figure 6 Types of Island Coalescence: a) Ostwald ripening, b) sintering and c) cluster migration. 17

Figure 7 Low Mol% $YO_{1.5}$ YSZ Phase Diagram 19

Figure 8 Schematic of the Nanoindenter®. 22

Figure 9 Load vs. Displacement Curve from Nanoindenter®. 26

Figure 10 Schematic of indentation in a material. 27

Figure 11 SEM micrograph in plan view of an indentation in a film made with a Berkovich indenter. 28

Figure 12 Radius of Curvature of Stylus 29

Figure 13 Indentation and Crack Measurement. 37

Figure 14 Schematic of indentation showing plastic zone and radial crack. 38

Figure 15 Plot showing plastic zone size, b, to cavity radius r_0 ratio versus modulus to hardness ratio for several materials. 38

Figure 16 Combustion CVD Schematic. 41

Figure 17 Apparatus for Suspending Substrate in Flame. 42

Figure 18 Alumina-Zirconia Phase Diagram. 46

Figure 19 Indentation matrix for hardness and elastic modulus measurements. 50

Figure 20 Indentation Matrix for Fracture Toughness Measurements. 51

Figure 21 SEM micrographs of YSZ-alumina films, plan-views (left image) and cross-sections (right image): a) 100% YSZ, b) 15 mol% Al_2O_3, c) 30 mol% Al_2O_3, d) 45 mol% Al_2O_3, e) 62.8 mol% Al_2O_3, f) 80 mol% Al_2O_3, and g) 100 mol% Al_2O_3. 54

Figure 22 SEM micrographs of YSZ-alumina films, secondary (left image) and backscatter electron (right image) images; a) 15 mol% Al_2O_3, b) 30 mol% Al_2O_3, c) 45 mol% Al_2O_3, d) 62.8 mol% Al_2O_3, and e) 80 mol% Al_2O_3. . . . 58

Figure 23 SEM micrographs of YSZ-62.8mol% Al_2O_3 films deposited at a) 1550EC and b) 1650EC flame temperature. 60

Figure 24 SEM micrographs of YSZ-62.8mol% Al_2O_3 films annealed at 1500EC for a) 0 hrs, b) 2.5 hrs, c) 5 hrs and d) 10 hrs. 61

Figure 25 Particle sizes for 62.8 mol% Al_2O_3 anneal series. 62

Figure 26 Nearest neighbor distances for 62.8 mol% Al_2O_3 anneal series. 63

Figure 27 APD x-ray diffraction pattern of a 62.8 mol% Al_2O_3 film deposited onto amorphous silica. 64

Figure 28 APD x-ray diffraction pattern of a 100% YSZ film deposited onto a-plane alumina. 65

Figure 29 Film stress due to substrate/film CTE mismatch versus Al_2O_3 content in films. 68

Figure 30 Film stress due to matrix/second phase CTE mismatch versus Al_2O_3 content in films. 70

Figure 31 TEM brightfield image of 62.8 mol% alumina film showing 10 nm to 20 nm sized YSZ particles (dark) in an alumina matrix (light). 72

Figure 32 TEM electron diffraction pattern for 62.8 mol% alumina film. 73

Figure 33 TEM electron diffraction pattern, [$\bar{1}11$] zone axis for YSZ in the films. 73

Figure 34 TEM EDS spectrum for 62.8mol% Al_2O_3 film. 74

Figure 35 High angle tilt SEM image of 62.8mol% Al_2O_3 film with 10hr anneal showing the growth of the YSZ particles out of the plane of the matrix. 78

Figure 36 Hardness and elastic modulus for various substrates and substrate orientation: a) and b) comparison of different materials, c) and d) display of repeatability of tests and e) and f) comparison of three orientations on one material. 82

Figure 37 Indentations in substrates: a) a-plane Al_2O_3, b) r-plane Al_2O_3, c) polycrystalline Al_2O_3, d) MgO, e) amorphous SiO_2 and f) YSZ. 85

Figure 38 Fracture toughness for various substrates. 85

Figure 39 'Good' load-displacement curve showing a smooth increase then decrease in the load with displacement of the indenter tip. 86

Figure 40 'Bad' load-displacement curve showing plateaus of indenter displacement without an increase in load. 87

Figure 41 'Bad' load-displacement curve showing erratic behavior possibly due to slippages of the indenter tip on a rough surface or discontinuities in the film. 88

Figure 42 SEM micrograph of 100% YSZ film deposited with solution concentrations of a) 0.002M and b) 0.005M, and a 30 mol% Al_2O_3 film deposited with solution concentrations of c) 0.002M and d) 0.005M. 89

Figure 43 Hardness, elastic modulus and fracture toughness for 0.002M and 0.005M solution concentration films. 90

Figure 44 Hardness, elastic modulus and fracture toughness for 100% YSZ films. . . . 92

Figure 45 Hardness, elastic modulus and fracture toughness for 30mol% Al_2O_3 films. 93

Figure 46 Fracture toughness of 1500EC annealed series of 62.8 mol% Al_2O_3 films. . 94

Figure 47 SEM micrographs of cube-corner indentations in YSZ-alumina films; a) 100% YSZ, b) 15 mol% Al_2O_3, c) 30 mol% Al_2O_3, d) 45 mol% Al_2O_3, e) 62.8 mol% Al_2O_3, f) 80 mol% Al_2O_3, and g) 100 mol% Al_2O_3. 96

Figure 48 Hardness and elastic modulus vs indentation depth for entire compositional range studied. 98

Figure 49 Hardness and elastic modulus vs the Al_2O_3 amount in the film for entire compositional range studied. 99

Figure 50 Fracture toughness vs the Al_2O_3 amount in the film for entire compositional range studied. 100

Figure 51 Histograms showing frequency of indentations with certain fracture toughness for each Al_2O_3 composition. 101

Figure 52 1500EC anneal series coarsening rate plot, particle radius, r^n versus anneal time, t. 112

Figure 53 1500EC anneal series logarithmic plot of particle radius, r, versus anneal time, t. 112

Figure 54 SEM micrograph showing lateral cracking and delaminating of the film. 126

Figure 55 SEM micrograph showing short crack that does not extend past the plastic zone. 127

Figure 56 Fracture toughness versus the nearest neighbor distance for the 1500EC annealed series of 62.8 mol% Al_2O_3 films 130

Figure 57 Fracture toughness versus indent load for several YSZ-Al_2O_3 films 136

Figure 58 SEM micrograph of a 62.8 mol% Al_2O_3 annealed film showing a) the arresting of a crack at a second phase particle and b) a crack propagating through a second phase particle. 141

Figure 59 SEM micrograph showing the deflection of cracks about second phase particles; a) 62.8 mol% Al_2O_3 film and b) 30 mol% Al_2O_3 film. 142

Figure 60 Schematic of typical crack deflection; top: tilt, and bottom: twist of the crack front. 145

Figure 61 Schematic of two spheres showing top: minium twist and bottom: maximum twist of the crack. 145

Figure 62 Crack deflection model showing relative toughness versus volume percent Al_2O_3 for both a uniform and distributed spacing. 150

Figure 63 Incremental toughening versus volume percent Al_2O_3 for both a uniform and distributed spacing. 150

Figure 64 Model of matrix stress incremental fracture toughness versus volume percent Al_2O_3 (balance YSZ) for a range of particle sizes. 154

Figure 65 Schematic of stress regions in the matrix and the second phase particles and their immediate vicinity: a) high Al_2O_3 content and b) low Al_2O_3 content 155

Figure 66 Model of film stress incremental fracture toughness versus volume percent Al_2O_3 (balance YSZ) for a range of particle sizes 156

Figure 67 Total incremental fracture toughness of matrix stress and film stress versus volume percent Al_2O_3 (balance YSZ) for a range of particle sizes 157

Figure 68 Model of incremental fracture toughness of matrix stress, film stress and their sum versus volume percent Al_2O_3 (balance YSZ) for measured particle sizes and spacings. 158

Figure 69 Model of incremental fracture toughness of matrix stress, film stress and their sum versus particle size for the 1500EC anneal series of 62.8 mol% Al_2O_3. 159

Figure 70 Schematic of the grain bridging toughening mechanism, where the crack is held together by the second phase particle or friction between the particle and the matrix. 160

Figure 71 Model of incremental fracture toughness of grain bridging versus particle size for the 1500EC anneal series of 62.8 mol% Al_2O_3. 162

Figure 72 Model of incremental fracture toughness of grain bridging versus volume percent Al_2O_3 for various uniform particle sizes. 163

Figure 73 Model of incremental fracture toughness of grain bridging versus volume percent Al_2O_3 for measured particle sizes. 164

Figure 74 Total model of incremental fracture toughness versus particle size for the 1500EC anneal series of 62.8 mol% Al_2O_3. 166

Figure 75 Total model of incremental fracture toughness and measured fracture toughness versus particle size for the 1500EC anneal series of 62.8 mol% Al_2O_3. 167

Figure 76 Total incremental fracture toughness model and measured toughening versus volume percent Al_2O_3 for uniform particle sizes and spacings with uniform spacing crack deflection model. 168

Figure 77 Total incremental fracture toughness model and measured toughening versus volume percent Al_2O_3 for uniform particle sizes and distributed spacing. 169

Figure 78 Total incremental fracture toughness model and measured toughening versus volume percent Al_2O_3 for measured particle sizes and spacings with the uniform-spacing crack deflection model. 170

Figure 79 Total incremental fracture toughness model and measured toughening versus volume percent Al_2O_3 for measured particle sizes and spacings with the distributed-spacing crack deflection model. 170

Figure 80 Total incremental fracture toughness model and measured toughening versus volume percent Al_2O_3 for measured particle sizes and spacings with the distributed-spacing crack deflection model (0-50 vol%) and the uniform-spacing crack deflection model (50-100 vol%). 172

Summary

Combustion chemical vapor deposition (combustion CVD) is a thin film deposition process that uses a flame created by the ignition of an aerosol containing precursors dissolved in a flammable solvent. Combustion CVD is a relatively new technique for creating thin film oxide coatings. Combustion CVD has been successfully used to deposit high quality thin oxide films for potential applications such as thermal barrier coatings, dielectric thin films, composite interlayer coatings, etc. The present work involved developing the optimum parameters for deposition of thin films of yttria-stabilized zirconia (YSZ), alumina (Al_2O_3), and YSZ-alumina composites followed by a determination of the mechanical properties of the films (measured using nanoindentation) as a function of composition.

The optimized parameters for deposition of YSZ, alumina, and YSZ-alumina composites onto single crystal a-plane alumina involved using an organic liquid as the flammable solvent and Y 2-ethylhexanoate, Zr 2-ethylhexanoate and Al acetylacetonate as the metal precursors at a 0.002 M concentration delivered at 4 ml/min at flame temperatures of 1550EC and substrate temperatures of 1050EC. The resulting films were grown with deposition rates of ~ 1.5 μm/hr.

Measurement of the mechanical properties (hardness, elastic modulus and fracture toughness) of the films was performed using a mechanical properties microprobe called

the Nanoindenter®. In order to obtain valid results from nanoindentation, the combustion CVD films were optimized for minimum surface roughness and grown to a thickness of approximately 0.8 μm. With the penetration depth of the indenter at approximately 150 nm, the 800 nm thickness of the film made influences of the substrate on the measurements negligible.

The hardnesses and elastic moduli of the YSZ-alumina films did not vary with the composition of the film. The fracture toughness, however, did show a dependence on the composition. It was found that second phase particles of alumina grown into a YSZ matrix increased the fracture toughness of the films (on average, 1.76 $MPa \cdot m^{0.5}$ for 100% YSZ to 2.49 $MPa \cdot m^{0.5}$ for 70 mol% YSZ/30 mol% alumina). Similarly, second phase particles of YSZ grown into an alumina matrix also increased the fracture toughness (on average, 2.20 $MPa \cdot m^{0.5}$ for 100% alumina to 2.45 $MPa \cdot m^{0.5}$ for 37.2 mol% YSZ/62.8 mol% alumina).

Modeling of the fracture toughness of the YSZ-alumina films was successfully achieved by using the following toughening mechanisms: crack deflection from the second phase particles, grain bridging around the particles, and residual stress from the CTE mismatch between the film and the substrate and between the second phase particles and the matrix of the film.

CHAPTER I

INTRODUCTION

The research presented in this dissertation studied the mechanical properties of ceramic thin films grown by combustion chemical vapor deposition (combustion CVD). Combustion chemical vapor deposition is a relatively new technique for creating thin film coatings. In comparison to conventional CVD, combustion CVD is an open air, flame-assisted, coating process that requires no reaction/vacuum chamber. Combustion CVD has been successfully used over the past several years to deposit high quality thin oxide films for potential applications in thermal barrier coatings, dielectric thin films, composite interlayer coatings, etc. Various ceramic materials have been deposited including: yttrium barium cuprate, yttria-stabilized zirconia, ceria, barium titanate, alumina, silica, lanthanum phosphate, magnesium spinel and nickel spinel. Now that the process has been developed to the point of producing quality films of several materials, more research is necessary to understand the deposition process and to quantify the quality of the films.

The mechanical properties of thin ceramic films are very important. The fracture toughness of a material is related to the amount of stress the material can withstand with an existing crack without failing. For thin films, failure is usually defined as the point

when spallation or delamination occurs. The formation of a crack is one of the most common processes leading to failure. The toughness of a thin film ceramic is thus a key mechanical property to study and control.

Increasingly harder films have been sought for applications in electronic, optical and heavy wear environments. The hardness of a material is now a common defining factor in materials selection. In metals Hall-Petch [1] has shown hardness to be a function of the intrinsic hardness of a single grain and the grain size. The hardness of ceramic films, however, was found to be a function of more than just those two variables [2]. Examination of the hardness of ceramic films may lead to some important property relationships and possibly the prediction of other film characteristics such as residual stress.

Young's modulus, or the elastic modulus, of thin ceramic films is another significant mechanical property. The modulus indicates how compliant or flexible a material will be under stress or strain. Therefore, knowing the modulus of a material to be used in a particular application is important to the engineer in predicting the performance of the material.

All of these mechanical properties (fracture toughness, hardness and elastic modulus) are important in terms of evaluating the potential performance for bulk materials, and are particularly important for films prepared by combustion CVD.

Combustion CVD grown films of yttria-stabilized zirconia (Y_2O_3 stabilized ZrO_2 or YSZ), alumina (Al_2O_3) and YSZ-alumina thin films were developed for applications with the thermal barrier coatings (TBC's) used in the hot regions of gas turbine engines. In order to increase the efficiency and extend the life of the engine, additional coatings are being studied to reduce or eliminate failure of TBC's. It is hypothesized that inserting a tough ceramic film under the TBC layer (between the ceramic top coat and bond coat) may help increase service life of the TBC and the engine. Combustion CVD films of YSZ, alumina and YSZ-alumina combustion CVD films were studied here because they are tough ceramics, stable at high temperature and can be readily deposited onto turbine blade components.

YSZ, in general, is a widely studied material because of its high toughness, high bending strength and low thermal conductivity. Plasma-sprayed and electron beam YSZ coatings are used extensively as TBC's. It is known that YSZ's mechanical properties, such as toughness and strength, degrade with low temperature aging (423 to 673K) particularly in environments containing water vapor [3, 4, 5, 6, 7]. This degradation results in crack formation due to the partial transformation of the YSZ from the tetragonal phase to the monoclinic phase and a decrease in strength. Additions of alumina to YSZ have been shown to prevent this low temperature degradation. In other words, additions of alumina to YSZ provide an increase in fracture toughness even though the fracture toughness of alumina may be lower than that of YSZ [3, 8]. This toughened composite

for bulk materials provides the impetus to study potential toughening in YSZ-alumina composite combustion CVD thin films.

The deposition process for YSZ-alumina films was first developed and optimized before the evaluation of turbine components with combustion CVD YSZ-alumina films. This was accomplished by varying the many process parameters used in the combustion CVD technique, such as temperature, precursor solvent, precursor concentration, aerosol size, precursor flowrate, oxidizer flowrate and others. The fine adjustments of these numerous parameters are necessary to provide the highest quality film based on morphology, phase, composition, deposition rate, etc.

The determination of the toughest composition of YSZ and alumina thin films is difficult due to the small dimensions. The indenter must be of a small size and load such that only the film properties are measured; no substrate influences included. To accomplish fracture toughness measurement, along with hardness and elastic modulus measurements, the Nanoindenter® located at the High Temperature Materials Laboratory of Oak Ridge National Laboratory in Oak Ridge, TN was used. Nanoindentation is an indentation technique similar to that of bulk hardness testers, except that its load ranges are on the millinewton scale and its indentation depths are on the micron and nanometer scale. This range of loads and depths permits the evaluation of the mechanical properties of a materials' surface on the microscopic scale. With nanoindentation, one is able to confidently test very small specimens of material such as microchips, specific grains of

materials and, in the case of this research, combustion CVD thin films.

To determine the feasibility and reliability of nanoindentation for thin films and to develop the nanoindentation testing technique, specimens of various bulk materials were tested along with the combustion CVD grown YSZ-alumina thin films. Bulk ceramics examined were silica (amorphous SiO_2), zirconia (fully stabilized 9.5mol% Y_2O_3-ZrO_2), alumina (polycrystalline, r-plane and a-plane single crystal Al_2O_3) and magnesium oxide (single crystal MgO). Nanoindentation is a growing area of research, however, review of the literature contains little on the nanoindentation of thin films. The research presented in this dissertation is some of the first work in this field.

The main objectives of this research were the following:

- Develop and optimize the deposition of YSZ, alumina and YSZ-alumina via combustion CVD.
- Determine the feasibility of nanoindentation for determining the fracture toughness, hardness and elastic modulus of combustion CVD thin films.
- If practical, quantify the fracture toughness, hardness and elastic modulus of combustion CVD YSZ-alumina composite films.

CHAPTER II

BACKGROUND

Film Deposition

Combustion CVD

Combustion chemical vapor deposition (combustion CVD) is an open air, flame-assisted, coating process that employs an aerosol to transport coating precursors (chemical compounds containing the desired coating constituents) to the deposition region [9, 10]. In liquid fuel combustion CVD (see below), which was used for this research, the coating precursors are first dissolved in an organic solvent which is then atomized and combusted to provide the energy necessary for chemical reactions to occur. The precursors react within the flame and form a coating on a substrate held in or near the flame. The experimental procedure, Chapter III, details the setup for the combustion CVD process.

Combustion CVD is used to deposit thin oxide films. The process has shown promise for the deposition of oxides that are thermodynamically stable at high temperatures. Over the past few years, the combustion CVD process has been explored as a deposition technique for use in thermal barrier coatings, dielectric thin films, composite interlayer coatings, and many more applications. Many different ceramic films have been

deposited successfully including: yttrium barium cuprate ($YBa_2Cu_3O_x$), yttria stabilized zirconia (Y_2O_3-stabilized ZrO_2), ceria (CeO_2), barium titanate ($BaTiO_3$), alumina (Al_2O_3), silica (SiO_2), lanthanum phosphate ($LaPO_4$), magnesium spinel ($MgAl_2O_4$) and nickel spinel ($NiAl_2O_4$) [10, 11, 12, 13, 14, 15].

In conventional CVD processing, gases carrying coating constituents flow into a reaction vessel where deposition onto a heated substrate occurs. Depositions may be conducted at atmospheric or reduced pressure. Both cold and hot wall reaction chambers may be used. Heat can be provided by a resistance furnace, RF induction, or high-intensity radiation lamps. Plasma, microwave, photon, RF and electron-enhanced CVD processes have also been developed [2]. In contrast to these methods, for combustion CVD, a flame provides the heat and the environment necessary for vapor phase deposition and provides an excess of oxygen for the oxidation of the metals to be deposited.

A major difference between combustion CVD and conventional CVD is the elimination of the need for a reaction/vacuum chamber which is required in conventional CVD. Combustion CVD is performed in the open atmosphere. The deposition process is controlled by managing several variables: substrate temperature, precursor concentration, precursor composition, aerosol size distribution, solvent composition and the apparatus setup geometry.

Evolution of Combustion CVD

The design of the combustion CVD process has evolved over the last few years. There are two different basic types of systems: gaseous fuel and liquid fuel. In the gaseous fuel system, the metal precursors are dissolved into either an aqueous or organic solution and fed into a chamber. The solution is then atomized with a high velocity gas such as O_2, N_2, Ar, or air followed by a particle discriminator to remove large droplets of liquid. A flammable gas (such as methane) is introduced at the exit of the chamber and mixes with the atomized precursor solution. As this gas mixture flows out of the chamber, the Venturi effect draws outside air into the mix. The final mixture passes through the burner and is then ignited. Figure 1 shows the setup of this system.

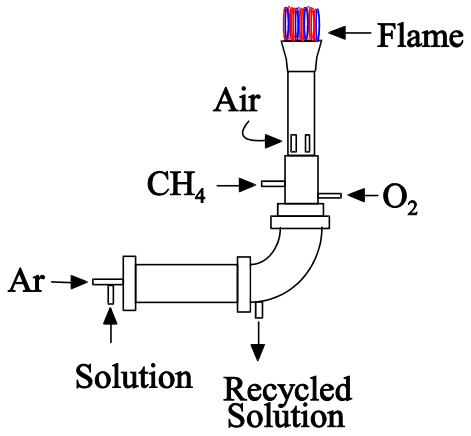

Figure 1 Gaseous Fuel Combustion CVD System.

In the liquid fuel system, the metal precursors are dissolved into an organic solution which is then fed through a nozzle and atomized. As the atomized solution exits the nozzle, oxygen or air is added and the mixture is ignited by a pilot flame. The oxygen added just prior to the pilot flame ensures the complete combustion of the atomized flammable solution. Figure 2 shows this system setup.

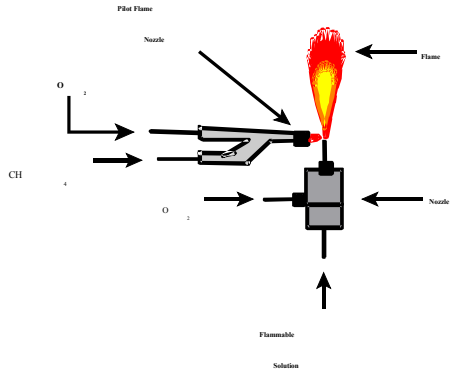

Figure 2 Liquid Fuel Combustion CVD System.

The first extensively used combustion CVD nozzle was a liquid fuel type pneumatic nebulizer involving a tube for the flammable precursor liquid positioned 90E to a separate tube supplied with high velocity oxygen with the ends of the two tubes positioned close to one another. The oxygen not only aided in complete combustion but also atomized the liquid. The atomized liquid was then ignited by a pilot flame. After several studies, it was found that smaller aerosol droplet sizes emitted from the nozzle tended to produce better films [16]. Improvements were made to the setup to create

increasingly finer aerosol droplets. The development of the oscillating capillary nebulizer (OCN) nozzle by Wang [17] allowed some control of aerosol size distribution. Figure 3 shows this nozzle in detail.

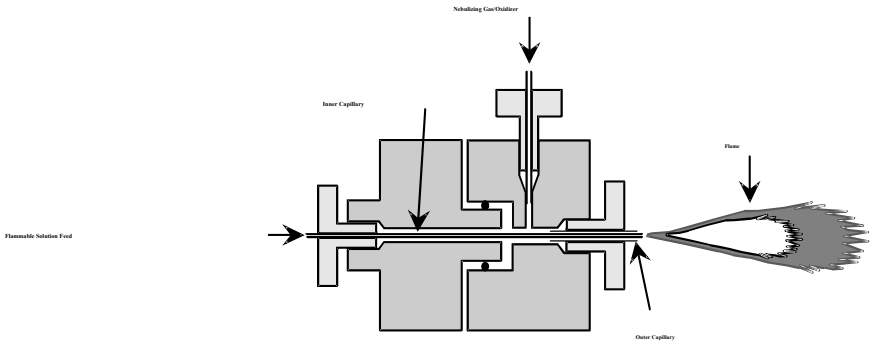

Figure 3 OCN (Oscillating Capillary Nebulizer) after Wang [17].

As the figure shows, the OCN consists of two concentric capillary tubes (made of silica) where the flammable liquid flows through the inner capillary and the oxygen flows through the space between the inner and outer capillaries. The high velocity oxygen causes the capillary tubes to oscillate at a high frequency which atomizes the liquid prior to ignition. By changing various parameters in this nozzle, such as the size of the capillary tubes, the relative positions of the ends of the tubes, and the flow rates of oxygen and precursor, the droplet aerosol sizes can be optimized. This method of aerosol production gave much finer aerosol droplet sizes than the original 90E nozzle. The OCN has been used heavily in creating combustion CVD films in the laboratory over the last few years.

A new, improved proprietary nebulizer design is now being employed in the laboratory and was the used for all the depositions in this research, see Figure 4.

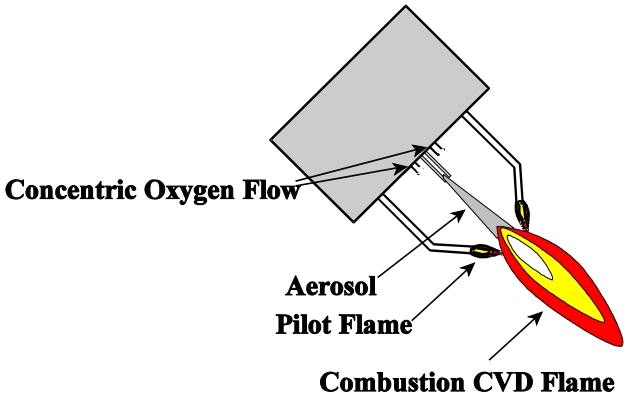

Figure 4 High Performance Combustion CVD Nozzle.

Similar Flame Techniques

The basic premise behind combustion CVD, utilization of a flame for deposition, is not completely new. Koguchi et al. [18] used a flame pyrolysis method for deposition of $YBa_2Cu_3O_X$ on a substrate of yttria stabilized zirconia. In their method the precursors are dissolved in distilled water, agitated in a supersonic vibrator and then carried to the hydrogen/oxygen flame with nitrogen gas. Just prior to the flame, the aerosol is passed through a cylindrical mist separator to remove large droplets. This technique has a problem with substrate cooling due to the high heat of vaporization of the water, but it is successful in producing superconducting films.

Another technique similar to combustion CVD is called "flaming solvent spray," and was used by McHale et al. [19]. Depositions of films of $YBa_2Cu_3O_X$ and

$Bi_7Pb_{0.3}Sr_2Ca_2Cu_3O_{10}$ were made onto MgO substrates. Precursors were dissolved in either ethanol, ethylene glycol or liquid ammonia and sprayed via a Pyrex air atomizing nozzle, using a natural gas burner for ignition. This technique does not have the substrate cooling problem of the previously described method. The major differences between combustion CVD and these other techniques are that combustion CVD uses a new nebulizing method, lower precursor concentrations and lower precursor solution flowrates.

CVD Film Growth

The theory film formation from vaporous material applies to combustion CVD. Heterogeneous nucleation to form a solid film on a planar surface is one of the better descriptions of film formation. Capillarity theory gives a simple qualitative model. In this model, atoms in the vapor phase impinge upon the surface of the substrate and either create film clusters that grow (nucleate) on the surface, or leave the surface due to dissociation processes. For a portion of film to begin to form, the change in chemical free energy per unit volume, ΔG_V, must be equal to or greater than the change in free energy of formation for the film, ΔG. The nuclei which have formed on the surface are assumed to have the shape of a spherical cap with its surface free energies per unit area, γ_{vf}, γ_{fs} and γ_{sv} (erg/m^2 or Joule/m^2) minimized. The subscript *vf* denotes the interfacial surface energy between the film and vapor. Similarly the subscript *fs* refers to the interfacial surface energy between the film and the surface of the substrate and *sv* indicates the

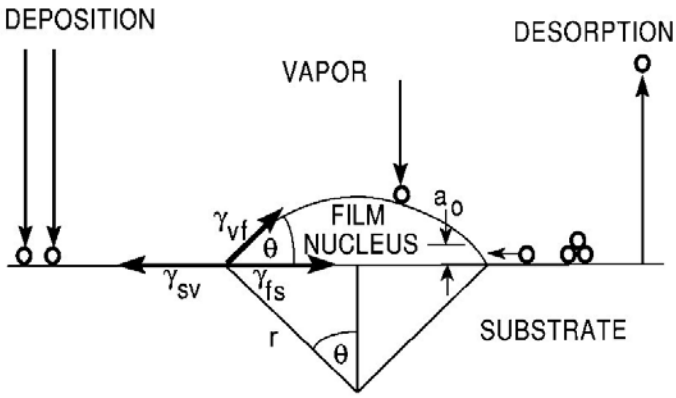

Figure 5 Surface Energy of Deposition.

interfacial surface energy between the surface of the substrate and the vapor. Figure 5 shows a nucleating particle and the surface free energies involved. With the radius of the spherical cap nucleus of film on the surface given by *r*, the following equation represents the free energy balance [2]:

$$\Delta G = a_3 r^3 \Delta G_V + a_1 r^2 \gamma_{vf} + a_2 r^2 \gamma_{fs} - a_2 r^2 \gamma_{sv} \qquad (1)$$

where a_1, a_2 and a_3 are geometric constants for a spherical shaped nucleus,

$a_1 = 2\pi(1 - \cos\theta)$,

$a_2 = \pi \sin^3\theta$,

and $a_3 = \pi(2 - 3\cos\theta + \cos^3\theta)/3$.

The critical radius, r^* (meter), for which a nucleated particle will continue growing is found by setting $\frac{d\Delta G}{dr} = 0$ from equation (1).

$$r^* = \frac{-2\left(a_1\gamma_{vf} + a_2\gamma_{fs} + a_2\gamma_{sv}\right)}{3a_3\Delta G_V} \tag{2}$$

Substituting r^* into equation (1) gives the critical free energy, ΔG^* (Joule):

$$\Delta G^* = \frac{4\left(a_1\gamma_{vf} + a_2\gamma_{fs} - a_2\gamma_{sv}\right)^3}{27a_3^2\Delta G_V^2} \tag{3}$$

For $r \geq r^*$, the nucleus lowers its free energy by increasing in size and thus growth proceeds. These equations determine the critical size for a new particle on the surface to continue growing, but they do not yield information regarding the rate of nucleation. The nucleation rate of particles on the surface of the substrate is also an important factor in film formation and it can be derived starting from the gas impingement flux, Φ (moles/cm^2-sec), of molecules hitting a surface:

$$\Phi = \frac{N_A P}{\sqrt{2\pi MRT}} \tag{4}$$

where P = vapor pressure (Pa),

M = molecular weight (g/mol),

N_A = Avogadro's number (mol^{-1}),

R = Universal gas constant (J/mol-K),

and T = source temperature (K).

After hitting the surface, atoms can either desorb or diffuse around on the surface. The atoms which remain attached to the surface are termed adatoms. The desorption rate, ν ($cm^{-2}sec^{-1}$), follows an Arrhenius dependency,

$$\nu \propto \exp\frac{-E_{des}}{kT} \tag{5}$$

where E_{des} (Joule) is the activation energy for desorption.

By making substitutions in accordance with Ohring's [2] derivation, the nucleation rate of particles on the surface of the substrate is,

$$\dot{N} = 2\pi r^{*} a_0 \sin\theta \frac{PN_A}{\sqrt{2\pi MRT}} n_S \exp\frac{E_{des} - E_S - \Delta G^{*}}{kT} \quad (\text{nuclei} / \text{cm}^2 - \text{sec}) \cdot \tag{6}$$

where a_0 = the atomic dimension (m),

P = pressure (Pa),

M= molecular weight (g/mol),

and E_s = activation energy for surface diffusion (Joule).

Following nucleation is the growth of the particles. There are three widely recognized modes of nuclei growth: island growth (Vollmer-Weber), layer growth (Frank-van der Merwe) and layer-plus-island (Stranski-Kranstanov). Island growth occurs when the neighboring film atoms bond more to each other than to the substrate. In the layer growth mode, the atoms bond more strongly to the substrate than to each other,

opposite of island growth. The layer growth mode leads to atoms attached all over the substrate and eventually to a single (mono) layer of atoms. The last mode is, as its name states, a combination of island and layer growth.

A balance of the surface energies shown in Figure 4 results in the equation:

$$\gamma_{sv} = \gamma_{fs} + \gamma_{vf} \cos\theta \tag{7}$$

For island growth, $\theta > 0$, so equation (7) becomes:

$$\gamma_{sv} < \gamma_{fs} + \gamma_{vf}. \tag{8}$$

With layer growth, $\theta = 0$, and equation (7) becomes:

$$\gamma_{sv} = \gamma_{fs} + \gamma_{vf}. \tag{9}$$

The island-plus-layer growth mode is a combination of these two.

With progressing island growth, islands will coalesce. There are three different mechanisms of coalescence as shown in Figure 6: a. Ostwald ripening, b. sintering and c. cluster migration. Ostwald ripening involves the transportation of mass from smaller nuclei to larger nuclei. Sintering occurs when surface diffusion takes place between two nuclei in contact with each other and one larger nuclei is formed. The last type of coalescence, cluster migration, results from the random movement, collision and

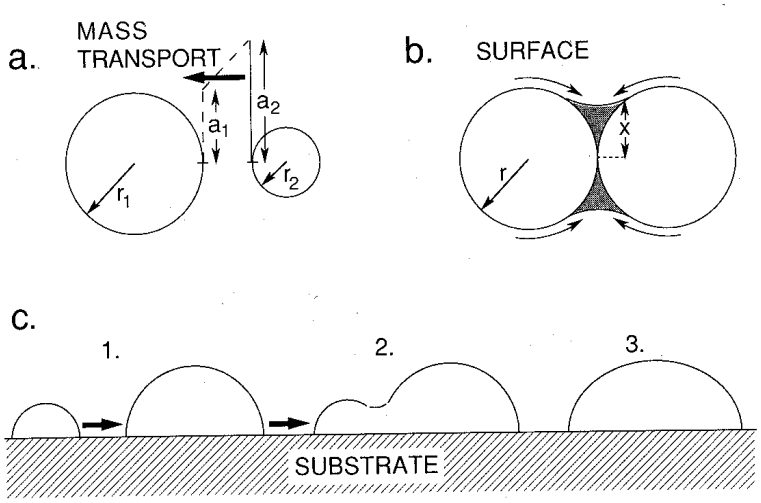

Figure 6 Types of Island Coalescence: a) Ostwald ripening, b) sintering and c) cluster migration. [2]

subsequent joining of nuclei on the surface of the substrate. These three mechanisms combine to coarsen the film's grain structure on the substrate surface [2]. Once the entire surface of the substrate is covered, thickening of the film begins. The foundation of the film's microstructure is formed by these initial coarsened nuclei.

Yttria Stabilized Zirconia-Alumina

Yttria-stabilized zirconia is a material that continues to be greatly studied because of its desirable mechanical and thermal properties. Because of its low thermal conductivity, YSZ has found one of its foremost uses as a thermal barrier in turbine engines, particularly in the hottest regions of the engine. In this location YSZ serves as a coating on turbine blades and vanes and other hot section parts. The thermal protection provided by the YSZ allows the turbine inlet temperature of the engine to be increased on

the order of 80EC to 200EC without an accompanying increase in the temperature of the blades, vanes and other parts coated with YSZ. Higher operating temperatures are desired by engine manufacturers because increased temperatures mean higher efficiencies, resulting in more fuel efficient power production [20]. Much of the following background information involves YSZ formed by sintering powders or by plasma-spray deposition, which is conventionally used in application of thermal barrier coatings.

Zirconia is a very tough and strong ceramic material, particularly in the tetragonal (denoted T) phase which occurs at higher temperatures (>1200EC). However, it undergoes a phase transformation from tetragonal to monoclinic when cooled below ~1200EC [21]. The monoclinic phase is not as strong as the tetragonal phase [22]. This transformation also involves a large volume expansion (~ 3%) [23] because of the larger lattice parameter and the larger crystal lattice of the monoclinic phase compared to the metastable tetragonal phase. This expansion is undesirable due to the stresses produced and the crack initiation and propagation which often results. Stabilizing the zirconia with small additions of other elements, such as yttrium, has been done regularly over the years to prevent this transformation and toughen the material.

Figure 7 shows the phase diagram of the ZrO_2-$YO_{1.5}$ system in the low yttria regime [24]. It can be seen that from ~4 to13 mol% $YO_{1.5}$ (or ~2.0 to 6.5 mol% Y_2O_3) the stable low temperature phase is nontransformable tetragonal, known as TN. The

monoclinic phase is only stable in the very low yttria region, 0 to 4 mol% $YO_{1.5}$ (or 0 to 2 mol% Y_2O_3). On the phase diagram from 0 to 13 mol% $YO_{1.5}$ (or 0 to 6.5 mol% Y_2O_3) the material is called yttria-partially stabilized zirconia (Y-PSZ) or most often simply yttria-stabilized zirconia (YSZ). Above 6.5 mol% $YO_{1.5}$ (or 13 mol% Y_2O_3), the cubic phase is the stable low temperature phase. The material is called fully stabilized zirconia in this region.

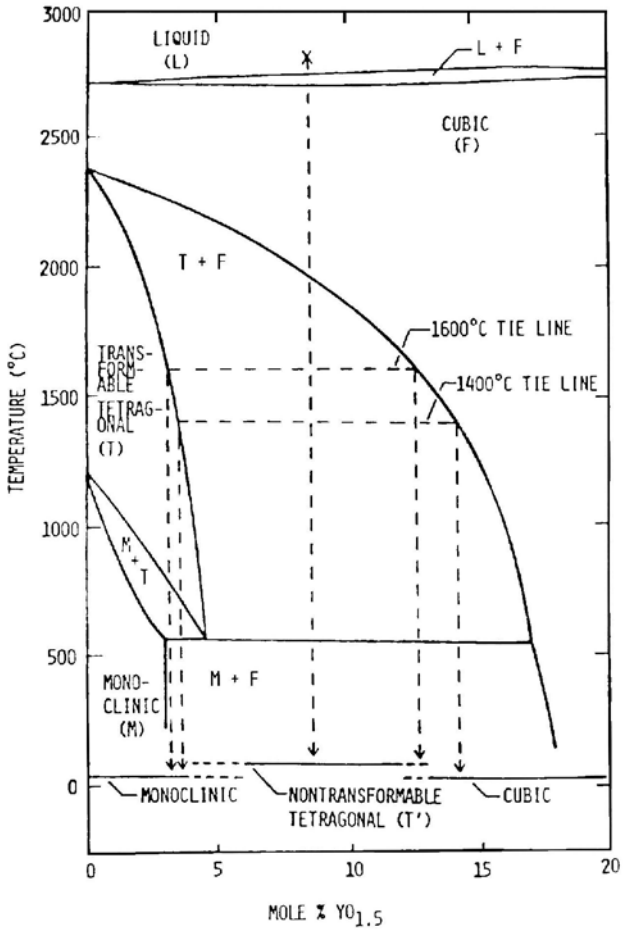

Figure 7 Low Mol% $YO_{1.5}$ YSZ Phase Diagram [6].

It is also known that the tetragonal phase (T) of YSZ will spontaneously transform to the monoclinic phase when a stress is applied [21]. Garvie et al. found that this transformation is accompanied by an increase in strength and fracture toughness [25, 3, 26, 22, 27]. They described the increase in strength as most probably due to an increase in the work of fracture via absorption of energy during the transformation from tetragonal to monoclinic. The increase in fracture toughness, they postulated, is due to the volume change actually suppressing crack growth by internal stresses closing material together about the crack tip [26]. The metastable TN phase does not undergo this stress-induced transformation to the monoclinic phase [28]. This property of the TN phase is highly desired.

Another problem that occurs with YSZ at low temperatures (200-500EC) is degradation of the strength and toughness of the tetragonal phase, TN with time [3, 4, 5, 6, 7]. With the temperature maintained around 200EC for a significant period of time, the tetragonal (TN) phase will transform to the monoclinic phase. This is particularly true in water or water vapor-containing environments. This transformation results in severe cracking and a large reduction in the strength of the material. Numerous researchers, to be discussed below, have worked to minimize this problem by including additives in YSZ. Note that in their research YSZ and YSZ-alumina was formed by sintering from powders of yttria, zirconia and alumina.

Li and Watanabe measured the fracture toughness of YSZ including alumina additions varying from 10-30 vol % [3, 5]. They found that the addition of alumina increased the fracture toughness by 17% to 30% and that the larger the alumina particles, the larger the increase in fracture toughness and strength. Yao-Yong et al. measured the amounts of phases present and the material's mechanical properties upon the addition of 20 wt % Al_2O_3 to YSZ with 2-5 mol % Y_2O_3 [8]. They found that only ~7% monoclinic phase remained after transformation while the Young's modulus increased 28%, hardness increased 22% and fracture toughness increased 25%. Tsubakino and Nozato studied the propagation of the phase transformation from tetragonal to monoclinic into specimen grain interiors during low temperature aging in water for YSZ (3 mol% Y_2O_3) with 1.2 to 12 wt% Al_2O_3 [4]. Their results show that the transformation to monoclinic only takes place near the surface of the grains and is completely suppressed in the interior of the YSZ-alumina sample.

Tsukama and Shimada performed long term aging experiments on YSZ-alumina at 250EC [6]. Their materials ranged in content for Y_2O_3 (2.0-2.6 mol %) and Al_2O_3 (5-40 wt %). They found that increased amounts of Al_2O_3 yielded decreased amounts of the monoclinic phase after the aging, with the 40 wt% Al_2O_3 specimen showing no monoclinic phase. It was also found that there was no decrease in strength of any of the specimens containing Al_2O_3 additions. Sato and Shimada also tested 2-4 mol% YSZ with

0-40 wt% Al_2O_3 in 80-200EC water for extended times and found that the Al_2O_3 additions limited the transformation to the monoclinic phase in all samples [7].

Alumina is a desirable material for use as an additive because of its higher elastic modulus and hardness and lower cost compared to ZrO_2 powders. The fracture toughness of Al_2O_3 is actually lower than that of ZrO_2 but as stated above, additions of Al_2O_3 of up to 30 vol% increase the fracture toughness, increase the strength and reduce or eliminate the amount of monoclinic phase formed in the YSZ after low temperature aging.

Nanoindenter®

The Nanoindenter® (shown in Figure 8 [29]) located at the Oak Ridge National Laboratory's High Temperature Materials Laboratory was used for this research. The Nanoindenter® is a mechanical properties microprobe. It is similar to hardness testing

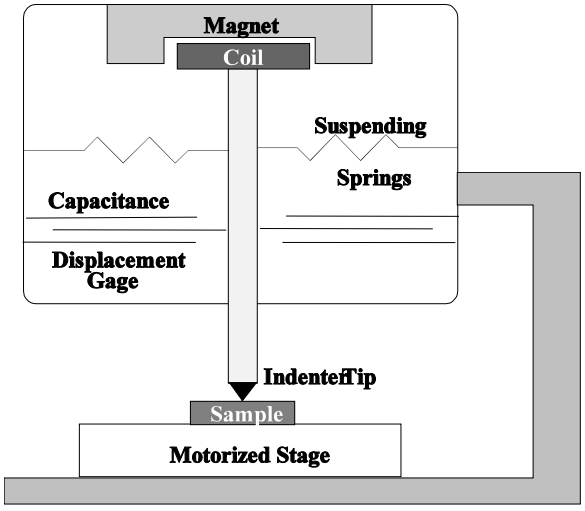

Figure 8 Schematic of the Nanoindenter®.

equipment used for large bulk properties of materials in that it indents materials with a hard, sharp indenter tip. The primary difference between the Nanoindenter® and the common hardness testing machines is that it operates with extremely low loads: millinewtons down to micronewtons. This results in very small penetration depths: microns down to nanometers. It is this advantage of low loads and shallow penetration depths that make the Nanoindenter® an ideal tool for characterizing the mechanical properties of thin films and near-surface regimes of bulk materials. The Nanoindenter® was developed by Oliver et al. [30] at Nano Instruments, Inc. of MTS, Knoxville, TN and is a registered trademark.

Microhardness

Hardness is defined as the resistance of a material to permanent deformation [31]. The hardness of a material is an important mechanical property because it can provide information on elastic and plastic behavior. High hardness is greatly desired in optical and mechanical applications. Larger hardnesses are particularly sought for mechanical applications in which wear resistance and friction are of serious concern.

The hardness of bulk material is often determined via a Knoop or Vickers indentation test. Most versions of these indenters cannot be used for films with thicknesses on the submicron scale, due to high loads causing the indentation depths to exceed the film thicknesses. Smaller indenters, shallower indentations and much lower applied loads are required (along with much more sensitive equipment) to determine the

hardness, or microhardness, of thin films. It was not until the last decade or so that submicron indentation became possible. The development of a microhardness indenter, such as the one used by Pethica, Hutchings and Oliver [30, 32], provided the ability to perform such measurements with adequate accuracy and precision. Indentation depths on the order of tens of nanometers with an indentation width of less than half a micron are achieved with the Nanoindenter®. The resolution of this apparatus is enough so that loads on the order of millinewtons (mN) down to micronewtons (μN) can be applied with indentations less than one micon apart.

The hardness of a material, H (Pa), is defined by the equation:

$$H = P/A \tag{10}$$

where P (N) is the applied load and A(m^2) is the projected area of the indentation after the load is removed. It has been determined that the hardness of metals is a function of the grain size, d, of the material. This relationship is described by the Hall-Petch equation,

$$H = H_0 + kd^{-1/2} \tag{11}$$

where H_0 is the intrinsic hardness for a single crystal, d (m) is the grain size and k ($Pa \cdot m^{0.5}$) is a material constant. Ceramics, on the other hand, do not follow this relationship. The hardness relationship in ceramics is more complex than in metals. In ceramics it is not the size of the grains that is important, but it is the quality of the grains

and grain boundaries that is dominant. Porosity and microcracks also affect the hardness of ceramic materials [2].

While the exact relationships of hardness to other properties of ceramics is not always well known, it is very simple to measure the microhardness. The Nanoindenter® can be used to precisely measure the hardness of very thin films. In order to obtain adequate values of hardness, the depth of the indentation must be small compared to the film thickness. Usually a film thickness 5 to 10 times the indenter depth is sufficient to prevent any substrate influence in the measurement [33]. The Nanoindenter® can have an indentation depth as shallow as ~20 nm and an indentation width as narrow as 500 nm, depending on the particular material being tested. The YSZ-alumina thin films deposited for this research were on the order of 0.5 to1.0 μm thick and the indentation depths were approximately 45 to 200 nm (0.045 to 0.200 μm). The measurements yielding the lower values of this range were not influenced by substrate effects.

The resolution of the Nanoindenter's ® depth measurements is ±0.05 nm. This high resolution is accomplished by the metal disks (capacitance measurement gages) attached to the indenter shaft and the indenter housing. As the indenter is displaced the capacitance in the plates changes, this capacitance change is then calibrated to the displacement depth. Because of the ability to measure very small changes in capacitance, extremely high displacement resolution is achieved.

An indentation is produced by the Nanoindenter® as follows: the sample stage is raised (while the indenter tip remains fixed) until the indenter tip touches the sample. The sample stage is then raised slowly as the applied load on the indenter tip and sample is measured. The displacement of the stage and the applied load are simultaneously and continuously measured, producing a load versus indentation depth plot similar to that shown in Figure 9 [34]. The displacement noted as h_f is the final displacement of the film after complete removal of the load. The value h_p is the effective plastic depth of the indenter in contact with the deforming material while under maximum load. The schematic in Figure 10 [35] defines these dimensions. The applied load can range from 0.25 μN to 120 mN in 0.1 μN increments. The remaining dimension, h_s, represents the elastic recovery of the initial surface of the film.

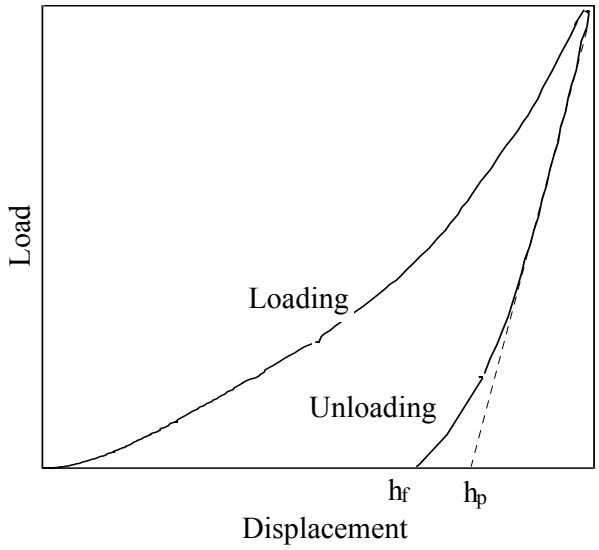

Figure 9 Load vs. Displacement Curve from Nanoindenter®.

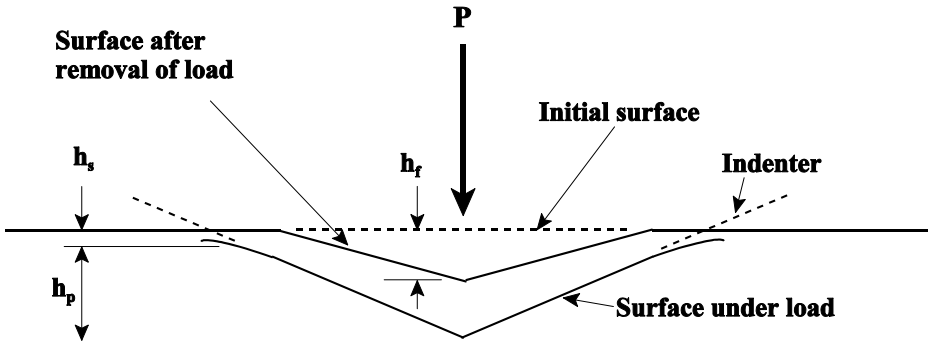

Figure 10 Schematic of indentation in a material.

The total displacement, h, is the sum

$$h = h_p + h_s \ . \tag{12}$$

The stylus used is a diamond, usually with a triangular pyramidal geometry known as the Berkovich indenter. A sample indentation produced from a Berkovich indenter tip is shown in Figure 11 [36]. Calculation of the microhardness is made using equation (10) where the effective contact area, A (m^2), for the Berkovich indenter is

$$A = 27.5h_p^2 \qquad \text{[36]} \tag{13}$$

This area is an ideal value for a perfect indenter tip. Because of non-uniformities and rounding of the indenter tip, Oliver and Pharr [35] developed the following for the area

$$A = 27.5h_p^2 + \sum_{i=0}^{7} C_i h_p^{1/2^{i+1}} \tag{14}$$

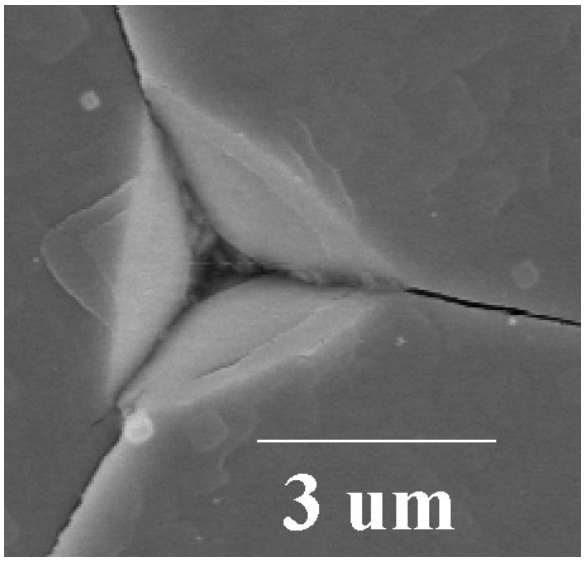

Figure 11 SEM micrograph in plan view of an indentation in a film made with a Berkovich indenter.

which is a ninth order polynomial fit of a plot of the area measured and the total displacement measured for this particular tip. The manufacturer of the tip, Nanoinstruments® determined the constants as C_0= 718.02, C_1= -0.00090549, C_2= -0.062832, C_3= 0.004929, C_4= 0.019922, C_5= 5.78E-5, C_6= -0.0064202 and C_7= 0.0014305.

Another triangular pyramidal indenter stylus used is a 'cube-corner'. As its name suggests, it is merely a cube-shaped diamond with one of its corners used as the indenter. The advantage of this type of indenter is that it is sharper than the Berkovich and will displace a greater amount of material than the Berkovich for a given load. Some authors, however, have utilized Vickers and Knoop indenters for nanoindentation.

The first indenter tips used for nanoindentation had a radius of curvature on the order of 300 nm, see Figure 12 [34]. Because of the assumption of an atomically sharp indenter tip, the effective plastic depth, h_p, is somewhat greater than the actual plastic depth due to the radius of curvature. Indenters with even smaller dimensions (100 nm radius of curvature) have been used by Kulkarni and Bhushan [37]. Still smaller indenters of 30-60 nm are available. The Berkovich tip used in this research has a radius on the order of 40 nm.

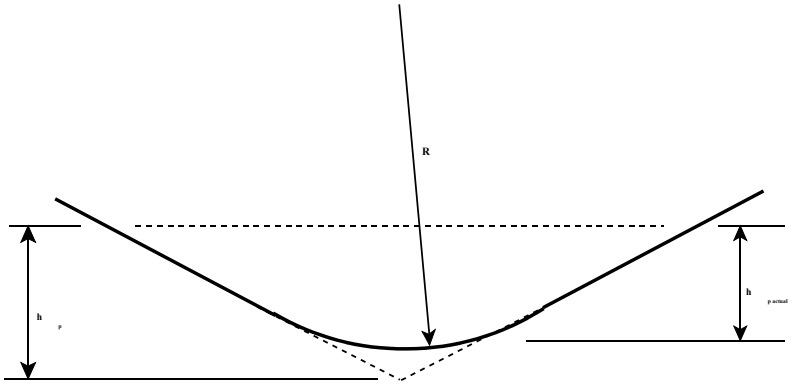

Figure 12 Radius of Curvature of Stylus, R.

It should be noted that the contact area is only a function of the effective plastic depth, h_p. The Nanoindenter®, however, measures only the total depth, h. The plastic depth required for the contact area can be found by rearranging equation (12)

$$h_p = h - h_s \tag{15}$$

From Sneddon's [38] solution h_s is given as

$$h_s = \varepsilon \frac{P_{\max}}{S} \tag{16}$$

where ε is a geometric constant based on the type of indenter tip (for this research ε = 0.72 was used) and S (N/m) is the stiffness, which can be obtained from the slope of the upper portion of the load displacement curve as shown by the dashed line in Figure 9. The Nanoindenter® can determine the stiffness continuously throughout an indentation by the application of a small sinusoidal oscillation on the applied load. The indenter apparatus and the specimen can be modeled as a simple harmonic oscillator. The phase and amplitude of the indenter oscillations are continuously measured along with the phase and amplitude of the imposed AC signal. The stiffness of the indenter frame, the mass of the of the indenter assembly, the damping constant for the capacitor plates and the spring constant of the supports for the indenter are all known values. This leaves the stiffness of the contact zone as the only unknown, which is easily computed during each indentation. This more detailed method is called the continuous stiffness measurement (CSM) option and was used for this research [39]. The stiffness can also be written as

$$S = \frac{dP}{dh} \tag{17}$$

The equation used for the effective plastic depth in this research is

$$h_p = h - 0.72 \frac{P_{\max}}{S} \tag{18}$$

There have been numerous studies involving the measurement of the microhardness of thin films using a nanoindentation device [40, 41, 31, 36, 42, 43, 44, 45]. A few of these are discussed here. Tsukamoto et al. performed some of the first tests on the nanoindenter, working on various films deposited on silicon: 0.1-0.4 μm thick carbon coating via magnetron sputtering and CVD, 0.15 μm thick SiO_2 via magnetron sputtering, 0.4μm thick SiO_2 via CVD and 0.3μm thick SiO_2 via oxidation [40]. These oxide film thicknesses are on the same order as the films in this research, 0.5 to 1.0μm. The load-displacement curves also show indentation depths of approximately 0.1 μm, which is also similar to the range in this work.

Other early work was by Quinto et al. [41] with TiN and HfN films of 8 μm thickness deposited via CVD and physical vapor deposition. These coatings were examined with a Vickers indenter to relate hardness to temperature variations. Bhushan et al. [31] performed nanoindentation on several substrates: 3 mm thick plexiglas, 3 mm thick tool steel, 23.4 μm thick polyethyleneterephthalate (PET), and a 4 μm thick magnetic coating on PET. The most notable trend they found was that the microhardness tended to be load dependent.

Additional researchers have worked a great deal on thin films. Nix et al. [36] measured the microhardness of 1 μm thick aluminum on silicon substrates with indentation depths up to 20 nm. Work done by Chou et al. [42] with radio frequency magnetron sputtering of films of 0.05 μm and 1.2 μm thick Al_2O_3 onto Si and NaCl was

done to compare the mechanical properties of γ and α alumina. Bell et al. [43] reviewed the performance of the Nanoindenter® on a 2 μm thick TiN coating on stainless steel, a 5 μm thick ZnAl coating on steel and a 1.25 μm thick solgel-formed ceramic coating on steel. Hjort et al. [44] utilized a Vickers indenter to find the microhardness of a 10 μm thick $Al_xGa_{1-x}As$ coating on a GaAs substrate and related the hardness as a function of stoichiometry (*x* in $Al_xGa_{1-x}As$). Haanappel et al. [45] deposited Al_2O_3 via metal-organic CVD on stainless steel in 0.07 μm and 0.5 μm thicknesses and related how the process parameters affected various mechanical properties, including the hardness. The indenter they used was developed by Shimadzu and had a Vickers-type stylus.

Elastic Modulus

The elastic modulus (Young's modulus) of any material is a significant property. From Hooke's Law, the elastic modulus indicates how compliant or flexible a material will be under stress. For thin films, stresses are always present to some degree, usually due to the manner in which the film is formed on the substrate. The exact mechanisms behind these inherent stresses are not fully understood and this area is a topic of on-going research [2]. How a thin film behaves under stress is largely dependent on its elastic modulus. For example, if the film has a high elastic modulus it may spall or peel off of the substrate due to the significant internal stresses created during deposition, whereas a low elastic modulus material may be able to withstand these stresses. Regardless of how the stresses and strains are created, it is important to know the elastic modulus of a

material for a particular application. Additionally, the elastic modulus of a material in thin film form can be very different from the elastic modulus of the same material in bulk form. The difference may be attributed to the variances in microstructure. For example, the density of voids and interfaces can affect the resulting elastic modulus of the thin film more so than the elastic modulus of the bulk material.

The elastic modulus can be determined from the Nanoindenter's ® load versus displacement curve, Figure 8. Loubet et al. [46] showed that the slope of the unloading curve is given by

$$\frac{dP}{dh} = \beta E^* \sqrt{A} \tag{19}$$

where P = load (N),

h = depth of indentation (m),

A = contact area (m^2),

β = constant dependent on indenter shape (dimensionless),

and E^*= effective modulus (Pa) of the system given by

$$\frac{1}{E^*} = \frac{1 - \nu_0^2}{E_0} + \frac{1 - \nu^2}{E} \tag{20}$$

where E_0 = elastic modulus of indenter (Pa),

E = elastic modulus of film (Pa)

ν_0 = Poisson's ratio of indenter

and ν = Poisson's ratio of film.

For the triangular Berkovich indenter, β= 1.167. Measuring the slope of the unloading curve and knowing the material properties of the indenter allows the determination of the elastic modulus of the film from equation (20). However, it should be noted that equation (19) is equal to the stiffness as shown in the previous section:

$$S = \frac{dP}{dh} = \beta E * \sqrt{A} \tag{21}$$

Using this equation and the continuous stiffness measurement method (the method used in this research) the elastic modulus can be determined.

Several researchers have worked with the Nanoindenter® or a similar microhardness apparatus to determine the microhardness as well as the elastic modulus of coatings. Nix reviewed elastic modulus determination via nanoindentation and found that it was valid for thin films of soft materials but produced greater values of modulus than expected for hard materials [36]. Possible explanations for this are the high pressures created beneath the indentation which may cause densification of that material, or the combination of plastic deformation of material under the stylus and elastic recovery after indentation may cause a higher modulus than expected. Bell et al. [43] agree that this method for determining modulus (and hardness) is best for materials with a low hardness to modulus ratio, i.e. metals, but the large elastic recovery during unloading for high hardness to modulus materials, i.e. ceramics, confounds the determination of the actual penetration depth and hence the modulus. This is the justification for using the effective

plastic depth in the calculations as shown in Figure 9. Chou et al. [42], however, found that the moduli for amorphous Al_2O_3 and γ-Al_2O_3 thin films were actually lower than expected. Other authors who have investigated thin films of these materials have found varying values for their moduli. Chou et al. attributes these differences to the various methods by which the films were deposited. One particular deposition method will result in a different microstructure than another method, resulting in differing properties.

Fracture Toughness

The fracture toughness of a material is a major topic of interest for many applications. The fracture toughness is related to the amount of stress a cracked material can endure without failing. This property is particularly important for thin ceramic films such as those investigated here. As previously mentioned, the deposition process of thin films can leave significant internal stresses which may lead to crack formation and/or growth. Failure of a thin film is usually defined as the point where spallation or delamination occurs, and the formation of a crack is the usual initiation event. Therefore the tougher a material is, the better its resistance to failure due to internal stresses and cracking.

Measurement of the fracture toughness of thin films by a Nanoindenter® or similar instrument has not been pursued heavily until recently. Lawn et al. developed the following equation to determine the fracture toughness, K_C ($MPa \cdot m^{0.5}$), of a material from

radial "half-penny" cracks formed during an indentation from a stylus such as that of a Nanoindenter® [47]

$$K_C = \alpha \left(\frac{E}{H} \right)^{1/2} \frac{P}{c^{3/2}} \tag{22}$$

where α = empirical constant which is ~0.016 for a Berkovich and ~0.032 for a cube-corner shaped diamond stylus

E = elastic modulus (Pa),

H = hardness (Pa),

P = applied load (N),

and c = crack length (m).

The elastic modulus and the hardness are both calculated from the Nanoindenter® data as discussed previously. The length of the racial crack is measured from the center of the indentation to the end of the crack tip as shown in Figure 13.

Lawn et al.'s model requires that the cracking be radial emanating from the indenter points and half-penny in shape within the material, i.e. no lateral cracking. Additionally, their model requires that the crack must be a "well-developed crack", meaning the length, c, must extend past the plastic zone created by the indenter tip. Figure 14 [47] shows a cross-sectional schematic of an indenter tip, the plastic zone and radial cracking. Lawn et al. also developed a relationship between the plastic zone size and the elastic modulus to hardness ratio (E/H) for a material, Figure 15 [47] where b is

the plastic zone radius and r_0 is the cavity radius (the distance from the center of the indent to a point of the indent, also referred to as the indent size). The *E/H* for the films studied in this research was on the order of 20 which from Figure 15 was a b/r_0 value of about 2.1. From this the acceptable crack length, *c*, that can be used in equation (22) was approximately twice the indent size ($c > 2\ r_0$).

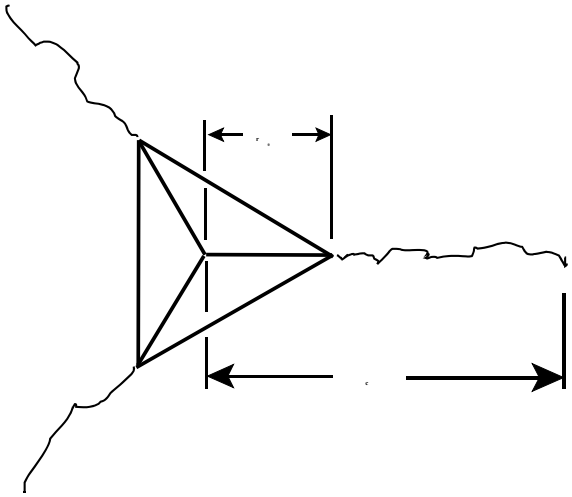

Figure 13 Indentation and Crack Measurement.

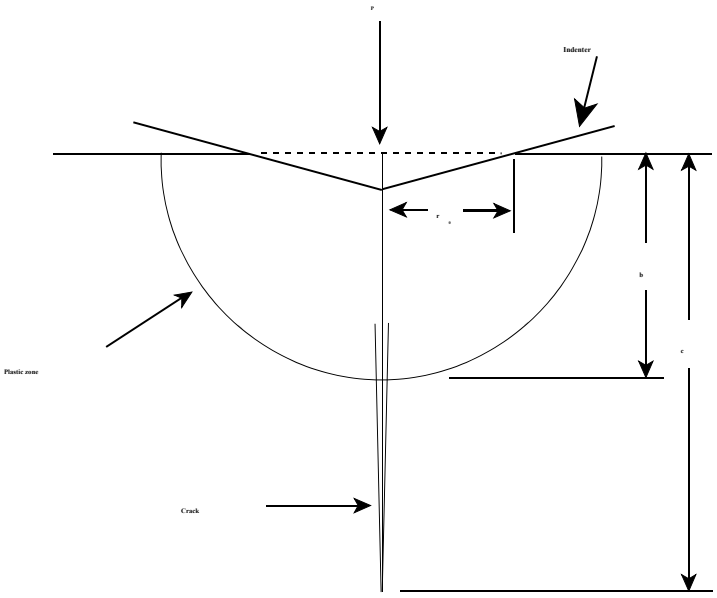

Figure 14 Schematic of indentation showing plastic zone and radial crack.

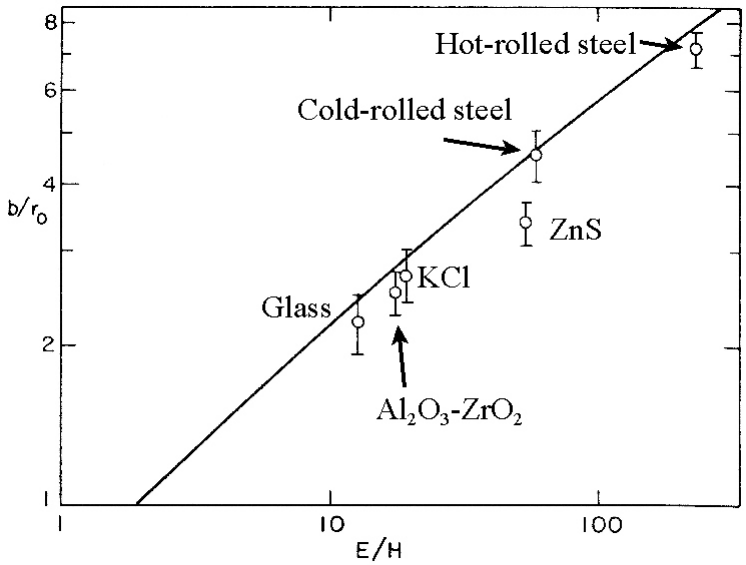

Figure 15 Plot showing plastic zone size, b, to cavity radius r_0 ratio versus modulus to hardness ratio for several materials.

As with the measurement of microhardness and elastic modulus, the best type of indenter for fracture toughness is the Berkovich indenter according to Bell et al. [43]. They studied the various types of indenters along with fracture toughness. Compared to the Vickers indenter, Bell et al. achieved more reliable results, particularly at low loads, with the Berkovich indenter. Some materials, however, may not crack under the Berkovich indenter because of their high toughness. Harding et al. [48] found that brittle materials have a load threshold below which the applied load will not cause the formation of cracks from an indentation. Changing from a Berkovich indenter to a cube-corner indenter, which has a much sharper angle and a greater displacement, will reduce the load threshold. With the same applied load, the cube-corner indenter will crack material that the Berkovich indenter will not crack. Utilizing the cube-corner indenter tip, Harding et al. reduced the threshold load for cracking to less than 1 mN.

One of the potential problems with measuring mechanical properties of thin films, as mentioned in a previous section, is the influence of the substrate. Hjort et al. [44] and Haanappel et al. [45] used a Vickers indenter to determine the fracture toughness of 0.5 μm thick Al_2O_3 on stainless steel and 10 μm thick $Al_xGa_{1-x}As$ on GaAs, respectively. Cross-section examinations of the indentations showed that the indentations were deep enough to fracture the substrate under the coating for both groups. This particular concern was taken into consideration during the reduction of fracture toughness data.

Kant et al. [49] reviewed the dependence of fracture toughness on the grain size and grain orientation in their measurements of CVD deposited diamond coatings. They found the fracture toughness to be independent of the grain size and orientation. Other background work includes De Boer and Gerberich's [50] study of the toughness of 0.8 μm thick tungsten films on SiO_2 and Weppelmann et al.'s [51] measurement of the toughness of 2.47 to 4.5 μm thick PVD TiN coatings on Si. These numerous reports supported the belief that the fracture toughness of YSZ-alumina thin films can be determined via nanoindentation and they helped provide the impetus to attempt this work.

CHAPTER III

EXPERIMENTAL PROCEDURE

Combustion CVD Deposition Apparatus

A general schematic of the combustion chemical vapor deposition (combustion CVD) system is shown in Figure 16. Solutions were prepared by dissolving organic or inorganic salts in reagent grade toluene or other similar organic solvent or solvents in order to place the desired metals (Y, Zr and Al in this case) in solution. The solution was then pumped by a Constametric 4100 high performance liquid chromatography (HPLC) pump to the nozzle, see Figure 16.

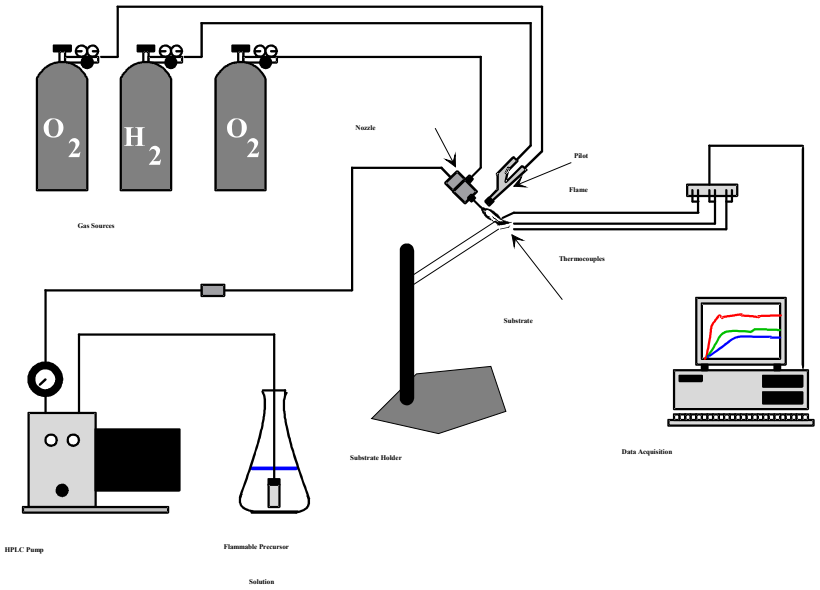

Figure 16 Combustion CVD Schematic.

The liquid precursor solution exited the nozzle through a small central capillary tube. The proprietary nozzle produces an aerosol out of this tube. Additional dry oxygen necessary for complete combustion was provided concentrically around the aerosol as shown. The oxygen flow rate was controlled by varying the regulator back pressure and flow control valve, and by monitoring the mass flow meter. The aerosol is ignited by a pilot flame fueled by hydrogen. The substrates for the depositions were mounted on a Kanthal wire frame (high temperature wire Kanthal A-1, Kanthal Corp., Bethel, CT) and suspended near or just inside the tip of the flame, see Figure 17. The substrate was mounted such that the flame approached at an angle of approximately 45Ewith respect to the substrate normal.

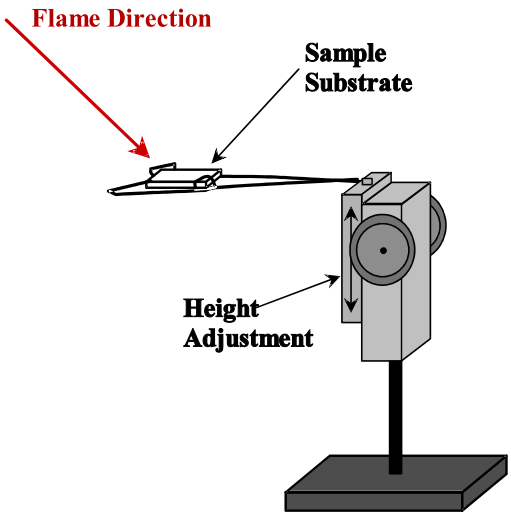

Figure 17 Apparatus for Suspending Substrate in Flame.

Deposition Parameters

In order to deposit high quality thin ceramic films with combustion CVD, the optimum deposition parameters were determined. The optimum parameters were those conditions that produced the densest-appearing film with a maximum adhesion to the substrate and the fastest deposition rate. Both trial and error and the advice of experienced combustion CVD scientists helped to shorten the time necessary to determine the optimum conditions. The different parameters that were optimized include the temperature, solution flowrate, metal ion concentration, type of solvent, type of substrate material and oxygen flowrate.

Temperature

By varying the location of the substrate relative to the tip of the flame the surface temperature of the substrate was controlled. The substrate was positioned near or just inside the flame tip. Type K and type B thermocouples were used to monitor the substrate surface temperature and the flame temperature just above the substrate. Flame temperatures just above the substrate surface during deposition were in the range of 1000EC to 1650° C, while substrate temperatures were in the range of 800EC to 1150° C. Substrate temperature was measured by attaching a type K thermocouple to the back of the substrate using Ceramabond high temperature ceramic adhesive.

Solution Concentration

Yttrium 2-ethylhexanoate (Y 2-EH), zirconium 2-ethylhexanoate (Zr 2-EH) and aluminum acetylacetonate (Al ac-ac) were used as precursors. These compounds were dissolved into toluene for total metal ion concentrations ranging from 0.001 M to 0.1 M.

Substrates

Pieces of single crystal a-plane alumina, approximately 1 cm x 1 cm x 1 mm in size were used as substrates. These ceramic substrates were selected because of the high temperatures necessary for the deposition of YSZ-alumina. There were several depositions performed with substrates of single crystal r-plane alumina, amorphous silica, single crystal MgO, single crystal 9.5 mol% Y_2O_3-ZO_2 and polycrystalline alumina. These other substrates were used in the development of the deposition technique for the YSZ-alumina combustion CVD films.

Film Materials

Film thickness

Based on a minimum indentation depth of 20 nm and the guideline that the film thickness be 5 to 10 times the indentation depth, the film thickness were greater than 0.8 μm, to avoid the influence of the substrate on the films' mechanical properties. Coatings were deposited on substrates using the parameters shown in Table 1.

Table 1: Deposition Parameters

Solvent	Toluene
Precursors:	Yttrium 2-EH[1] Zirconium 2-EH Aluminum acac[2]
Solution Flow Rate	4 ml/min
Concentration of Precursor Solution:	0.002 M
Nebulizer	Proprietary
Oxidizer	Oxygen
Oxidizer Flow Rate	20 lpm
Deposition Rate	1.8-2.5 μm/hr
Flame Temperature	1350 - 1650°C
Substrate Temperature	800 - 1150°C
Substrate	a-plane alumina
Pilot Flame Fuel	Hydrogen
Deposition duration	30 min

[1]2-ethylhexanoate

[2]acetylacetonate

YSZ-alumina Components

The amount of yttria in the zirconia was 8 wt% or 4.5 mol%. This is the most common yttria partially stabilized zirconia compound used and studied in TBC's. The amount of alumina present in the YSZ was varied between 0% and 100% with the

zirconia-alumina eutectic, which occurs at 57.4 wt% Al_2O_3 (62.8 mol%), as one of the testing points (refer to the phase diagram in Figure 18). The specific mole percentages of alumina used in the depositions were 0, 15, 30, 45, 62.8, 80 and 100%.

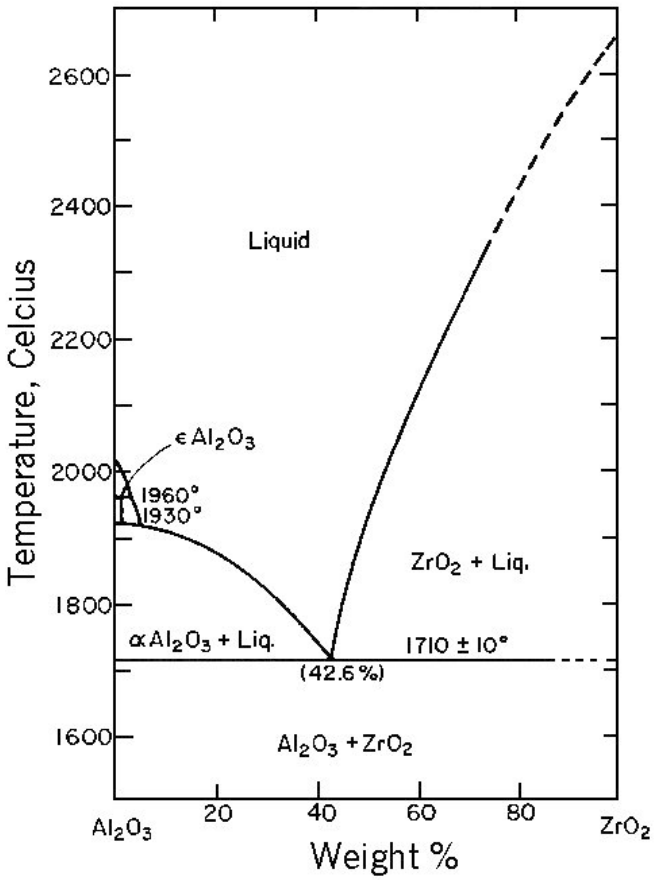

Figure 18 Alumina-Zirconia Phase Diagram.

Repeatability Study

Experience with the present combustion CVD nozzle has shown that several factors may change the characteristics of the films deposited. One factor was that the nozzle tip (capillary tube) became clogged after numerous hours of depositions requiring replacement of the nozzle tip. The clogging of the nozzle tip was found to be due to the deposition of alumina on the inner surface of the capillary tube. It was observed that a new nozzle tip had some flame characteristics different from the previous tip, such as the direction of the flame and completeness of combustion of the flame. Each new nozzle tip (capillary tube) was prepared by polishing both ends with silicon carbide grinding paper in order to give a round, clear open end for unrestricted flow of the precursor. Upon installation the aerosol produced by the nozzle tip may not be centered among the pilot flames because of the mechanical polishing and the design of the holder for the nozzle tip. Centering of the aerosol was accomplished manually. This hand polishing and hand manipulation of the nozzle tip is not exactly reproducible, however to be as reproducible as possible, the nozzle tip's geometry was adjusted until the general appearance of the aerosol and the flame was similar to previous depositions.

Another factor was that the position of the substrate in the flame was adjusted based on the flame temperature just above the substrate surface. In other words, the substrate was moved in the flame until a desired temperature was reached. Because measurement of this flame temperature was not extremely precise, ±50EC, the position of

the substrate in the flame was not exactly the same for different depositions performed at the same temperature. These factors may affect the characteristics of the films deposited.

In order to provide confidence in the ability to deposit consistent thin films via combustion CVD, a repeatability study was conducted. Several substrates were coated with one type of film under as similar as possible conditions. The differences from one deposition to the next was movement and reconfiguration of the apparatus. This included removing, adjusting and replacing the nozzle tip. Characterization and mechanical testing of these films were performed to show that a film grown on a substrate under a certain set of conditions on one particular day could be reproduced.

Characterization

Films were characterized with various materials analysis tools. A Phillips $\theta/2\theta$ Automated Powder Diffractometer was utilized for phase identification and residual stress analysis. A Hitachi S-800 scanning electron microscope (SEM) was used to characterize film morphology and film thickness. Using secondary electron imagery the SEM allowed the microstructures to be determined in a relatively straightforward manner. The samples with deposited films were cross-sectionally fractured to expose the microstructure of the film and substrate. This cross-section allowed the examination of the growth morphology and direct measurement of the film thickness. Back scatter

electron imagery was used for compositional analysis as well as energy dispersive spectroscopy (EDS).

A Hitachi HF-2000 Field Emission Transmission Electron Microscope (TEM) was used for more detailed studies of microstructure, grain orientation, and composition. Electron diffraction was used to identify phases, to evaluate grain crystal structure and to verify possible crystal orientation preferences. Grain sizes were measured from the dark field images obtained on the TEM. The composition of individual grains examined within the TEM were obtained using oxygen-sensitive EDS. Several TEM specimens were prepared by scraping the film with a clean sharp stainless steel blade onto a copper TEM specimen grid. Other TEM specimens of thin plan-views and cross-sections were prepared using standard thin foil preparation techniques.

Mechanical Properties Measurements

Microhardness

The microhardness of all the YSZ-alumina films deposited via combustion CVD were measured with the Nanoindenter® at Oak Ridge National Laboratory's High Temperature Materials Laboratory, Oak Ridge, TN. Several indentations were made on each sample for a good statistical sampling. The Berkovich indenter tip was used for each sample. The usual setup was an array of 15 indentations in a 5 by 3 matrix with a 15μm spacing, see Figure 19. As described in a previous section, each indentation

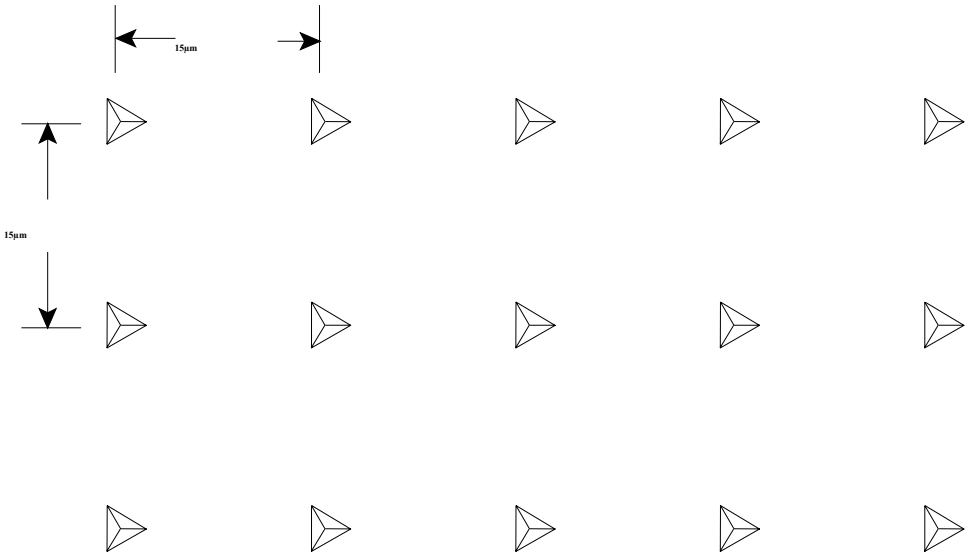

Figure 19 Indentation matrix for hardness and elastic modulus measurements.

produced a load versus displacement curve. From this curve, the maximum load and the effective plastic depth were used to determine the hardness based on the equations presented above.

Elastic Modulus

The elastic modulus was also determined using the Nanoindenter®. As discussed in Chapter II, from the load versus displacement plot, the slope of the unloading curve was used to find the modulus. The same indentations used for measuring the hardness were used to determine the elastic modulus.

Fracture Toughness

Fracture toughness of the thin films was evaluated using additional indentations made in each sample. The cube-corner indenter tip was used to crack the films because preliminary indentations with the Berkovich indenter tip did not cause cracking. Several indentations were made at various loads. The usual setup was five indentations at 400 mN, five at 250 mN, five at 100 mN, five at 50 mN and five at 25 mN. This resulted in a 5 by 5 matrix of 25 indentations, Figure 20. Some of the films and substrates tested would not crack at the lowest loads. The heaviest loads produced indentations which were

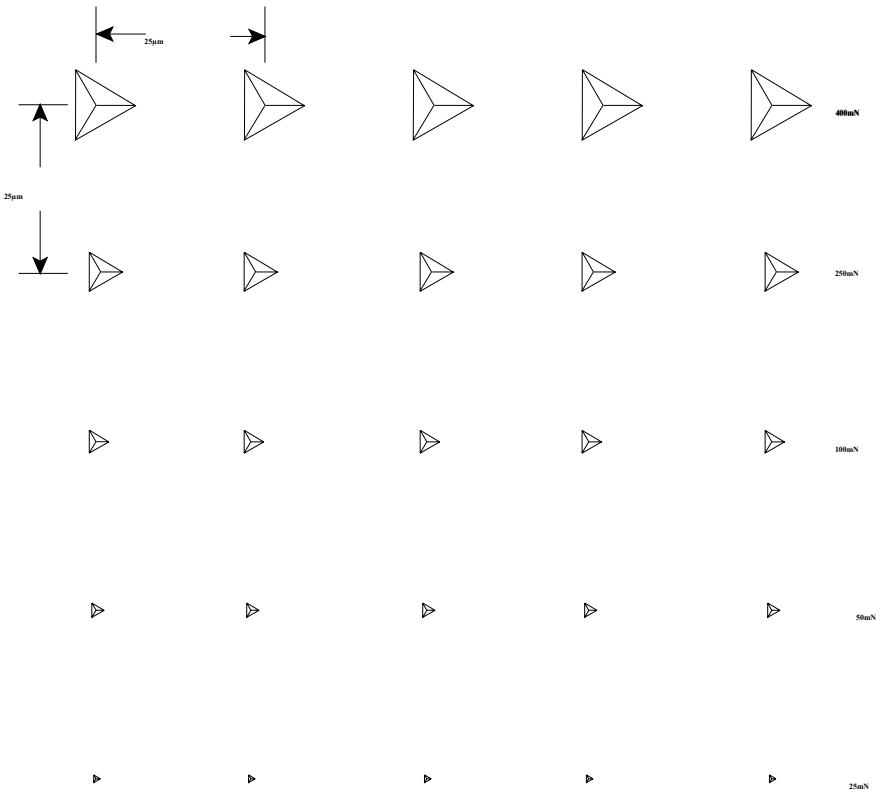

Figure 20 Indentation Matrix for Fracture Toughness Measurements.

necessary for locating the matrix of indentations in the scanning electron microscope. For the combustion CVD coated specimens the smaller indentations do not penetrate through the film into the substrate, which provided a truer measure of the film properties than the heavy indentations which broke completely through the film. Crack initiation in the films was from the points of the indentations and continued radially outward from the center of the indentation. In determining the fracture toughness, when no cracks developed from the lighter loads, the indentations from higher loads which did produce cracks were used. The calculation of the fracture toughness was derived from the crack length as described in Chapter II.

CHAPTER IV

RESULTS

Deposition Parameters

Over 200 depositions were made during the development of the YSZ-alumina thin films used in this research. The appropriate parameters used for the depositions were obtained within the first eighty or so runs. Table 1 from Chapter III shows the deposition parameters used in this study. The optimum deposition flame temperature found was 1550EC ± 50E. while the substrate temperature was 1050EC ± 10E. The results presented here will detail the characterization of the deposited films and their mechanical properties obtained from the Nanoindenter®. The images and data shown will only be from representative samples.

Characterization

Scanning Electron Microscopy

The bulk of the information gathered for this research was from SEM micrographs. The morphology of the films was examined and characterized by secondary electron SEM imaging as was the observation and measurement of the cracks required for fracture toughness determination. Figure 21 shows the plan-views and cross-section views

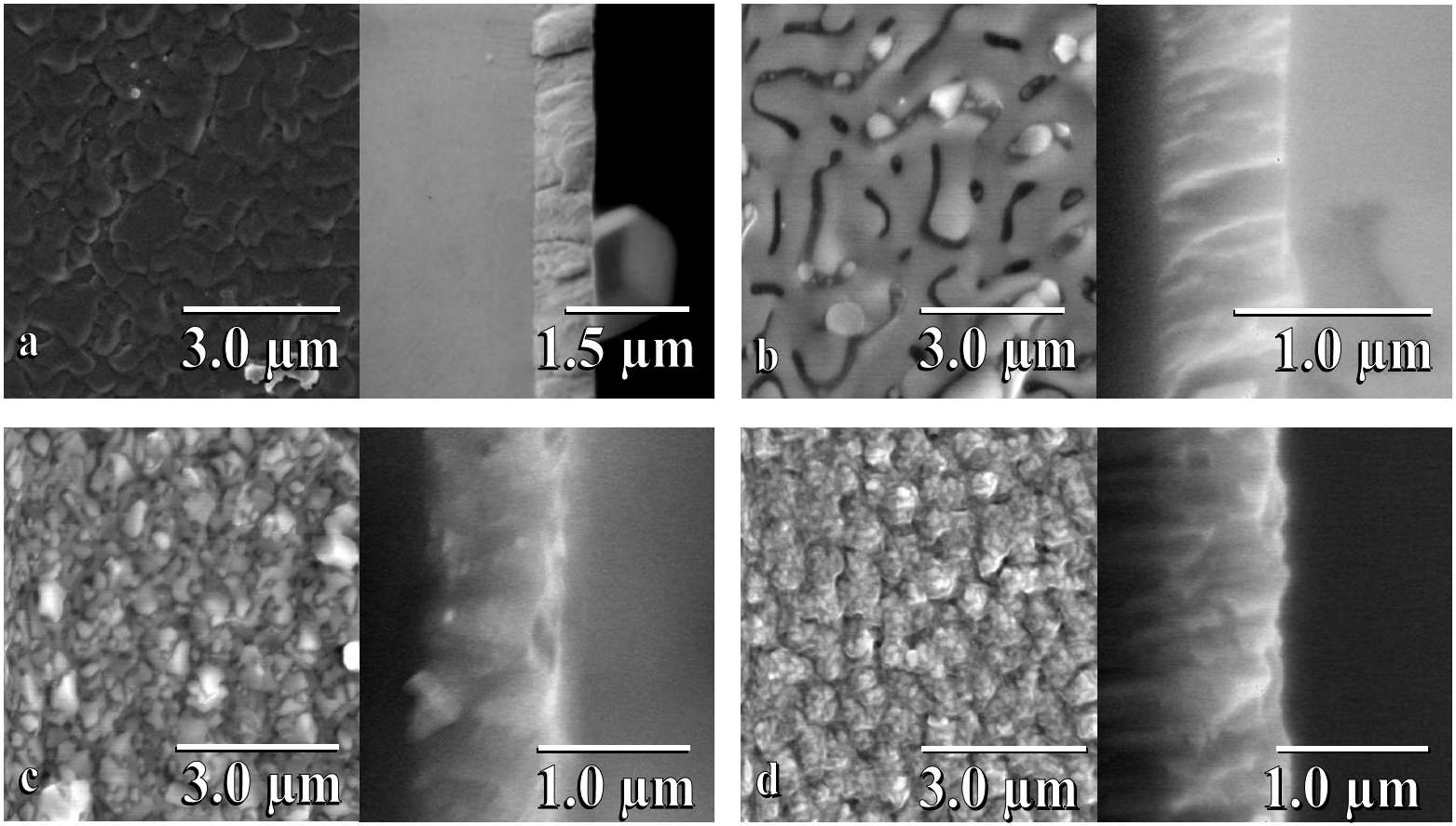

Figure 21 SEM micrographs of YSZ-alumina films, plan-views (left image) and cross-sections (right image): a) 100% YSZ, b) 15 mol% Al_2O_3, c) 30 mol% Al_2O_3, d) 45 mol% Al_2O_3

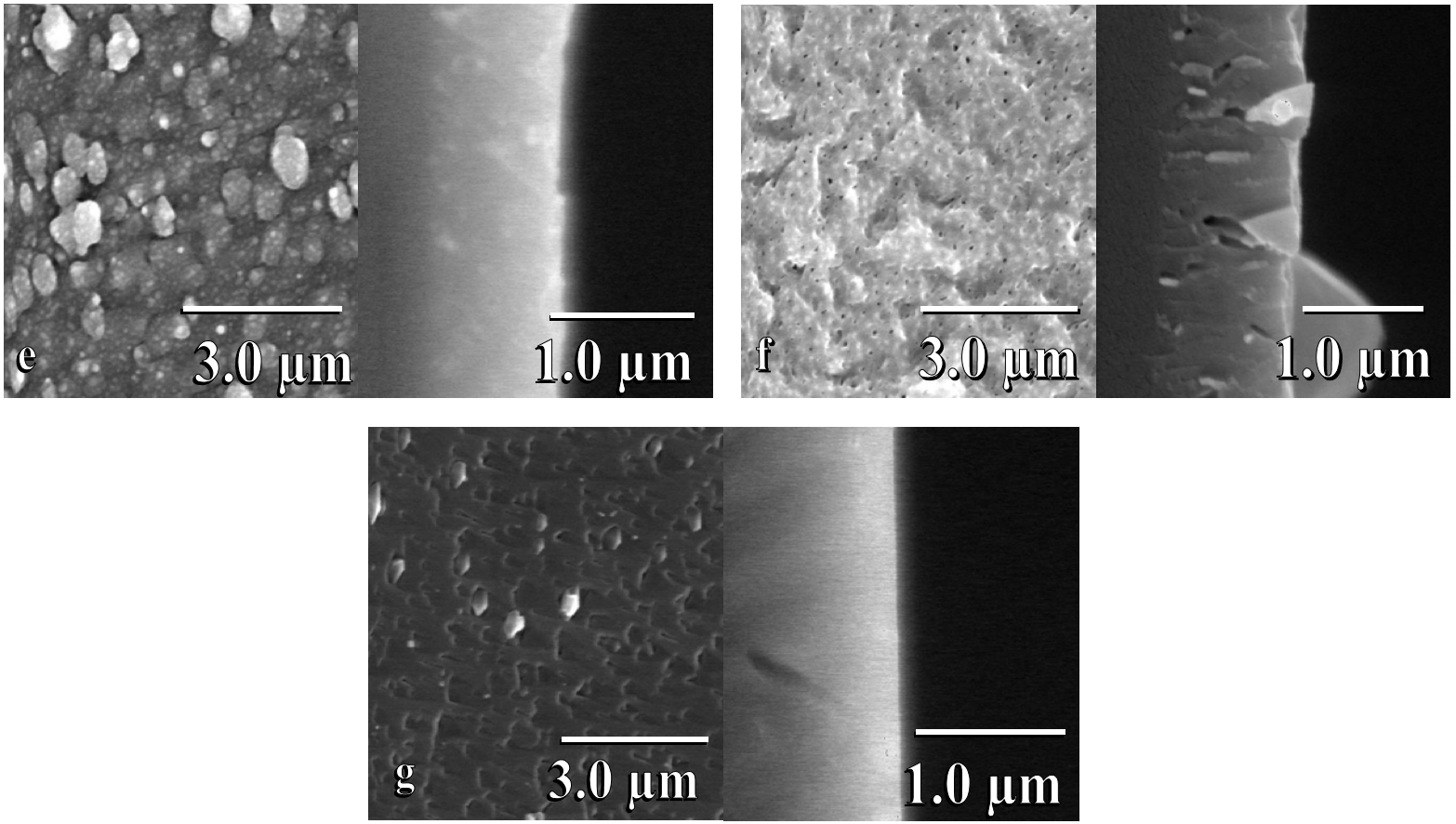

Figure 21 Continued, e) 62.8 mol% Al_2O_3, f) 80 mol% Al_2O_3, and g) 100 mol% Al_2O_3.

of the films made for each of the compositions studied (0, 15, 30, 45, 62.8, 80 and 100 mol% alumina).

The deposition rates, Table 2, were determined from the film thicknesses measured from the SEM images and the total deposition time. The deposition rate is seen to increase from a rate of 1.3 ± 0.10 μm/hr for the deposition of pure YSZ to a maximum rate of 1.7 ± 0.10 μm/hr for the eutectic composition and to then fall off to 0.76 ± 0.18 μm/hr for pure alumina. The film thickness was also a significant factor as mentioned in the background section of this thesis. The film had to have a large enough thickness such that the substrate did not influence the indenter. It was also found that actual thickness of the 100% alumina film was difficult to judge. This was because both the film and the substrate were alumina making the film-substrate interface indistinct. This may be a

Table 2: Film Deposition Rates

Precursor mol%	Precursor vol%	Deposition Rate, (μm/hr)
0	0	1.3 ± 0.10
15	16.7	1.4 ± 0.15
30	32.7	1.6 ± 0.20
45	48.1	1.6 ± 0.08
62.8	65.7	1.7 ± 0.10
80	81.9	1.5 ± 0.09
100	100	0.76 ± 0.18

factor in the relatively low deposition rate measured at this composition. Several observations in addition to film thickness may be noted from the figures: the surface roughness of the films and the distribution of the two phases. Surface roughness of the films was an important factor in the Nanoindenter® work, as the smoother the film, the more reliable the results and the quicker the data acquisition.

The two distinct phases of YSZ and alumina were visible in secondary electron images, see Figure 21. However, they were very distinct in backscatter electron images, see Figure 22, which shows the plan-views for both the secondary electron images and back-scatter electron images for every two-phase film. The lighter atomic weight elements (aluminum from the Al_2O_3) appear dark, while the heavier elements (yttrium and zirconium from the YSZ) appear light in contrast. For ease of discussion the majority phase of the film will be referred to as the matrix and the minority phase will be the second phase, i.e. for volume percent less than 50% alumina, the matrix is YSZ and the second phase is alumina and for greater than 50% alumina, the matrix is alumina and the second phase is YSZ. It is noted that for the lower alumina compositions the second phase of alumina appears as swirls, see Figure 22a, b and c, while for higher alumina content films the second phase of YSZ appears more uniform as spherical particles, see Figure 22e, for example.

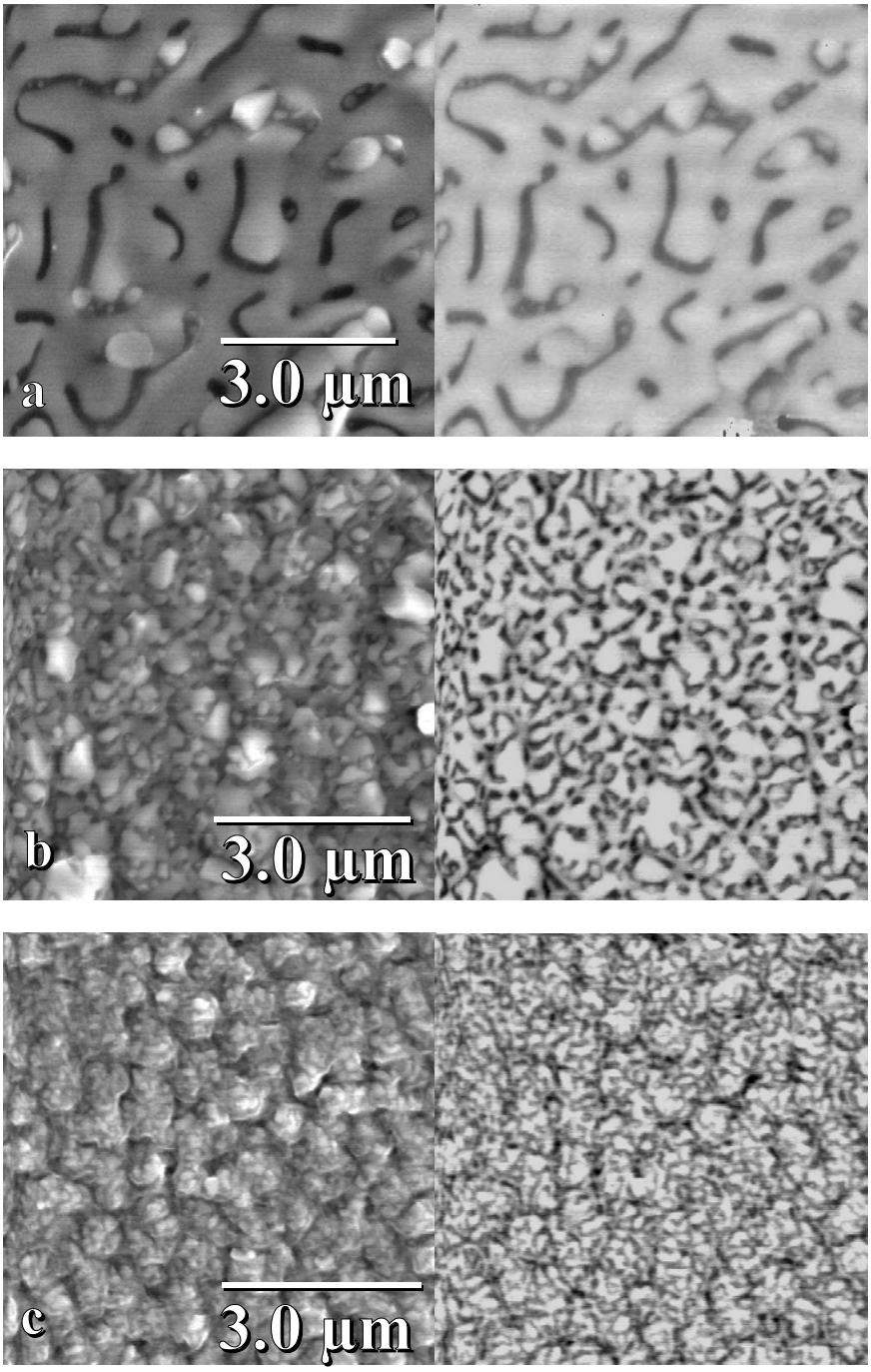

Figure 22 SEM micrographs of YSZ-alumina films, secondary (left image) and backscatter electron (right image) images; a) 15 mol% Al_2O_3, b) 30 mol% Al_2O_3, c) 45 mol% Al_2O_3,

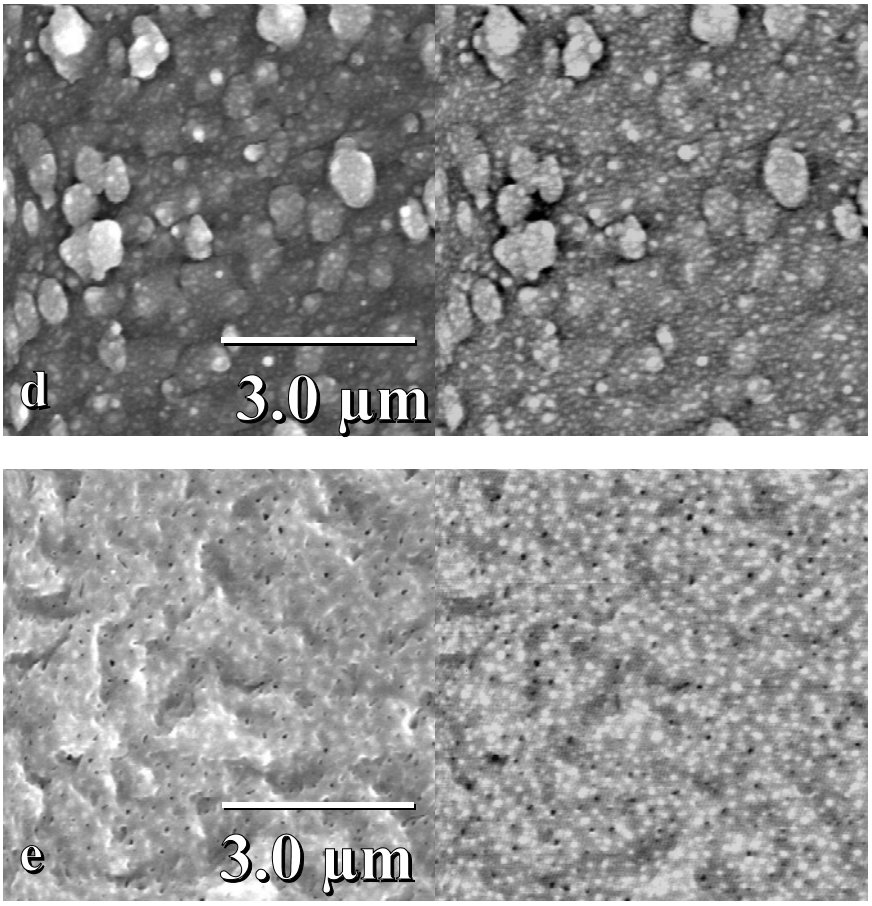

Figure 22 Continued, d) 62.8 mol% Al_2O_3, and e) 80 mol% Al_2O_3.

During the development of the YSZ-alumina films it was noted that the second phase particle size was different for different deposition temperatures, particularly for the eutectic composition of 62.8 mol% alumina. Figure 23 shows the 62.8 mol% alumina films deposited with flame temperatures of 1550EC and 1650EC. Again for these images the light regions were YSZ while the darker matrix was alumina. The YSZ regions for the 1550EC deposition were smaller than that of the 1650EC deposition. To help analyze this phenomenon, a series of anneals at 1500EC for 2.5 hrs, 5 hrs and 10 hrs was performed on the 62.8 mol% alumina film deposited at 1450EC, see Figure 24. As the anneal time increased the size of the YSZ particles increased and the distance between particles (nearest neighbor distances) also increased.

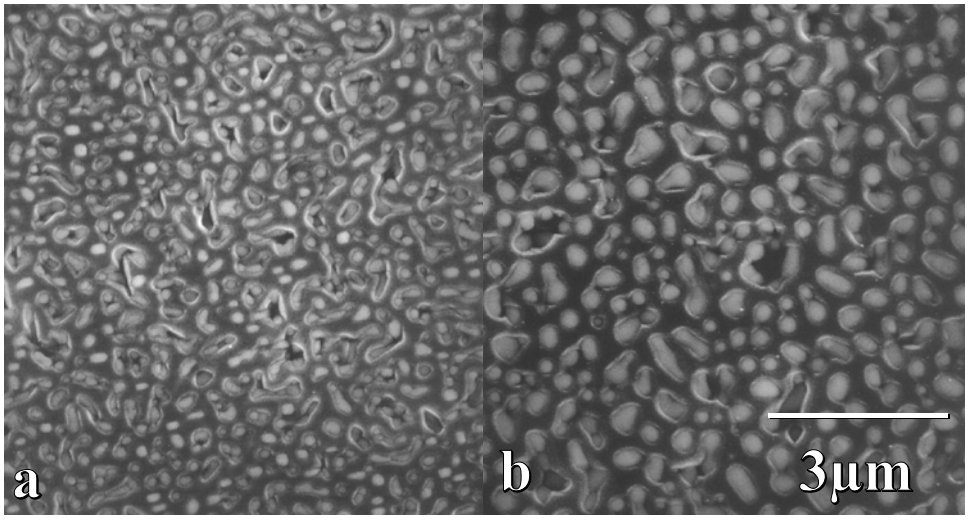

Figure 23 SEM micrographs of YSZ-62.8mol% Al_2O_3 films deposited at a) 1550EC and b) 1650EC flame temperature.

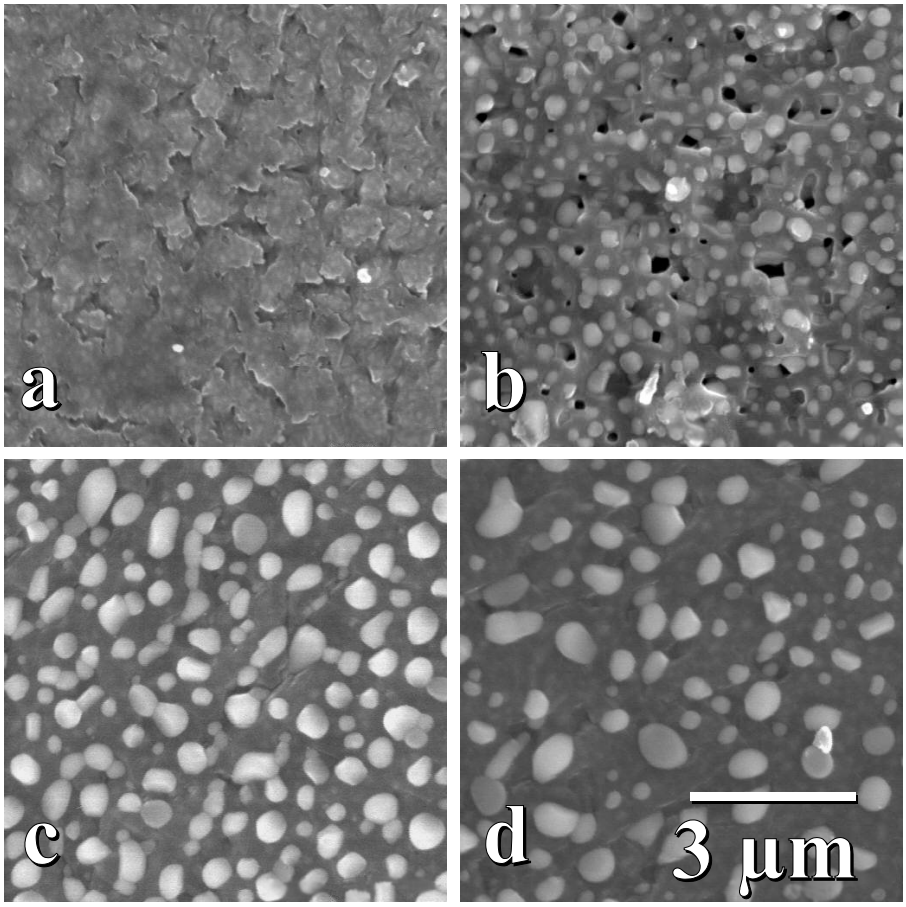

Figure 24 SEM micrographs of YSZ-62.8mol% Al_2O_3 films annealed at 1500EC for a) 0 hrs, b) 2.5 hrs, c) 5 hrs and d) 10 hrs.

Quantitative image analysis was performed on these images yielding the average particle sizes, see Figure 25, and the three nearest neighbor distances for the YSZ particles, Figure 26. The error bars represent two standard deviations (or ± one standard deviation) of the particle size and distance for each figure. The error bars on the sample that was not annealed data point cannot be discerned on the figure because they were very tight compared to the error bars for the other anneal times.

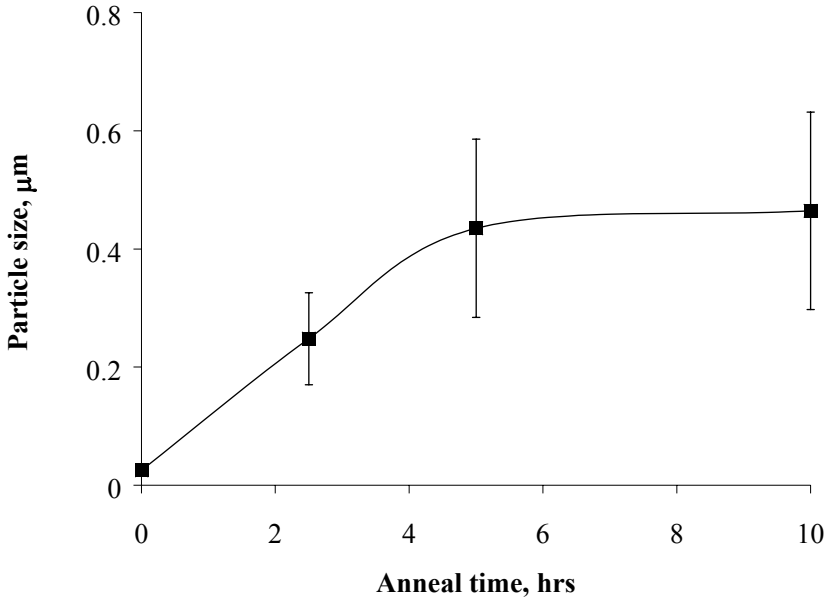

Figure 25 Particle sizes for 62.8 mol% Al_2O_3 anneal series.

It can be seen from Figure 25 that the particle size increases with anneal time at 1500EC to maximum of ~ 0.43 µm. Additional annealing did not significantly alter the particle size. The particle spacing (nearest neighbor distance) as shown in Figure 26 continuously increased as the annealing time increased.

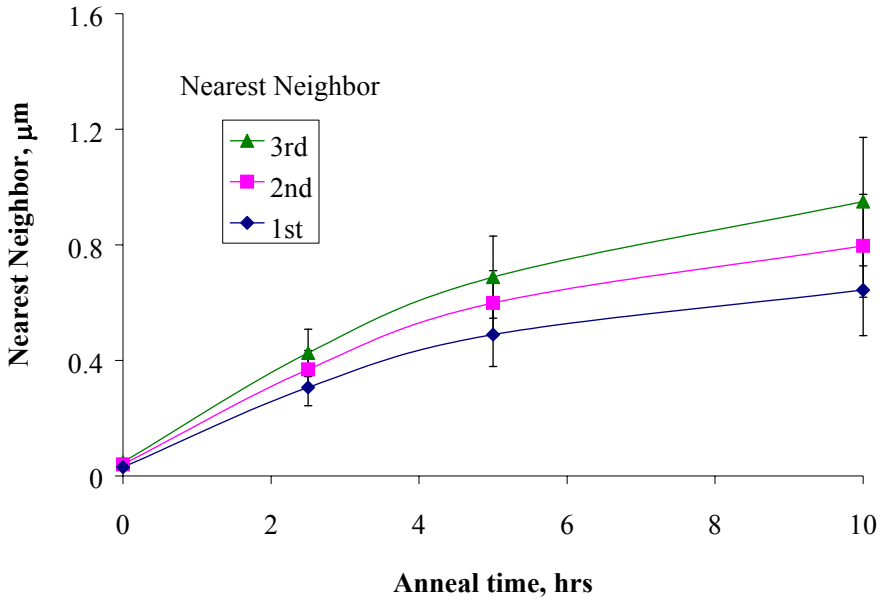

Figure 26 Nearest neighbor distances for 62.8 mol% Al_2O_3 anneal series.

X-ray Diffraction

An x-ray diffraction θ-2θ scan from an APD for a 62.8 mol% alumina film deposited on an amorphous silica substrate is shown in Figure 27. It was found that x-ray analysis of the films produced diffraction peaks for the YSZ but did not produce diffraction peaks for the alumina. The amorphous nature of the substrate was easily apparent by the size of the background and the characteristic hump at 20E 2θ. The zirconia powder diffraction card peaks were noted on the figure and matched with the YSZ peaks in the scan. However, no peaks were present from the alumina in the film.

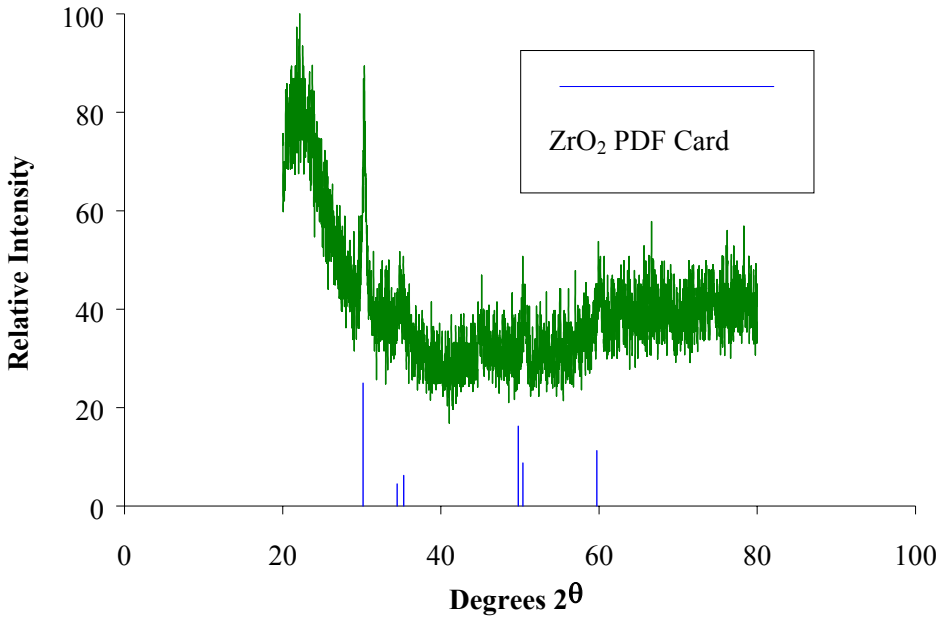

Figure 27 APD x-ray diffraction pattern of a 62.8 mol% Al_2O_3 film deposited onto amorphous silica.

An APD scan of a 100% YSZ film was performed to identify the phase of the YSZ film, Figure 28. Indexing this scan provided only verification that the film contained zirconia, in either the cubic or tetragonal phase. If the phase of YSZ was tetragonal, the the faint {$_1$G$_2$}-type reflections would be present. There was no evidence of this peak in the x-ray scan. Proper identification of the phase was performed later via TEM electron diffraction.

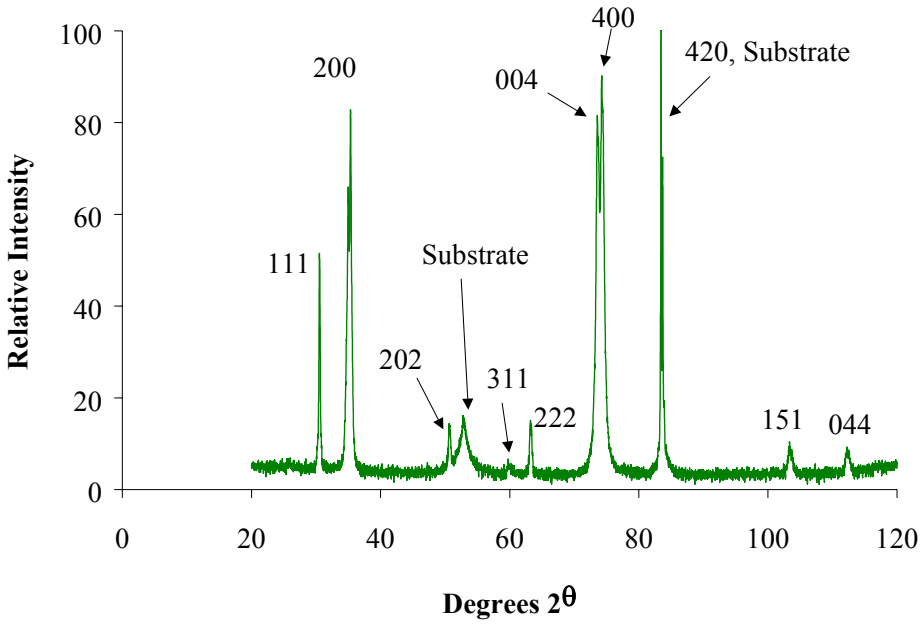

Figure 28 APD x-ray diffraction pattern of a 100% YSZ film deposited onto a-plane alumina.

Residual Stress

Film Stress: Film stress, σ_F (Pa), in the film was calculated directly from the coefficient of thermal expansion differences between the film and the substrate with this equation [2]:

$$\sigma_F = \frac{\left(\alpha_s - \alpha_f\right)\Delta T E_f}{\left(1 - \nu_f\right)} \tag{23}$$

where α_s = coefficient of thermal expansion (CTE) for the substrate (EC^{-1}),

α_f = coefficient of thermal expansion for the film (EC^{-1}),

ν_f = Poisson's ratio for the film,

ΔT = difference between the deposition temperature (substrate temperature) and room temperature (EC), T_{roomm} - $T_{substrate}$.

and E_f = elastic modulus of the film (Pa).

The film properties are determined from a simple rule of mixtures and the volume percent of the second phase particle, V_f:

$$\alpha_f = V_f \alpha_p + \left(1 - V_f\right)\alpha_m \tag{24}$$

$$\nu_f = V_f \nu_p + \left(1 - V_f\right)\nu_m \tag{25}$$

$$E_f = V_f E_p + \left(1 - V_f\right)E_m \tag{26}$$

where the subscript *m* if for the matrix and *p* is for the second phase particles. Literature values for the materials properties of Poisson's ratio, CTE and elastic modulus are shown in Table 3 .

Table 3: Material Properties

Material	***v*,**	***α*, x 10^{-6}, EC^{-1}**	***E*, GPa**
Al_2O_3[52]	0.27	7.9	390
YSZ[53]	0.31	10.4	200

Assuming a linear distribution of stress from maximum at the interface of the substrate and film to zero at the surface of the film (zero because the film is unrestrained at the surface), the reported average film stress of the deposited films is half of the maximum, Table 4. The results of film stress calculation show that the stress was in tension for all compositions. The maximum was near 100% YSZ at 9 vol% alumina while the minimum was at 100% alumina, Figure 29.

Matrix Stress: An additional stress in the film is the matrix stress. Matrix stress is the stress due to the CTE mismatch between the matrix material and the second phase material. The matrix stress, *q* (Pa), was determined from Taya et al. [54] as follows:

$$q = -2V_f \beta \alpha^* \frac{E_m}{A} \tag{27}$$

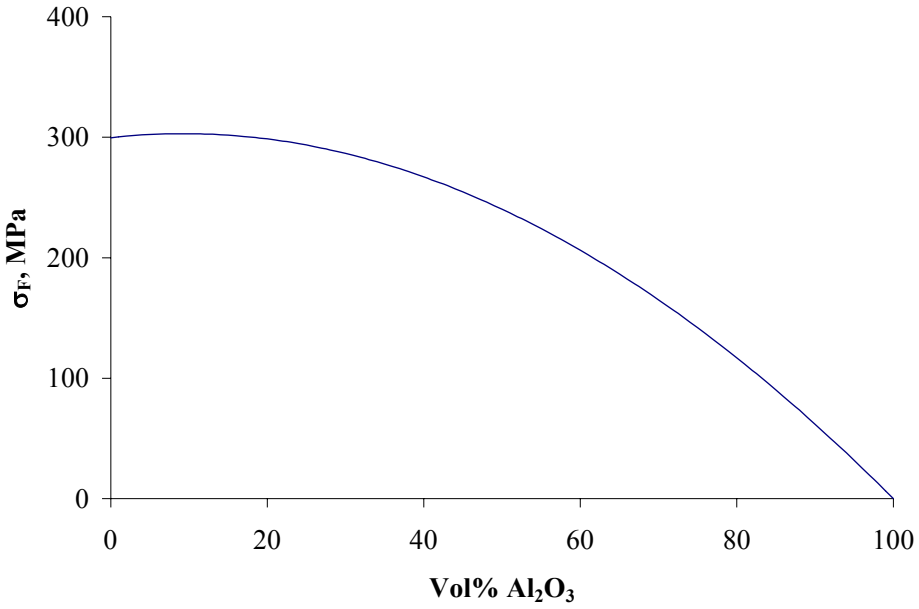

Figure 29 Film stress due to substrate/film CTE mismatch versus Al_2O_3 content in films.

and β (dimensionless) is a ratio of elastic moduli given by

$$\beta = \left(\frac{1 + \nu_m}{1 - 2\nu_p} \right) \frac{E_p}{E_m} \tag{28}$$

The term A (dimensionless) is given by

$$A = \left(1 - V_f\right)\left(\beta + 2\right)\left(1 + \nu_m\right) + 3\beta V_f \left(1 - \nu_m\right) \tag{29}$$

and α^* (EC^{-1})is

$$\alpha^* = \left(\alpha_p - \alpha_m\right)\Delta T \tag{30}$$

with the Poisson's ratio, elastic modulus, coefficient of thermal expansion, change in temperature as defined previously.

The resulting matrix stress for the films is also shown in Table 4. The results show that the matrix stress was in tension for the low volume percent alumina and in compression for the high compositions of alumina. The matrix stress was zero at the 100% YSZ and the 100% alumina compositions with a maximum at 45 mol% alumina and a minimum at 62.8 mol% alumina. Figure 30 shows the matrix stress versus the alumina composition.

Table 4: Film Stress Determined by CTE Mismatch

Precursor mol% Al_2O_3	Film stress, σ_F (MPa)	Matrix stress, q (MPa)	Film and matrix stress, $\sigma_F + q$, (MPa)
0	300	0	300
15	301	77.9	379
30	282	148.0	430
45	246	211	457
62.8	184	-239	-55.1
80	107	-119	-13.1
100	0	0	0

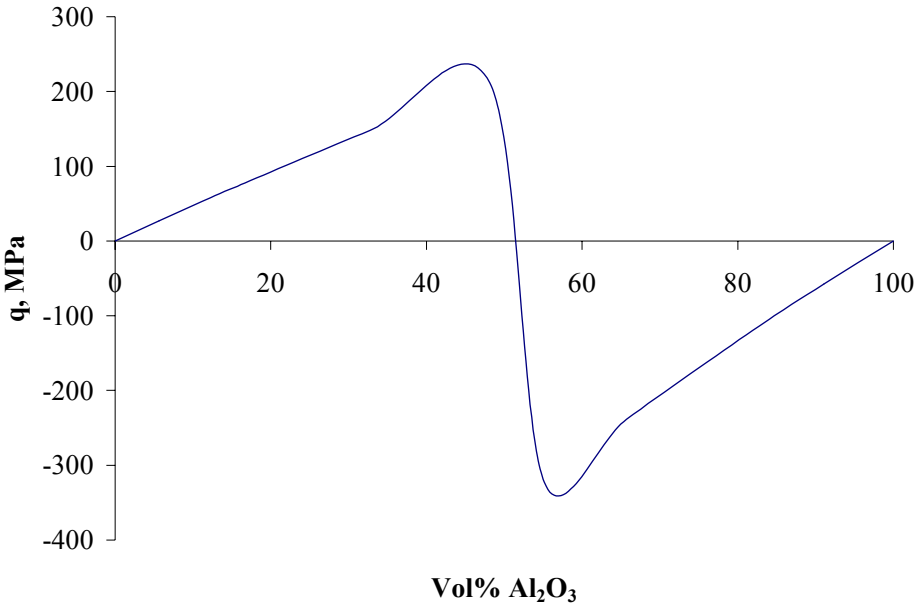

Figure 30 Film stress due to matrix/second phase CTE mismatch versus Al_2O_3 content in films.

Transmission Electron Microscopy

Because of the inability to see alumina peaks with x-ray diffraction and the small size of the second phase particles in the unannealed 62.8 mol% alumina film, transmission electron microscopy was performed. Specimen preparation was performed by thinning the substrate to ~100 µm thick with a hand grinder and 15 µm, 9 µm and 6 µm diamond polishing paper. The thinned specimen was then dimple grinded with a diamond wheel and 6 µm, 3 µm, 1 µm and 1/4 µm grit diamond paste until its center thickness was ~35 µm. Final thinning was performed using the Gatan Precision Ion Polishing System at 5 keV and a 6E milling angle. The specimen was milled until a small

hole was formed in the center of the sample. With the geometry of the ion milling at 6Eand knowing the thickness of the film was ~ 0.75 μm, it was safe to assume that the TEM results were from the film only with no substrate material in the analysis.

The TEM work detailed the small second phase particles and provided electron diffraction patterns of alumina (as well as the YSZ). Figure 31 is a TEM brightfield image showing a 62.8 mol% alumina film. The morphology of this film can be seen to have 10 nm to 20 nm sized YSZ particles (dark) in an alumina matrix (light). This film can be compared to the SEM secondary electron and backscatter electron images of the same composition film, Figure 22d. In Figure 22d, the fine morphology is barely visible, but nonetheless present as evidenced by Figure 31. Figure 32 is an electron diffraction pattern for the 62.8 mol% alumina film. The diffraction pattern shows spots in discontinuous rings which were indexed as alumina and zirconia. Figure 33 is the [G11] zone axis electron diffraction pattern for the YSZ. The diffraction pattern tilted onto the [G11] zone axis allows the {1G2}-type reflections to be seen, if the phase is tetragonal. Indexing the pattern confirmed the {1G2}-type reflections thus verifying the non-transformable tetragonal, TN, phase of zirconia.

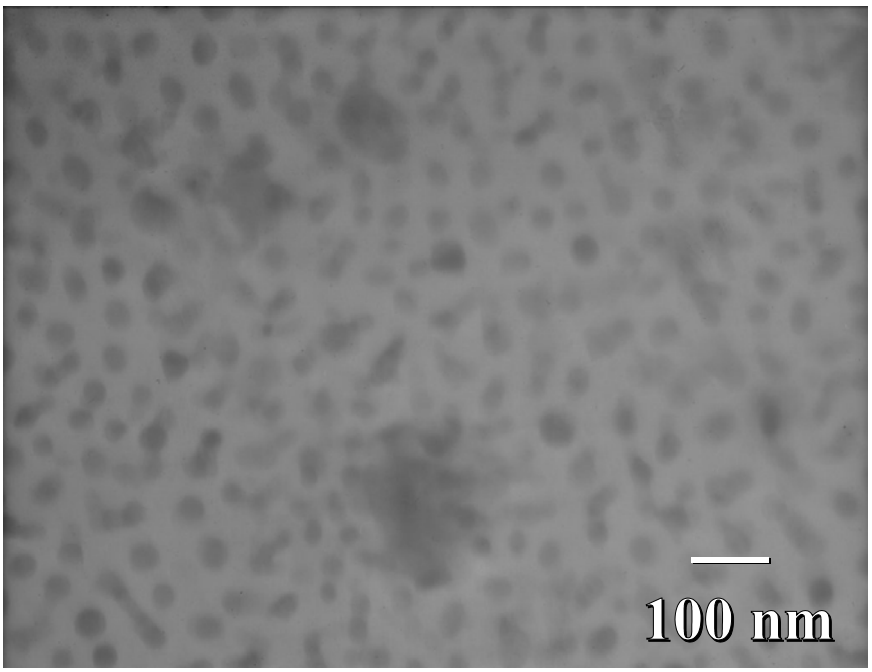

Figure 31 TEM brightfield image of 62.8 mol% alumina film showing 10 nm to 20 nm sized YSZ particles (dark) in an alumina matrix (light).

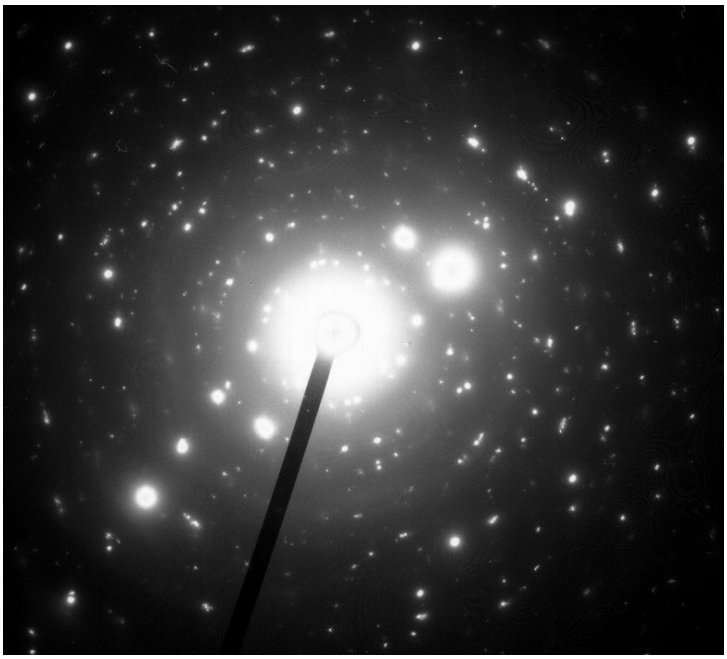

Figure 32 TEM electron diffraction pattern for 62.8 mol% alumina film.

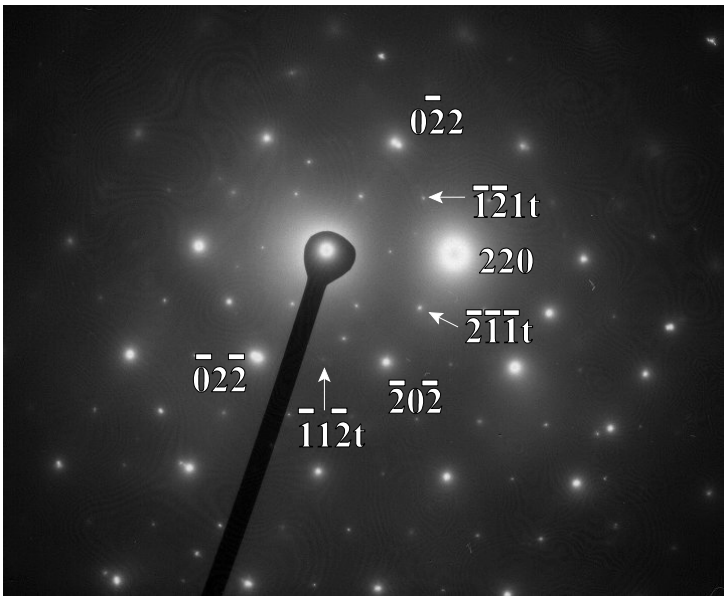

Figure 33 TEM electron diffraction pattern, [$\bar{1}\bar{1}$] zone axis for YSZ in the films.

Energy Dispersive Spectroscopy

EDS in the TEM was also used to aid in evaluation of the composition of the deposited films, see Figure 34. Quantification of the films from EDS was performed using the ZAF standardless method for alumina and YSZ. However, a standard was employed in determining the amount of yttria in the YSZ. The standard, obtained from Ceries, Inc., 202 Boston Rd, N. Billerica, MA 01862, was 9.795322 mol% Y_2O_3 (or 17.84 mol% $YO_{1.5}$) with the balance being zirconia (ZrO_2). EDS performed on a TEM specimen prepared from the standard resulted in a measured yttria content of 10.78713 mol% (or 19.47125 mol% $YO_{1.5}$).

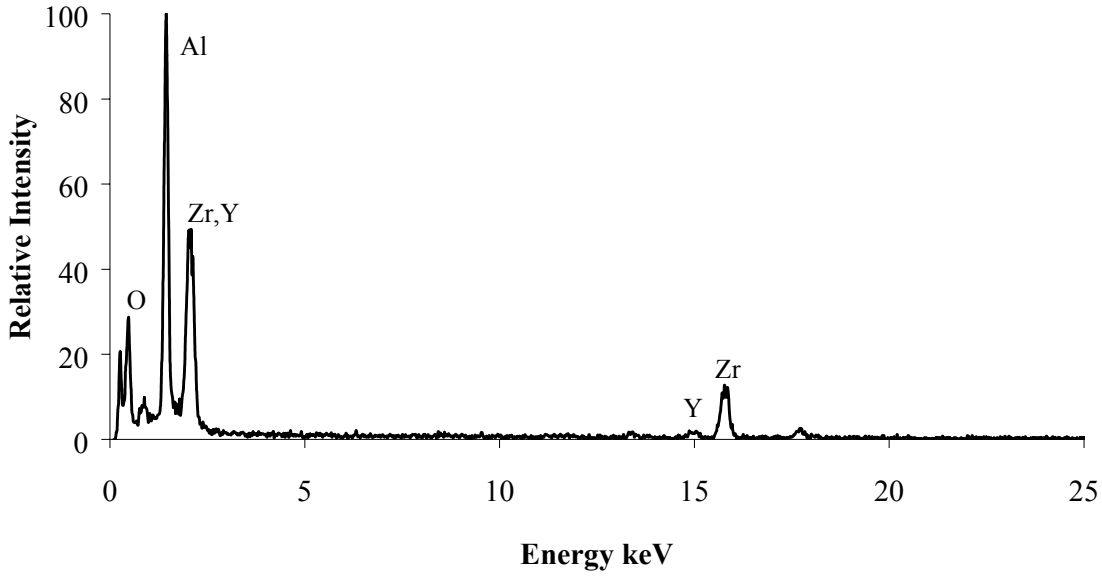

Figure 34 TEM EDS spectrum for 62.8mol% Al_2O_3 film.

The amount of yttria in the films was determined by the following linear calibration equation [55]:

$$mol\%\ YO_{1.5} = \frac{ROI_Y}{ROI_Y + ROI_{Zr}} \times \frac{17.84}{19.47} \times 100\% \qquad (31)$$

where ROI_X= Region of Interest (area under peak X) in total counts. The Kα peak was used for both yttrium and zirconium. Table 5 shows the EDS quantitative analysis results.

Table 5: TEM-EDS Quantitative Analysis

Precursor mol% Al_2O_3	mol% Y_2O_3	mol% ZrO_2	mol% YSZ	mol% Al_2O_3
0	5.70	94.30	100	0
15	6.16	93.84	85.9	14.1
30	6.64	93.36	70.5	29.5
45	7.81	92.19	54.6	45.4
62.8	6.68	93.32	36.9	63.1
80	7.76	92.24	18.9	81.1
100	0	0	0	100

Quantitative Image Analysis

Quantitative image analysis was performed on all two-phase films. Backscatter and TEM images were used for this work. For each composition the average particle size and area percentage (approximately equivalent to volume percent assuming uniform distribution of the two phases in the third dimension) were determined. For the low percentages of alumina (15, 30 and 45 mol% Al_2O_3), the second phase (alumina) was in the form of swirls as opposed to distinct particles. In these cases the calculated particle size was essentially an effective particle size, derived from the assumption that the second phase was uniformly distributed as round (spherical in three dimensions) particles.

For the compositional range studied, Table 6 shows the particle size and area percentage (~ volume percent) from quantitative image analysis along with the mole percentage determined from EDS. Table 7 shows the particle size, area percentage (~ volume percent) from quantitative image analysis and the mole percentage determined from EDS for the 1500EC anneal series on the eutectic composition. The volume percentage and area percentage had a significant standard deviation. Examination of the plan-views of these films tilted in the SEM showed that the second phase (YSZ in this case) also grew out of the plane of the alumina matrix, see Figure 35. This may account for the deviations in calculated volume percent.

Table 6: Film Composition and Particle Size via Quantitative Image Analysis and TEM-EDS Analysis

Precursor mol% Al_2O_3	Precursor vol% Al_2O_3	Particle Size, (μm)	Area % Al_2O_3 (~vol%)	TEM-EDS mol% Al_2O_3
0	0	n/a	n/a	0
15	16.7	1.27 ± 0.18	12.8 ± 4.9	14.1 ± 2.5
30	32.7	0.608 ± 0.18	28.4 ± 9.1	29.5 ± 2.1
45	48.1	0.371 ± 0.33	57.1 ± 11.0	45.4 ± 2.9
62.8	65.7	0.131 ± 0.087	69.2 ± 5.5	63.1 ± 4.4
80	81.9	0.116 ± 0.035	83.9 ± 4.5	81.1 ± 3.9
100	100	n/a	n/a	100

Table 7: Eutectic Composition Anneal Series: Particle size and Area/Volume Percentage

Precursor mol% Al_2O_3	Precursor vol% Al_2O_3	Anneal Time, (hr)	Particle Size, (μm)	Area % Al_2O_3 (~vol%)	TEM-EDS mol% Al_2O_3
62.8	65.7	0	0.131 ± 0.087	70.4 ± 3.6	63.1 ± 4.4
62.8	65.7	2.5	0.284 ± 0.078	65.5 ± 4.7	67.7 ± 1.7
62.8	65.7	5	0.435 ± 0.151	59.8 ± 4.7	65.5 ± 1.7
62.8	65.7	10	0.464 ± 0.167	68.4 ± 5.7	58.3 ± 2.1

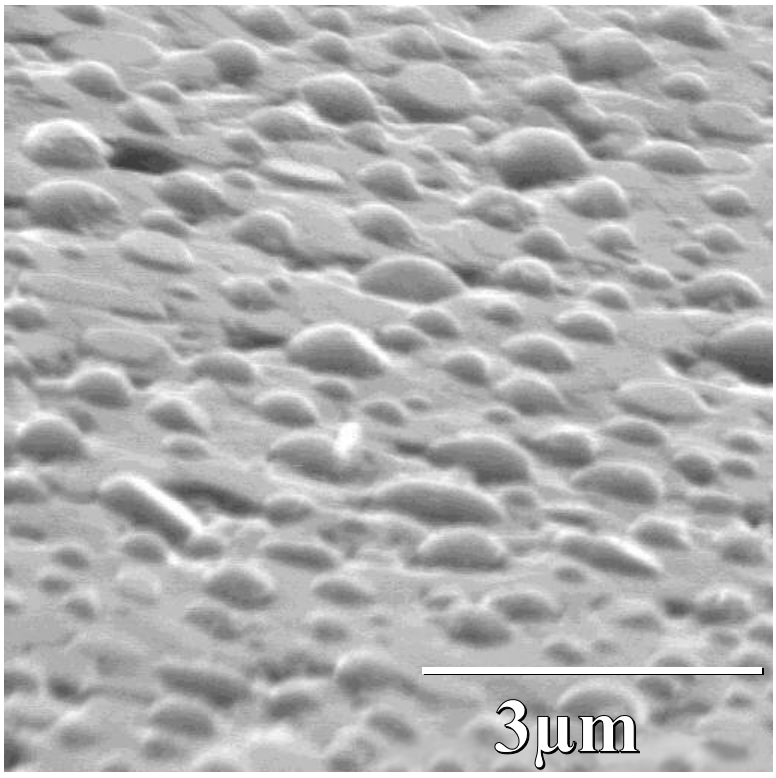

Figure 35 High angle tilt SEM image of 62.8mol% Al_2O_3 film with 10hr anneal showing the growth of the YSZ particles out of the plane of the matrix.

Nanoindentation

In presenting the results from the Nanoindenter® average values of harness, elastic modulus and fracture toughness were obtained from the numerous indents performed on each specimen. For the hardness and elastic modulus results, the average was from the fifteen indents made with the Berkovich tip. The error bars came from the different values obtained from each of the fifteen indents per sample. For example, on each particular sample, there were fifteen indents made with the Berkovich tip. Each indent produced a load-displacement curve and a hardness value and an elastic modulus value were obtained as described in the background chapter. For the fracture toughness results, the average was from the three cracks formed from each of the twenty-five indents made with the cube-corner tip. The error bars were from the different lengths of the cracks. For example, on each particular sample, there were 25 indents made with the cube-corner tip. Each indent produced up to three cracks and in turn up to three fracture toughness values.

In accordance with the equation for fracture toughness developed by Lawn et al. [47] (which was used here), not all cracks formed by an indent were used in determining the average fracture toughness for a specimen. As described in Chapter II, only "well-developed" radial cracks were measured and included, i.e. cracks shorter than ~ 2 times the indent size were excluded and lateral cracks were excluded.

Bulk Material Specimens

The mechanical properties of the films were determined via the Nanoindenter®. To provide a basis for indentation of the films, the procedure was developed by indenting various bulk material samples. Table 8 shows the bulk materials used.

Nanoindentation of these materials gave three important mechanical properties: hardness, elastic modulus and fracture toughness. As described in Chapter III, the hardness and elastic modulus were found directly from the Nanoindenter®'s load displacement curves using the continuous stiffness method. Fracture toughness determination additionally required SEM examination of each specimen to measure crack lengths. Figure 36 shows the results of the hardness and elastic modulus versus the

Table 8: Bulk Materials Tested with Nanoindentation.

Material	**Crystal Structure**
Al_2O_3 [1]	a-plane rhombohedral
Al_2O_3 [1]	r-plane rhombohedral
Al_2O_3	polycrystalline
ZrO_2 (9.5mol% Y_2O_3) [2]	cubic (100)
MgO [3]	polycrystalline
SiO_2 [4]	amorphous

[1] Saphikon Inc., 33 Powers St, Milford, NH 03055
[2] Zirmat Corp., P.O. Box 968, Westford, MA 01886
[3] Canadian Substrate Supplies Ltd., M.P.O. Box 2597, Niagara Falls, NY 14302
[4] Quartz Scientific, 819 T East St, Fairport Harbor, OH 44077

indentation depth for the bulk samples. Figures 36a and b show the six different materials tested. Figures 36c and d show three different tests of a-plane alumina and two different tests of amorphous silica; shows the repeatability properties measurements for the bulk materials. And Figures 36e and f show the a-plane alumina tested at three different orientations with respect to the cleavage plane.

All hardness and elastic modulus data from these substrates had very tight standard deviations, see Figure 36a and b. The hardness and modulus values for the three a-plane alumina were within two standard deviations from each other (numbers 1 through 3 in Figure 36c and d) as were the two silica tests (numbers 1 and 2 in Figure 36c and d). The r-plane alumina and polycrystalline alumina were also within two standard deviations from that of the a-plane alumina, as seen in Figure 36c and d.

Figure 36e and f shows the set of tests performed on a-plane alumina where the orientation of the single crystal was set at different angles from the cleavage plane: 0E, 30E and 90E. The modulus did not vary with this change of orientation, but the hardness was significantly higher (much greater than two standard deviations) for the 0E orientation compared to the 30E and 90E tests. Typical cracks measured for determination of the fracture toughness of the bulk materials can be seen in Figure 37. The resulting values of the fracture toughness are shown in Figure 38. All of the a-plane substrates produced very similar toughness values (within one standard deviation) no matter what the orientation of the indenter.

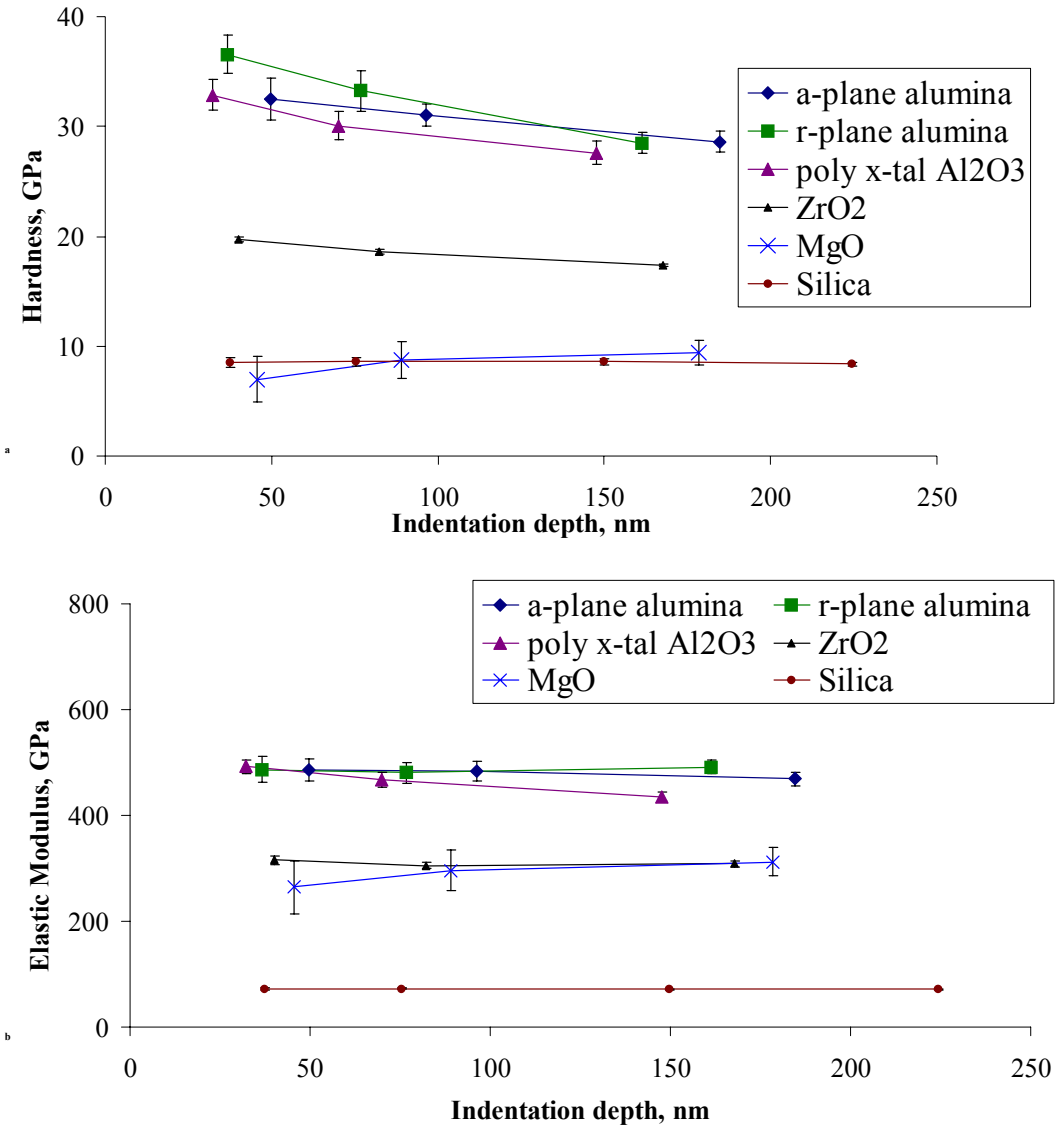

Figure 36 Hardness and elastic modulus for various substrates and substrate orientation: a) and b) comparison of different materials,

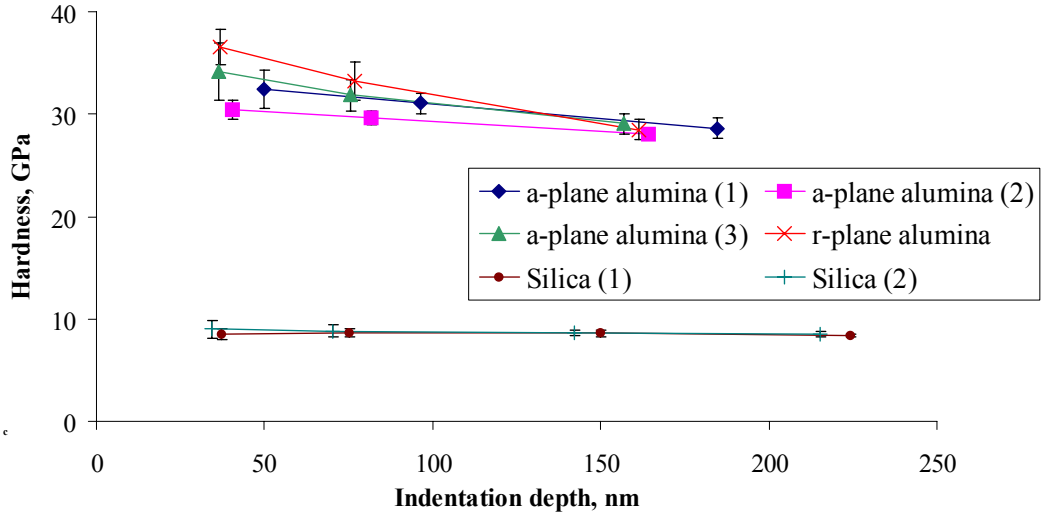

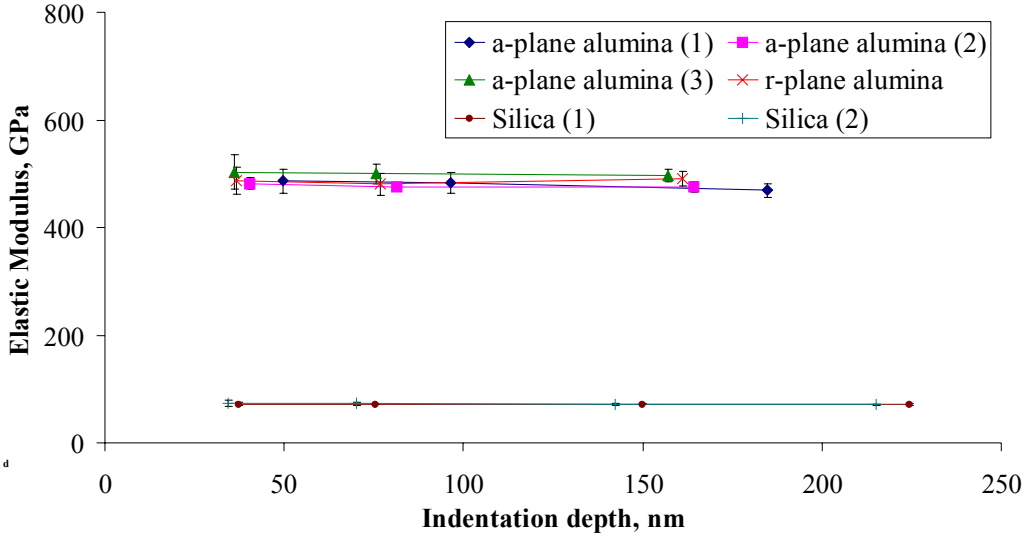

Figure 36 Continued, c) and d) comparison of repeatability,

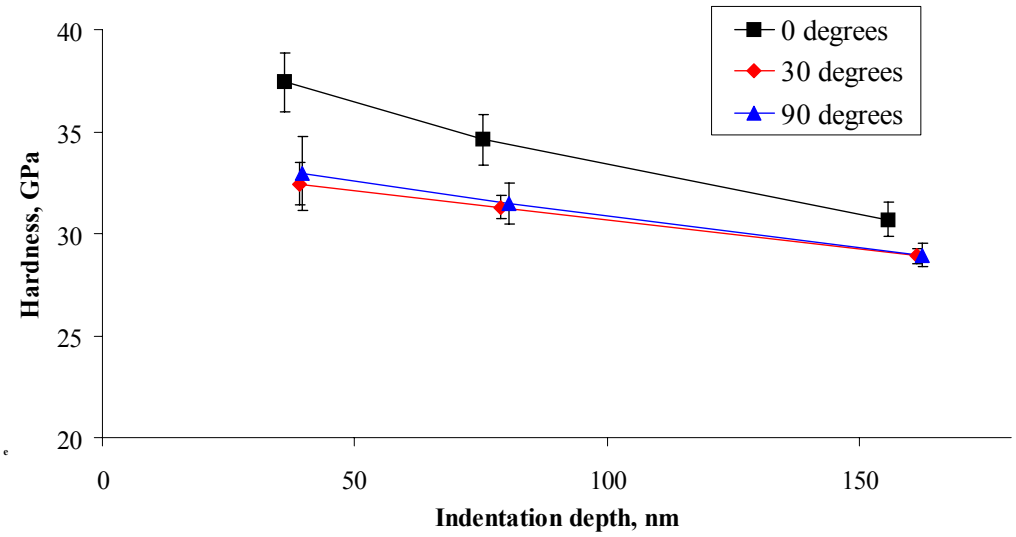

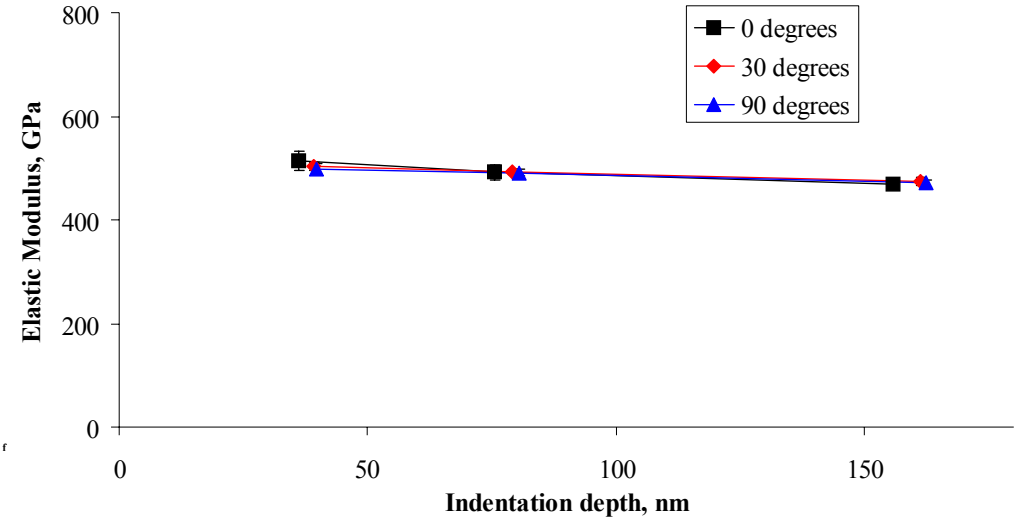

Figure 36 Continued, e) and f) comparison of three orientations on a-plane Al_2O_3.

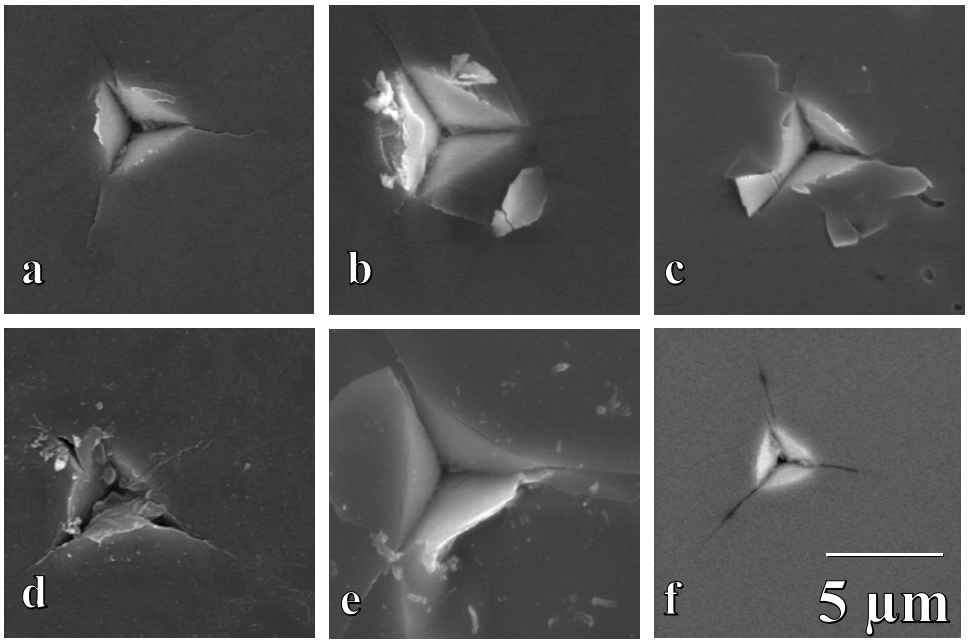

Figure 37 Indentations in substrates: a) a-plane Al_2O_3, b) r-plane Al_2O_3, c) polycrystalline Al_2O_3, d) MgO, e) amorphous SiO_2 and f) YSZ.

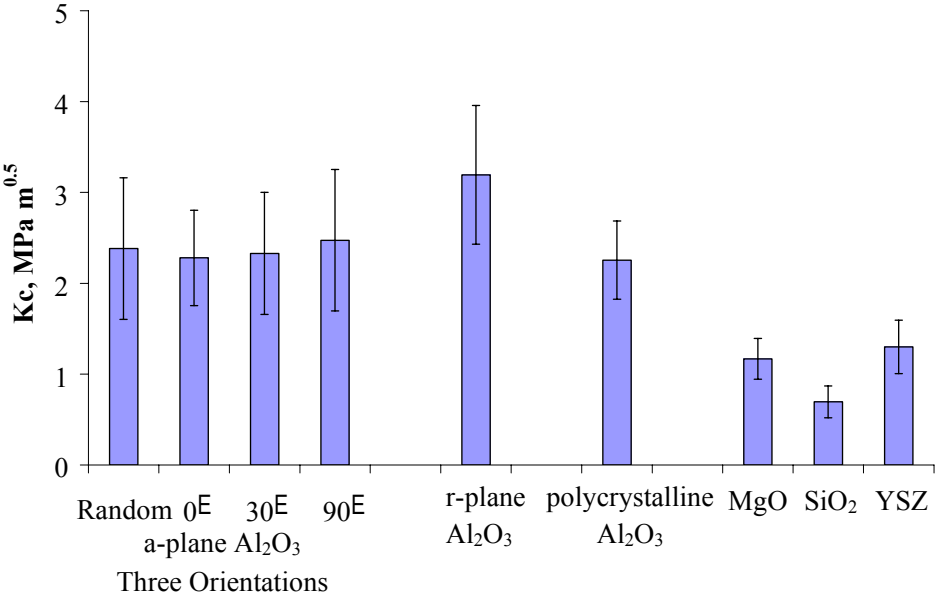

Figure 38 Fracture toughness for various substrates.

YSZ-alumina

Data from Indents: In nanoindentation it was found that certain films would produce good data while other films would result in bad data. Bad data is defined as an indent that does not produce a load-displacement that has a smooth increase in load with an increase in displacement followed by a smooth decrease in both. Figure 39 is an example of a smooth load-displacement curve, termed a 'good' indent. If the indenter encountered a pore just beneath the surface of the film, the indenter displacement would increase with no change in load. Figure 40 shows a typical load-displacement curve where this phenomenon occurred. There was a significant flat plateau region, as the indenter displacement increased without an increase in load. This load-displacement curve was an example of a 'bad' indent.

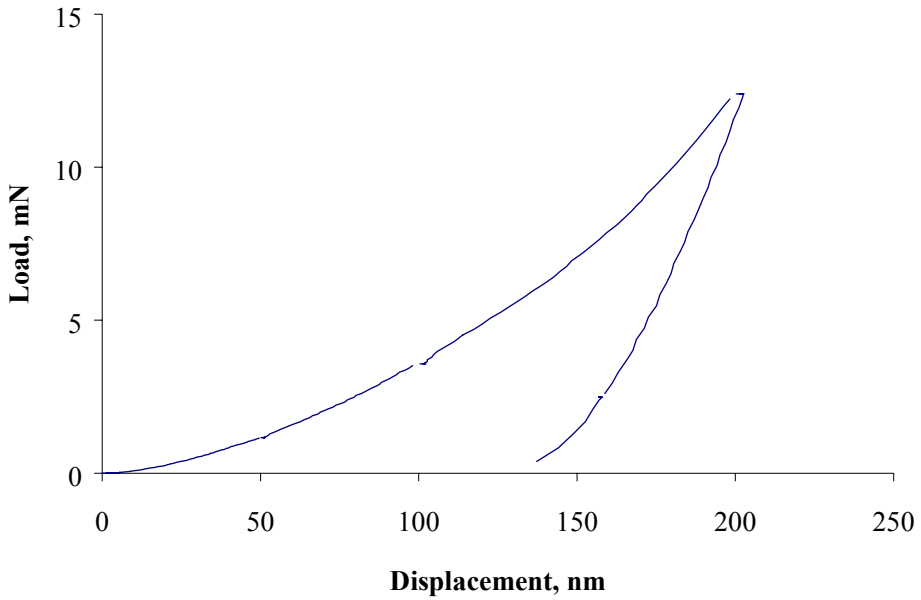

Figure 39 'Good' load-displacement curve showing a smooth increase then decrease in the load with displacement of the indenter tip.

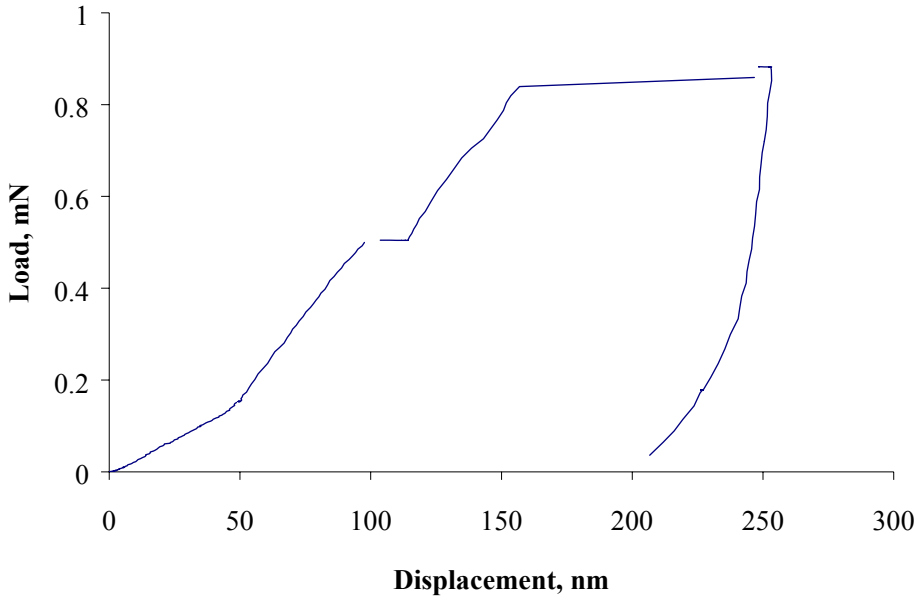

Figure 40 'Bad' load-displacement curve showing plateaus of indenter displacement without an increase in load.

Another type of 'bad' indent may be caused by significant surface roughness of the film or other discontinuity in the film, see Figure 41. This load-displacement curve showed at initial contact the indenter touched the surface, the load increased and displacement increased. Three points on the plot (approximately 45 nm, 90 nm and 175 nm indent depth) show the load decreasing as the displacement increased.

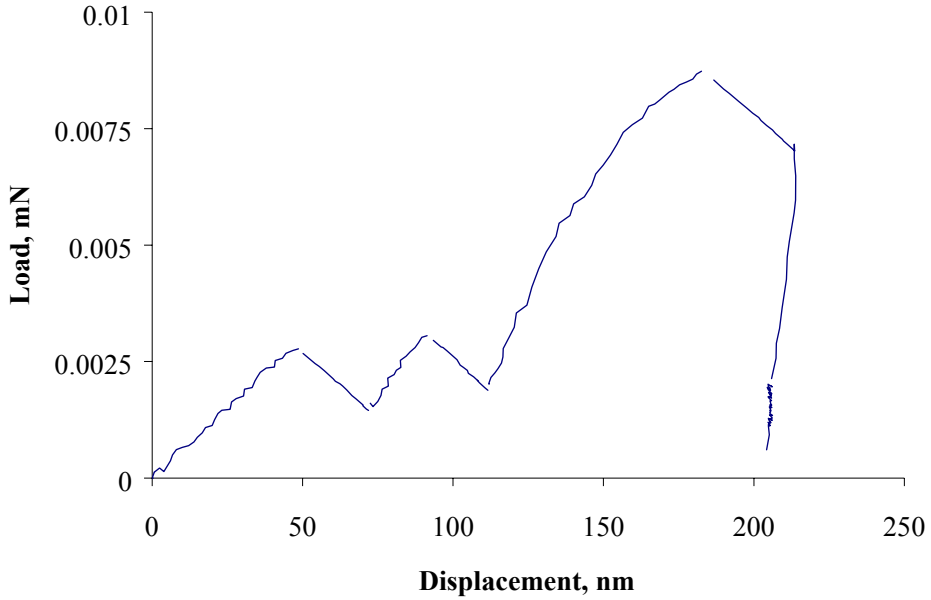

Figure 41 'Bad' load-displacement curve showing erratic behavior possibly due to slippages of the indenter tip on a rough surface or discontinuities in the film.

Solution Concentration: Figure 42 shows two films deposited under the same conditions except for the concentration of precursors in the solvent, 0.002 M and 0.005 M. The higher concentration deposition had a much rougher appearing surface. Figure 43 shows the hardness, elastic modulus and fracture toughness for these films. There was a large difference in the hardness and modulus for the two concentrations throughout the range of compositions. However, the fracture toughness was only significantly different at low amounts of alumina (0 and 15 mol% alumina) while it was the same at higher alumina content (30 and 45 mol% alumina).

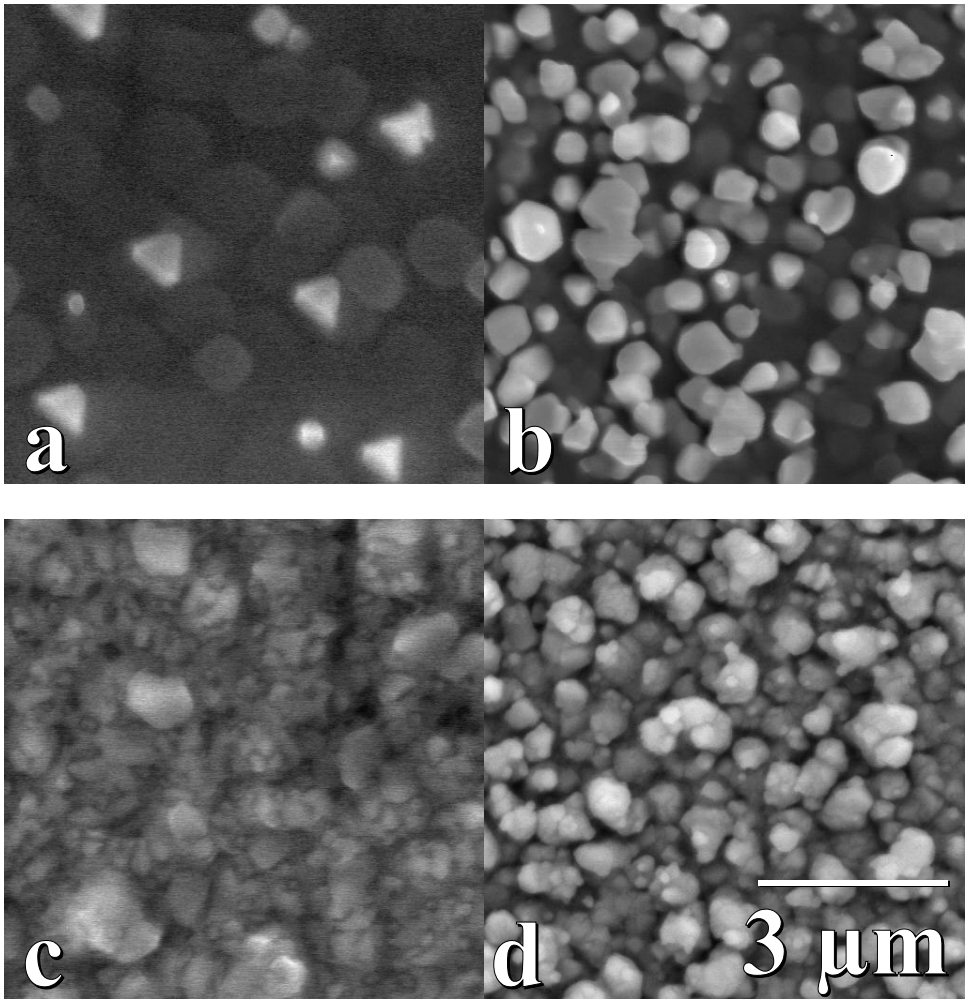

Figure 42 SEM micrograph of 100% YSZ film deposited with solution concentrations of a) 0.002M and b) 0.005M, and a 30 mol% Al_2O_3 film deposited with solution concentrations of c) 0.002M and d) 0.005M.

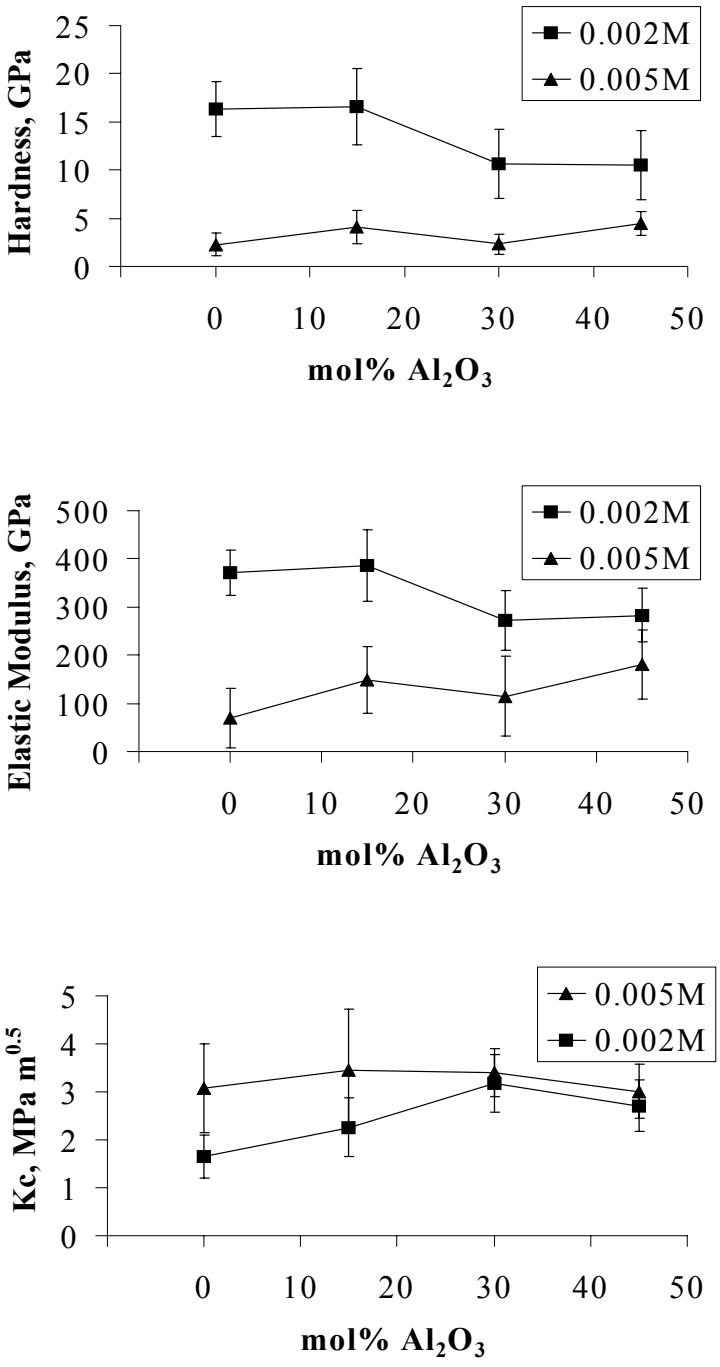

Figure 43 Hardness, elastic modulus and fracture toughness for 0.002M and 0.005M solution concentration films.

Repeatability Study: In order to determine the reliability of the deposition process and the indentation technique, five depositions each were made at two different compositions 100% YSZ and 30 mol% alumina then tested with the Nanonindenter®. The general appearance of each film (for each composition) and the thickness of each film did not vary noticeably from one to the next. The mechanical properties of each film did have slight variations as can be seen in Figures 44 and 45.

Figure 44 shows the hardness, elastic modulus and the fracture toughness determined from nanoindentation for the five 100% YSZ films (numbered 1 through 5). Figure 45 shows the same properties but for the 30 mol% alumina films (numbered 1 through 5).

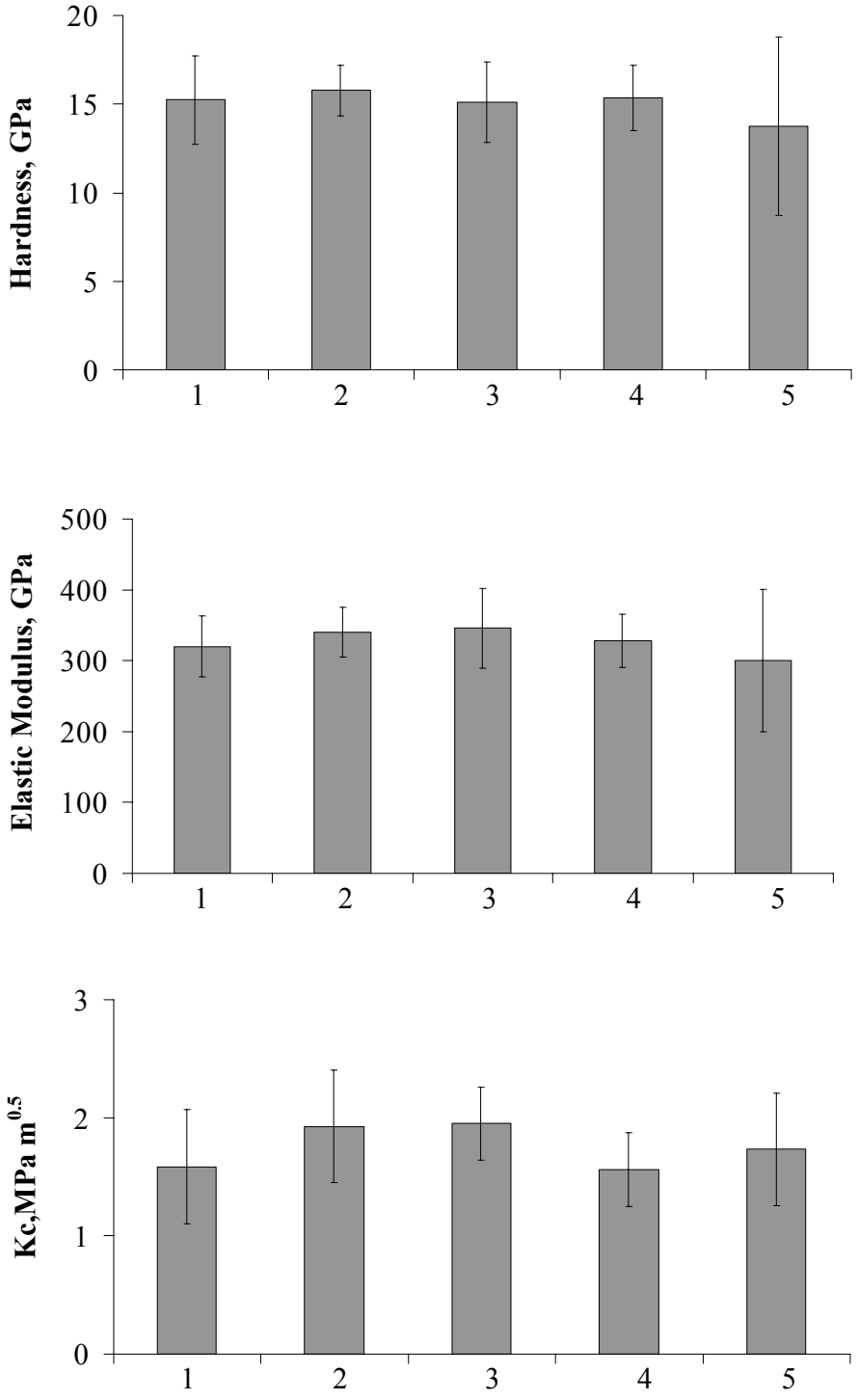

Figure 44 Hardness, elastic modulus and fracture toughness for 100% YSZ films.

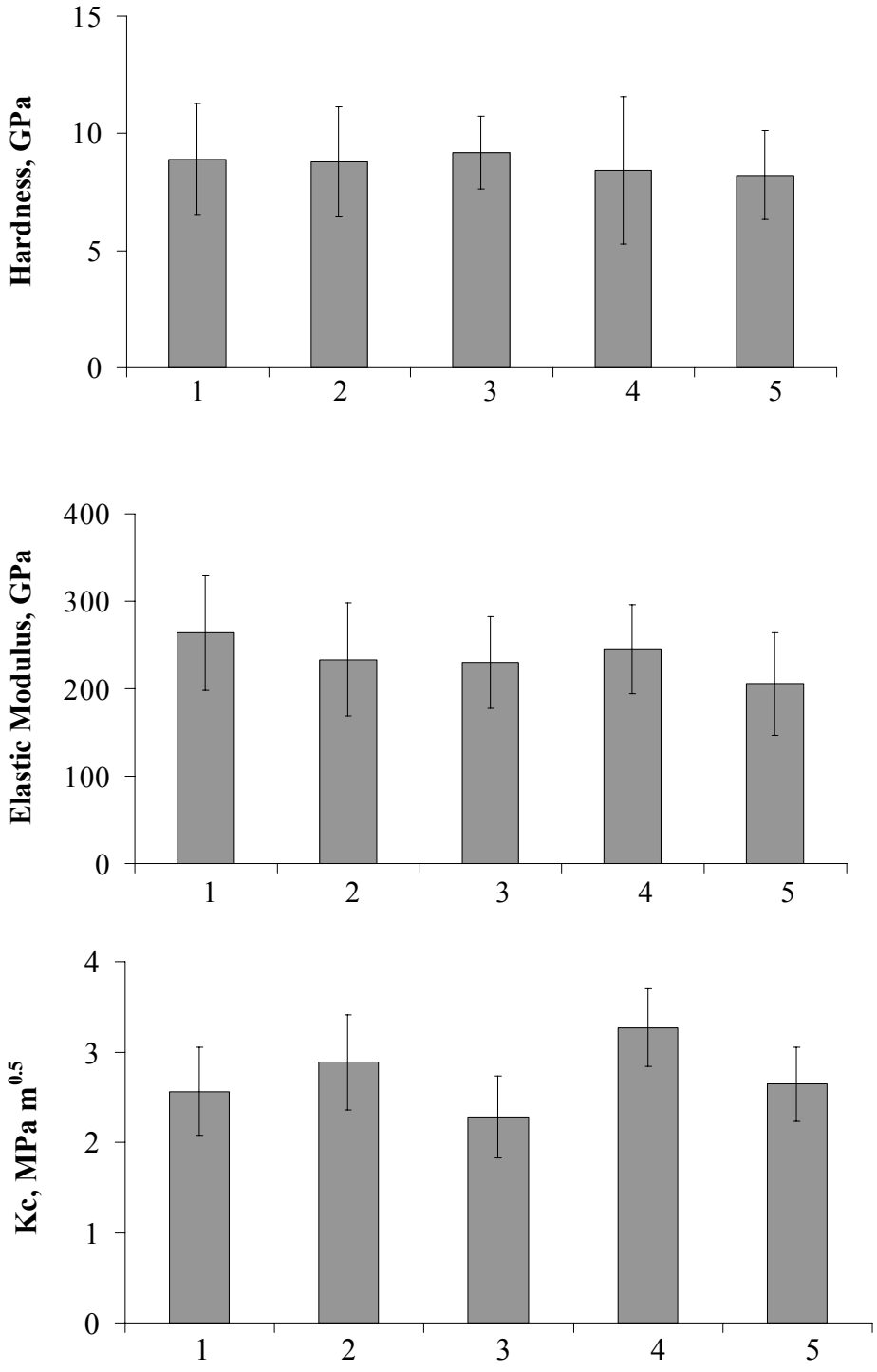

Figure 45 Hardness, elastic modulus and fracture toughness for 30mol% Al_2O_3 films.

Anneal Series: For the 1500EC annealed series of films deposited at 62.8 mol% alumina (the eutectic composition of YSZ-alumina), the resulting fracture toughnesses are shown in Figure 46. It was found that the fracture toughness increases significantly as the particle size increases and then drops suddenly near the 0.45 μm particle size (between the 5 hr and 10 hr anneals).

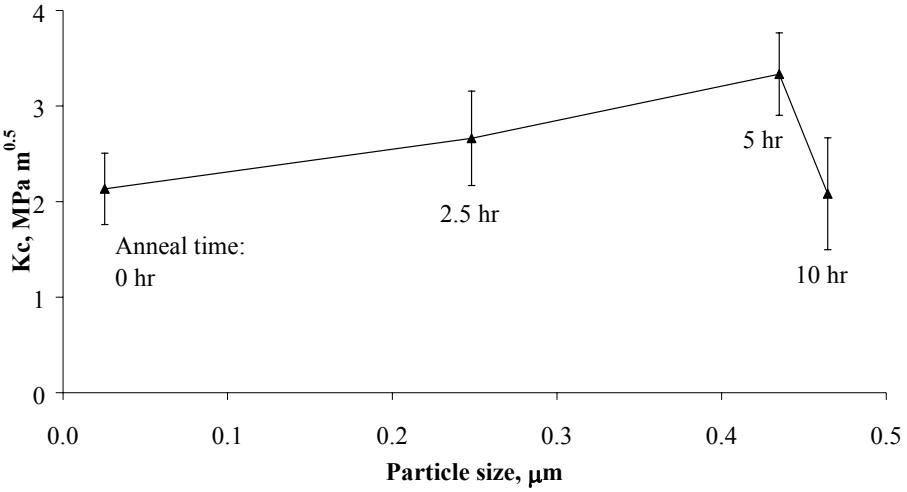

Figure 46 Fracture toughness of 1500EC annealed series of 62.8 mol% Al_2O_3 films.

Compositional Study: Mechanical properties for the full series of YSZ-alumina compositions are shown in the next few figures. Typical images of the indents and cracked films made by the cube-corner tip are shown in Figure 47. The cracks in the 100% YSZ and the 15 mol% alumina films are easily visible, see Figure 47a and b. The resolution of the images here make it difficult see the cracks for the other compositions.

Figure 48 presents the hardness and modulus values extracted from the load-displacement curves and the CSM technique as described in Chapter II versus indentation depth. These figures show that there was not much variation in properties with the depth of the indentations. For the hardness, the100% alumina composition was the only composition that changed more than a standard deviation from the shallowest indent depth to the deepest. All other compositions were well within one standard deviation for all indent depths. For the elastic modulus, each composition except the 100% alumina composition increased (nearly one standard deviation) as the indentation depth increased.

Figure 49 is the hardness and modulus versus alumina content. Both of these properties values decreased slightly then rose as the alumina content increased. This was very significant in the hardness results as opposed to the elastic modulus. Figure 50 provides the final results of the fracture toughness data, which were the average of results from two sets of specimens. It is observed that the toughness increases to a maximum at 30 mol% alumina where it reaches a plateau and decreases slowly to 100% alumina.

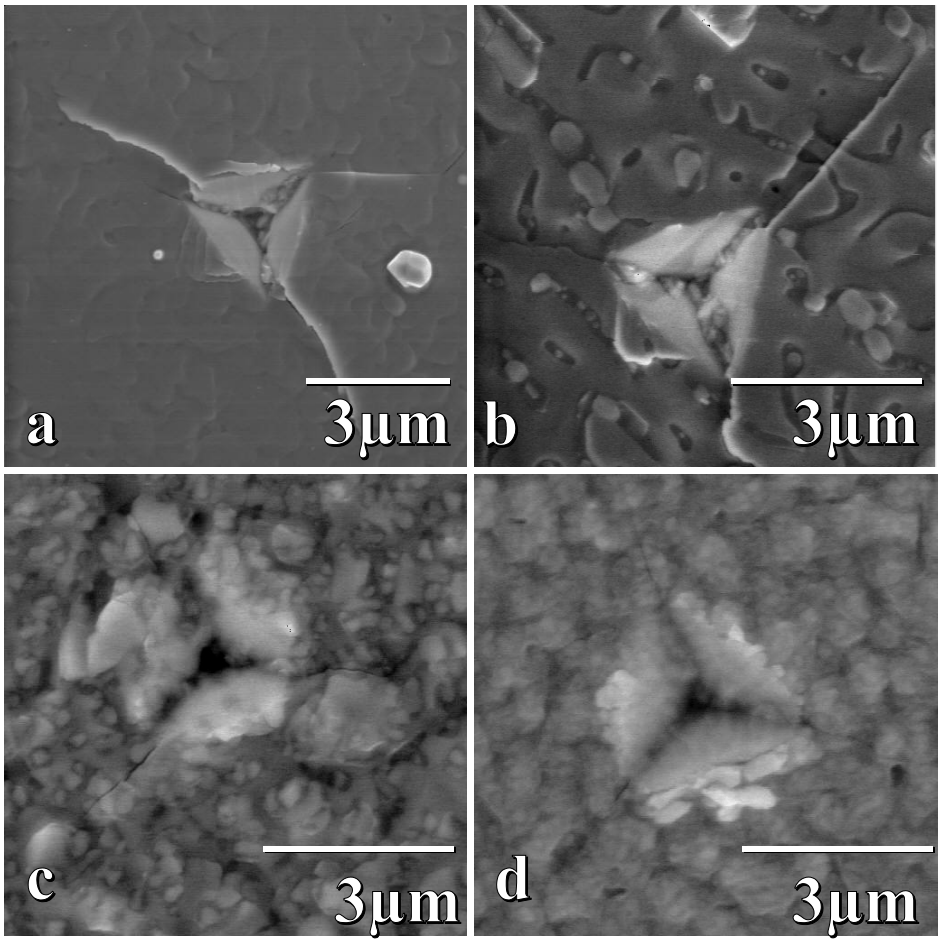

Figure 47 SEM micrographs of cube-corner indentations in YSZ-alumina films; a) 100% YSZ, b) 15 mol% Al_2O_3, c) 30 mol% Al_2O_3, d) 45 mol% Al_2O_3,

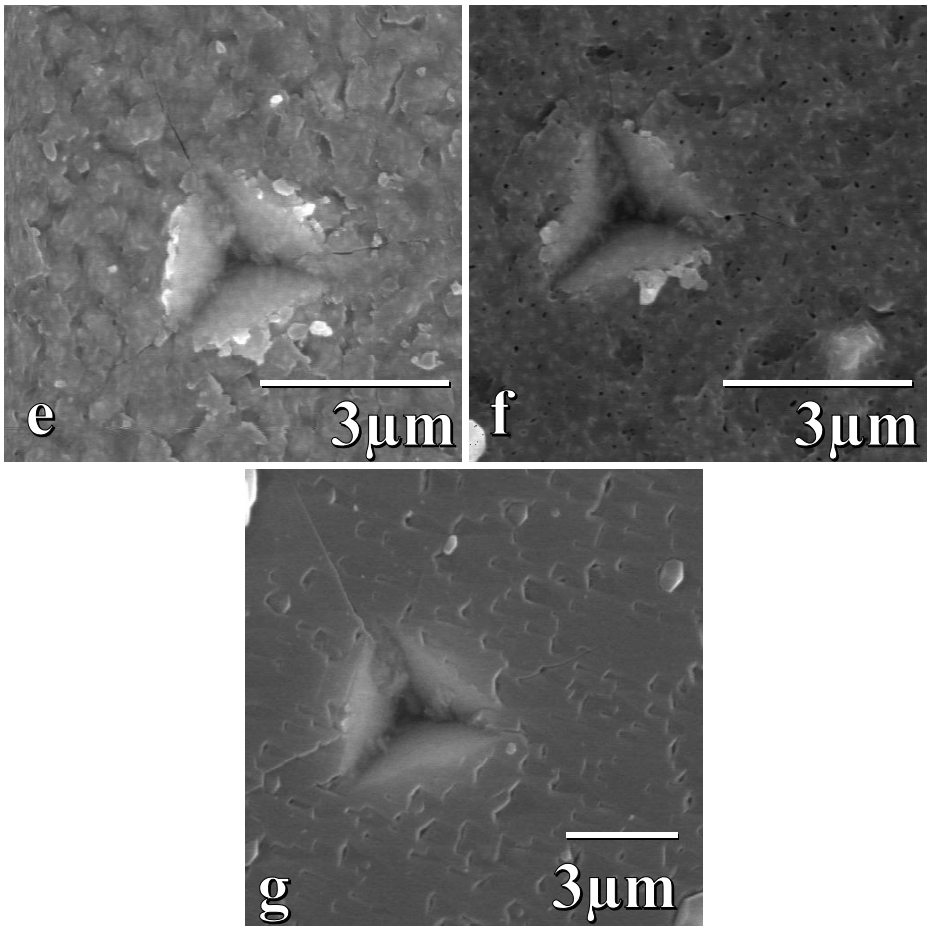

Figure 47 Continued, e) 62.8 mol% Al_2O_3, f) 80 mol% Al_2O_3, and g) 100 mol% Al_2O_3.

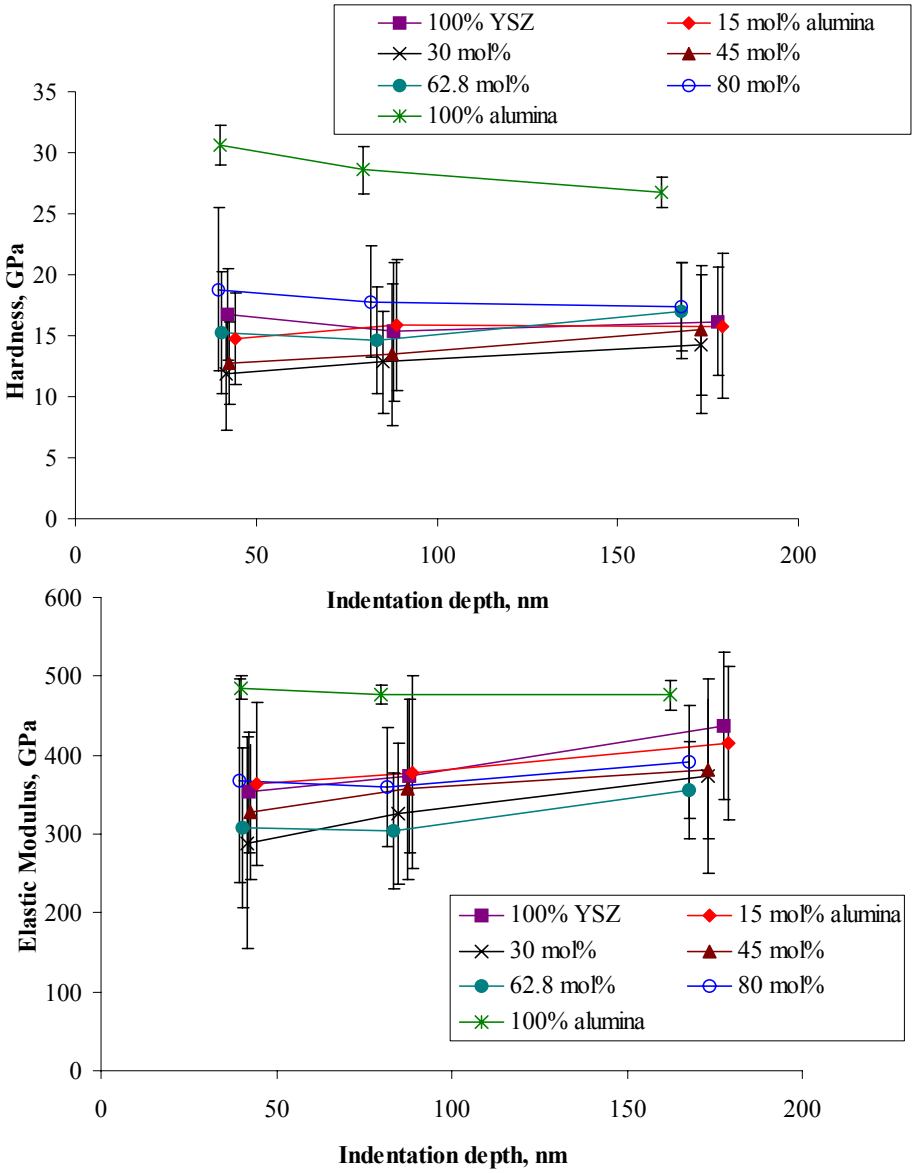

Figure 48 Hardness and elastic modulus vs indentation depth for entire compositional range studied.

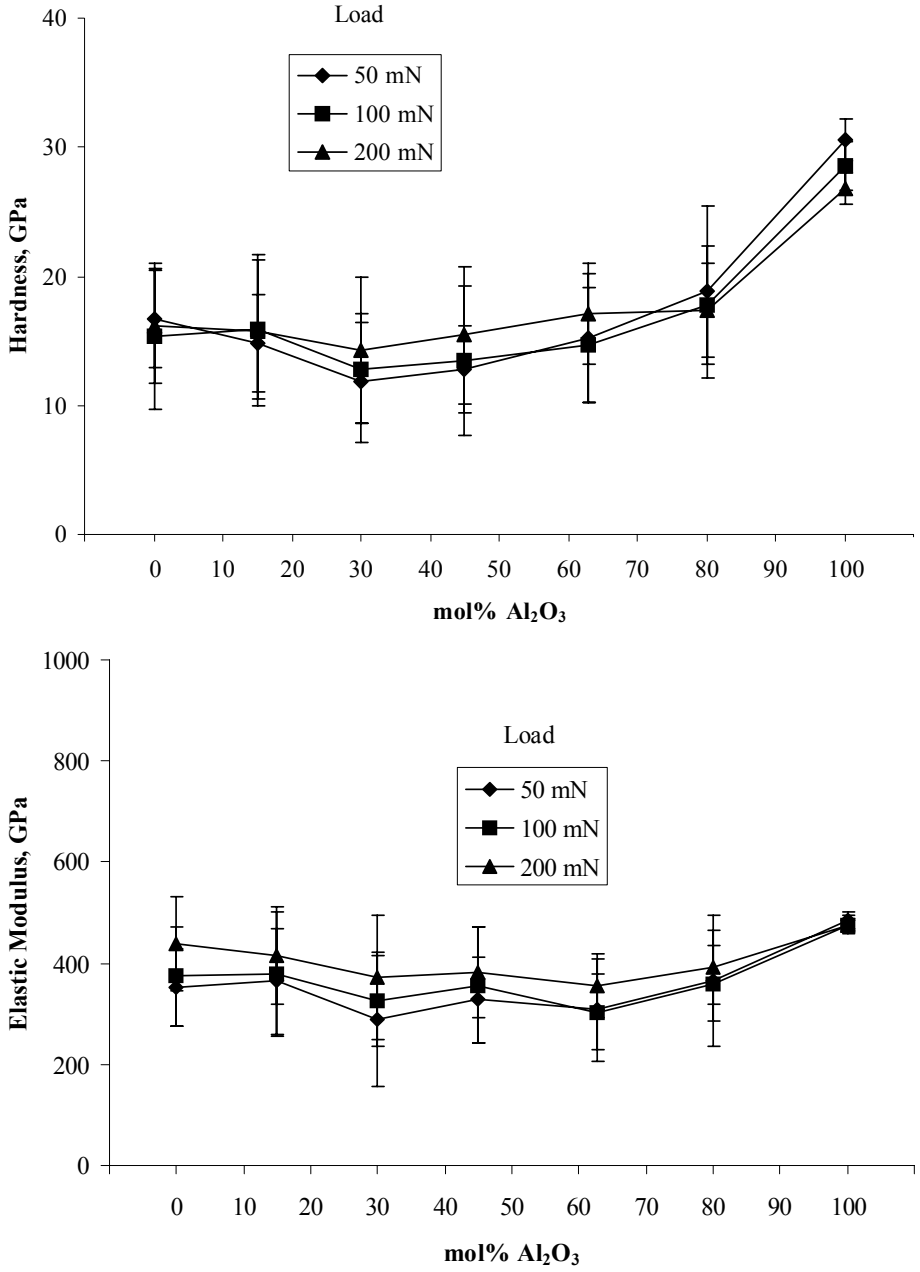

Figure 49 Hardness and elastic modulus vs the Al_2O_3 amount in the film for entire compositional range studied.

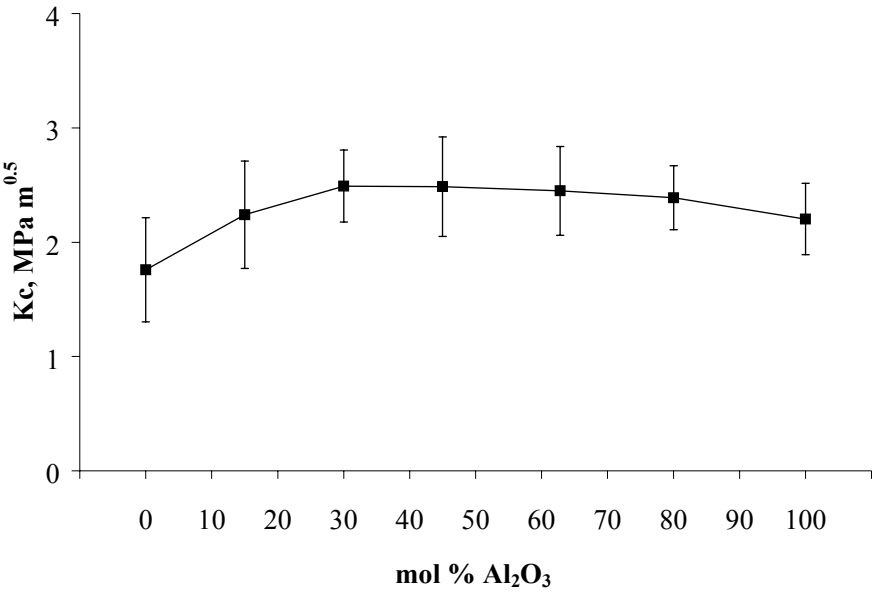

Figure 50 Fracture toughness vs the Al_2O_3 amount in the film for entire compositional range studied.

Confidence in Fracture Toughness Data

Because of the significant standard deviations found with the fracture toughness data there was concern regarding the reliability of the data. To provide additional confidence in the measured data, the distribution of the fracture toughness values for each composition was plotted to determine that the data was a normal distribution (Gaussian) and not bi-modal or multi-modal. Figure 51 shows the results of these histograms. Although the sample sizes were not large for a few of the compositions, the results were fairly normal in distribution.

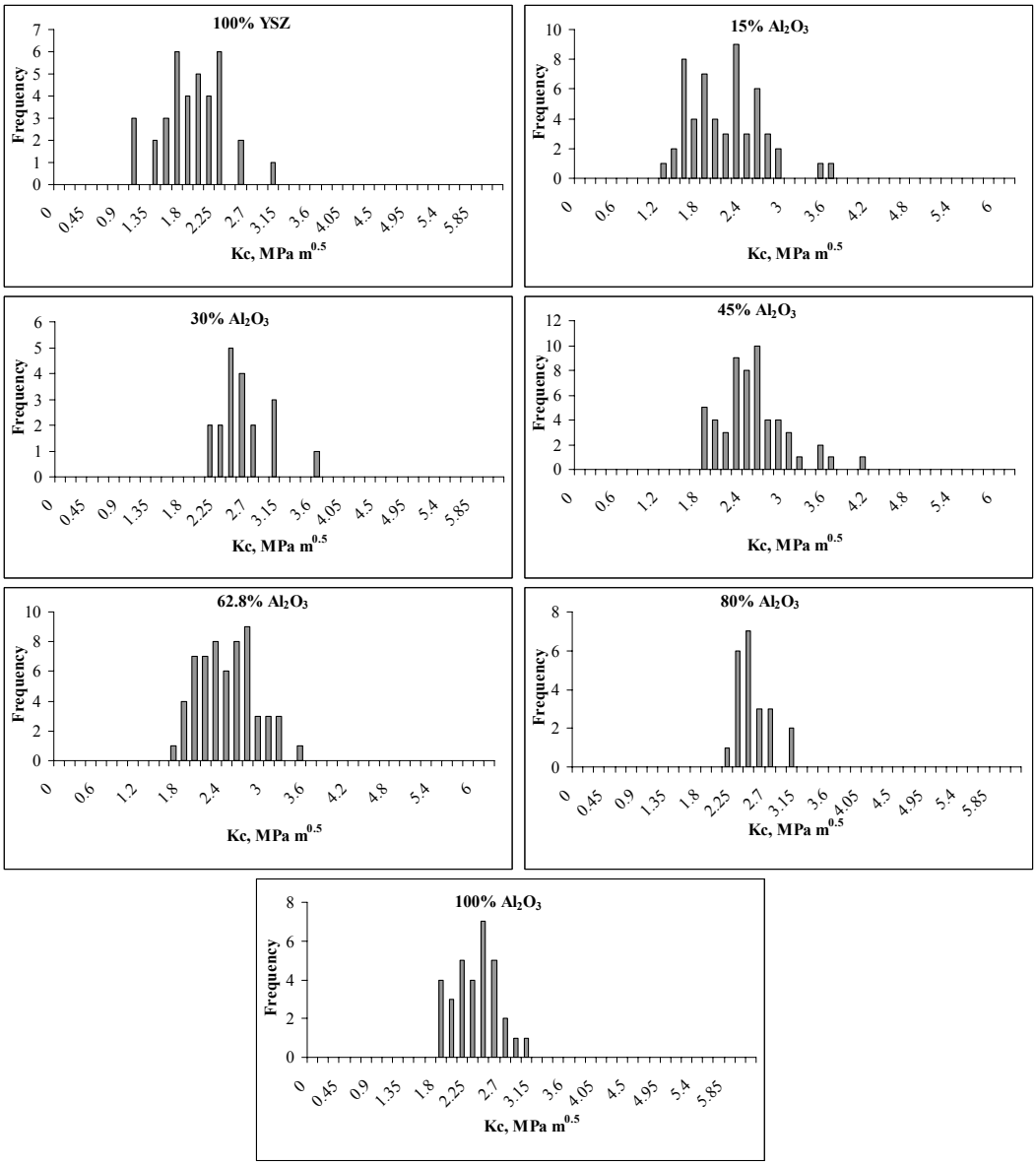

Figure 51 Histograms showing frequency of indentations with certain fracture toughness for each Al_2O_3 composition.

The second step in testing the confidence of the data was the reliability test (t-test). A t-test was performed on the data to determine if the average fracture toughness at

one composition was indeed significantly different from the fracture toughness at other compositions. The following paragraphs detail the t-test form that assumes the variances of two ranges of data are unequal (it is referred to as a heteroscedastic t-test). The statistics involved require the testing of a hypothesis, H_o, and either the acceptance of that hypothesis or the rejection of the hypothesis in favor of an alternate hypothesis, H_a. Given that μ_1, μ_2 are the means for two ranges of data, the two hypothesis are the following:

H_o: $\mu_1 = \mu_2$ or H_o: $\mu_1 - \mu_2 = 0$ i.e., there is no significant difference in the means,

H_a: $\mu_1 \neq \mu_2$ or H_o: $\mu_1 - \mu_2 \neq 0$ i.e., there is a significant difference in the means.

The test statistic $(\mu_1 - \mu_2)$ was transformed into a t-score, t_{ov}, by the following equation:

$$t_{OV} = \frac{\left(\bar{x}_1 - \bar{x}_2\right) - \left(S_1 - S_2\right)}{S_p\sqrt{\frac{1}{n_1} + \frac{1}{n_2}}} \tag{32}$$

where S_1, S_2 = standard deviation for each range of data,

n_1, n_2 = sample sizes for each range of data,

S_p = pooled standard deviation (weighted average of the standard deviations of the two ranges of data). The pooled standard deviation was given by the next equation:

$$S_p = \sqrt{\frac{\left(n_1 - 1\right)S_1^2 + \left(n_2 - 1\right)S_2^2}{n_1 + n_2 - 2}} \tag{33}$$

To test the hypothesis, the observed t-score, t_{ov}, was compared to the critical t-score, t_{cv}, from the known statistical tables for the t-test. In order to determine the critical t-score, t_{cv}, the degrees of freedom, *dof*, and a confidence level were chosen. The degrees of freedom for the t-test is usually given as $n_1 + n_2 - 2$, but because the variances (S_1^2 and S_2^2) or standard deviations (S_1 and S_2) were not equal, *dof* was actually smaller. The following equation was used instead

$$dof = \frac{\left(\frac{S_1^2}{n_1} + \frac{S_2^2}{n_2}\right)^2}{\frac{\left(S_1^2/n_1\right)^2}{n_1 - 1} + \frac{\left(S_2^2/n_2\right)^2}{n_2 - 1}} \tag{34}$$

A commonly accepted confidence level is 95%, which implies that the level of significance, α, is 5%. Because the hypothesis was only concerned that the two means were different, a two-tailed test was used. Had the hypothesis been such that the concern was if the second mean was larger than the first, then a one-tailed test would have been used. Using α = 0.05 (or 0.025 for each tail) and the degrees of freedom from equation (34), the tables provided the critical t-score, t_{cv}.

The final determination of the t-test was performed by comparing the two t-scores, t_{ov} and t_{cv}. If $|t_{ov}| > |t_{cv}|$ then H_o was rejected and H_a was accepted; i.e. there was a significant difference in the means of the two ranges of data. However if $|t_{ov}| < |t_{cv}|$ then

H_o was retained and H_a was rejected; i.e. there was no significant difference in the means of the two ranges of data.

Applying the t-test to the repeatability study, it was found that the hardness and elastic modulus that were measured were found to be statistically the same (using the t-test) for each of the five different depositions at each composition. However, the fracture toughness values for the set of five films for both compositions were somewhat different, refer to Figures 44 and 45. For the 100% YSZ set, the fourth deposition was found to be statistically different (using the t-test) from the second and third depositions but was statistically the same as the first and fifth depositions. For clarity, Table 8 shows the fracture toughness combinations that were the same or different. For the 30 mol% alumina see Table 10 for the comparison chart of the t-test. The first deposition was different from the fourth but statistically the same as the second, third and fifth. However, the second and third were found to be statistically different.

Table 9: 100% YSZ Fracture Toughness Repeatability Comparison Chart

Deposition Number	1	2	3	4	5
1	n/a	S	N	S	S
2	S	n/a	S	N	S
3	N	S	n/a	N	S
4	S	N	N	n/a	S
5	S	S	S	S	n/a

S = average Kc's were statistically the same
N = average Kc's were not statistically the same

Table 10: 30 mol% Alumina Fracture Toughness Repeatability Comparison Chart

Deposition Number	1	2	3	4	5
1	n/a	S	S	N	S
2	S	n/a	N	N	S
3	S	N	n/a	N	N
4	N	N	N	n/a	N
5	S	S	N	N	n/a

S = average Kc's were statistically the same
N = average Kc's were not statistically the same

Applying the t-test to the compositional study fracture toughness data, it was found that in the steep portions of the curve, Figure 50, neighboring compositions had fracture toughness data that were significantly different; i.e. 0% alumina compared to 15% and 80% to100%. For the flat part of the curve neighboring compositions' fracture toughness's were not statistically different; however the t-test did show that for several composition combinations the data were significantly different; i.e. 0% compared to 30%, 15% to 45% and 62.8% compared to 100%. Additionally for the two samples tested at each particular composition, it was found that their means were not significantly different. Table 11 is a comparison table showing the fracture toughness results of the t-test between each of the various compositions.

Table 11: Compositional Study Fracture Toughness Comparison Chart

mol% Al_2O_3	**0**	**15**	**30**	**45**	**62.8**	**80**	**100**
0	n/a	N	N	N	N	N	N
15	N	n/a	S	N	N	N	S
30	N	S	n/a	S	S	S	N
45	N	N	S	n/a	S	S	N
62.8	N	N	S	S	n/a	S	N
80	N	N	S	S	S	n/a	N
100	N	S	N	N	N	N	n/a

S = means were statistically the same
N = means were not statistically the same

CHAPTER V

DISCUSSION

Primary Goal

The primary goal of this research was to use nanoindentation to determine the relationship between the mechanical properties, in particular the fracture toughness, and the amount of alumina present in combustion CVD grown YSZ-alumina thin films. To achieve this, the relationship of the combustion CVD process parameters with the amount of alumina in the YSZ-alumina films, the film grain size, the film morphology, and the films' mechanical properties was also studied. Finally, the mechanical properties of several bulk materials were measured.

Deposition Parameters

Optimization of the deposition parameters for obtaining quality films required performing many depositions. The goal was to obtain the smoothest, densest-appearing films possible such that the nanoindentation results would be reasonable and acceptable; the details of this are discussed in the following pages. Considering the numerous trials and problems, the SEM micrographs show that the films at each composition were relatively smooth with no apparent voids, see Figures 21 and 22.

The two most difficult deposition parameters to control were the aerosol size and the temperature. The aerosol size was controlled with a proprietary nozzle, so the details cannot be discussed here. But, in general, the problem was the nozzle would clog after several depositions. For each new nozzle tip the settings for an optimum aerosol size distribution were slightly different. The procedure for obtaining the optimum aerosol size was also not ideal, such that each nozzle tip probably produced a unique aerosol size distribution. This resulted in the fact that each different nozzle tip produced a slightly different flame behavior.

The other difficult parameter to control was the temperature of the deposition. At least two different temperatures were measured during each deposition, the flame temperature just above the substrate and the substrate temperature. Theses temperatures differed somewhat; for example, a deposition at a substrate temperature of 850EC would correspond to a flame temperature above the substrate of 1350EC. The substrate temperature was measured by a thermocouple attached to the substrate with Ceramabond, a high-temperature ceramic adhesive. The substrate temperature was used as the guide for depositions. It was a more reliable measure for the deposition, varying only on the order of ± 10EC while the flame temperature measured above the substrate varied ± 50EC.

Characterization

Scanning Electron Microscopy

Film Thickness: The deposition rates for the films were determined by dividing the average film thickness obtained at several points on SEM cross-sectional images by the total deposition time. The error involved in measuring the thickness was dependent on the resolution of the SEM image. The resolution was approximately 0.05 μm. Film thicknesses were on the order of 0.7 to 1.0 μm for the entire compositional range studied. The interface of the film with the substrate was very distinct for the YSZ and YSZ-alumina films, but this was not so for the pure alumina film. This was expected because both the film and the substrate were the same material, alumina. It was believed that the film was growing epitaxially, which resulted in the indistinct interfaces found in the SEM micrographs. Because of the poor resolution, the thickness of the film could not be determined accurately for the 100% alumina film; therefore the deposition rate for the 100% alumina film is not considered to be a very reliable result.

As mentioned in Chapter II, the thickness of the film was required to be at least 5 to 10 times the indentation depth in order to prevent any influence from the substrate on hardness or elastic modulus data [34]. The indentation depths for the mechanical properties measurements from the Nanoindenter® were from 45 nm for the shallowest portions of the load displacement curve used in determining the hardness and elastic modulus to 710 nm used for some of the heavier loaded cube-corner indentations for

determination of fracture toughness. Compared to the film thickness were 0.7 to 1.0 μm, there was no expected substrate influence on the hardness or elastic modulus. The effect of the substrate on the fracture toughness determination was unknown. However, it was found, for the most part, all the films' fracture toughnesses were not a function of indent load. Regardless, the shallowest indents were still used as much as possible for fracture toughness determination in order to avoid potential for substrate influences.

Anneal Series: During the deposition of the eutectic composition (62.8 mol% alumina) it was noted that the temperature had a significant effect on the final microstructure. The higher the deposition temperature, the more distinct the two phases and the larger the size of the second phase (YSZ) particles. In order to aid in quantifying this phenomenon, subsequent depositions were made at different temperatures. However, this proved nonproductive because of the difficulties in controlling the deposition temperatures. Instead, a series of anneals was performed to help quantify the growth of the second phase particles. First it was found that the films were stable when annealed at temperatures below 1450EC. Both an anneal at 1200EC for 12 hrs and at 1450EC for 24 hrs were exhibited no noticeable change in the microstructure. It was found that at 1500EC there was noticeable changes in the size and distribution of the second phase particles in the alumina matrix. A series of anneals at 1500EC was then performed for 2.5 hrs, 5 hrs and 10 hrs; the SEM micrographs of these films were shown in Figure 24.

Quantitative analysis of the resulting films showed that the particle size grew as the anneal time increased as did the inter-particle spacing (nearest neighbor distances). This phenomenon is known as coarsening. To analyze the coarsening the natural log of the particle size radius was plotted versus the natural log of time, see Figure 53. The slope of this plot provided the indication as to the controlling mechanism for the coarsening. A slope of ½ is interface-controlled while a slope of ⅓ is diffusion-controlled. The slope of the data in Figure 53 is 0.452 which lies in between ½ and ⅓. Spherical particles are an indication of diffusion-controlled coarsening, however the best fit line's slope was somewhat closer to interface-controlled coarsening of ½. The rate equation follows the following form with the power of the rate equation as the inverse of the slope from the ln r vs ln t plot (diffusion-controlled coarsening rate equation is shown):

$$r^3 - r_0^3 = kt \tag{35}$$

where r and r_0 (μm) are the particle size radius and initial particle size radius respectively, t (hrs) is time and k (μm^3/hr) is the rate constant for diffusion-controlled coarsening. Plotting equation (35) results in a coarsening rate constant of 0.0013 μm^3/hr for diffusion-controlled or 0.0055 μm^2/hr for interface-controlled as seen in Figure 52. The measured data seems to fit the diffusion-controlled coarsening rate better than the interface-controlled. However, these results may not be accurate because of the few data points

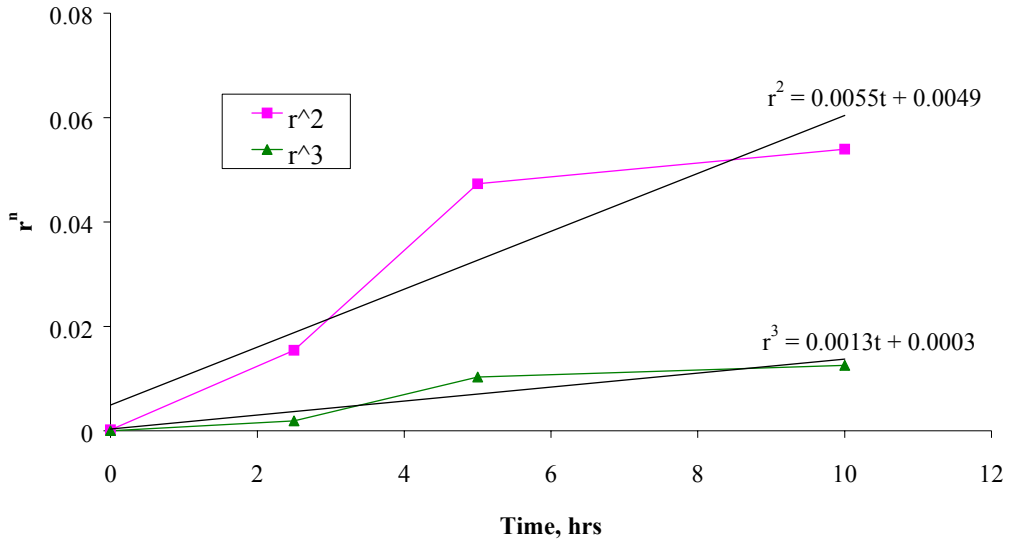

Figure 52 1500EC anneal series coarsening rate plot, particle radius, r^n versus anneal time, t.

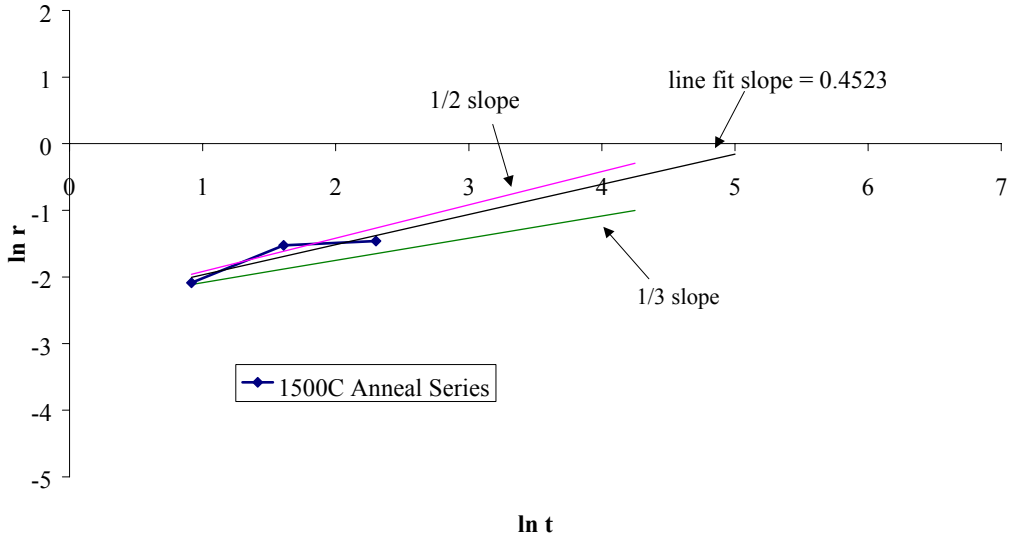

Figure 53 1500EC anneal series logarithmic plot of particle radius, r, versus anneal time, t.

available for the plots. Additional data points should be acquired to provide more accurate data on this coarsening phenomenon.

In accordance with the coarsening rate equation, the particle size grew significantly between the 0 hr and 2.5 hr and between the 2.5 and 5 hr anneals, but did not grow significantly between the 5 hr and the 10 hr anneals. The particle spacing, however, continued to increase. Modeling of coarsening by others also predicts this behavior. The particle size and spacing results contribute to the fracture toughness of these films, as will be discussed later in this Chapter.

X-ray Diffraction

Films were deposited onto a-plane and r-plane alumina substrates which made it impossible to distinguish between any peaks from the substrate from those of the film. Because of this depositions of YSZ-alumina were made on amorphous silica substrates. It was observed that the alumina in the film would not produce x-ray diffraction peaks in the APD. Previous work by Hendrick [56] et al. also showed this problem. In this earlier work, it was shown by transmission electron diffraction that the alumina films deposited were nanocrystalline θ-phase alumina for depositions at 800EC and 1000EC, and that at 1200EC, both θ and α-phases were codeposited. Thus, the grain size of the θ-alumina film deposited was so small that the APD could not resolve the peaks. In order to determine the presence and the phase of the alumina in the film produced in the current research, TEM electron diffraction was also performed, as detailed in the next section.

X-ray diffraction of the 100% YSZ films deposited onto the alumina substrates was very useful. The results showed that zirconia was definitely present and was either in the cubic or the tetragonal phase. Because the addition of yttria to zirconia shifts the zirconia peaks only a fraction of the its original d-spacing, the exact phase of the YSZ could not be determined. For example, zirconia with a 6.0 mol% $YO_{1.5}$ addition (which is tetragonal) would result in the [111] reflection shifted 0.16% (2.956 to 2.961Å). Instead, electron diffraction in the TEM was used to find this information. Table 12 [57, 58] shows the effect of yttria content on the lattice parameters of zirconia.

Table 12: Effect of Yttria Content on Zirconia Lattice Parameters

Phase	**Lattice Parameter, Å**	**Relationship of d-spacing to lattice parameters**
Tetragonal[1]	a = 3.5963 + 0.00227 x c = 5.1892 - 0.00256 x	$\frac{1}{d^2} = \frac{h^2 + k^2}{a^2} + \frac{l^2}{c^2}$
Cubic	a = 5.1038 + 0.016628 x	$\frac{1}{d^2} = \frac{h^2 + k^2 + l^2}{a^2}$

x = mol% $YO_{1.5}$

[1]Lattice Parameters given here are for Primitive tetragonal; the PDF card is given with Pseudofluorite indexing. Meaning, for example, the PDF card's hkl of 111 becomes the primitive hkl of 101 using the transformation of hp = (hf + kf)/2, kp = -(hf - kf)/2 and lp = lf. The primitive hkl's and lattice parameters are used in Table 12 to obtain the proper d-spacing.

Residual Stress

Residual stress from CTE mismatch, both between the film and substrate (film stress, σ_F) and between the matrix and second phase particles of the film (matrix stress, q), was determined for each composition of films.

Film Stress: The film stress was a tensile stress for all compositions. This was because the CTE for the YSZ was higher than that of the substrate, alumina. At the deposition temperature both film and substrate were expanded. Upon cooling the film wanted to retract more than the substrate, but because of the large dimension of the substrate compared to the film, the film was restrained by the substrate. Because the film was very adherent to the substrate, the result was the tensile stress in the film. The maximum film stress occurred very close to that of 100% YSZ, as expected, because of the large CTE mismatch between YSZ and the substrate, alumina. The minimum occurred at 100% alumina as expected, because both film and substrate were the same materials. The maximum did not occur at 100% YSZ but somewhat higher at 9 vol% alumina. This was due to the film stress equation containing the elastic modulus for the film. The film elastic modulus was calculated using the rule of mixtures. The high modulus for the alumina (380 Gpa) was much greater than that for YSZ (200 Mpa), which for the 15 mol% alumina film resulted in a film modulus higher than the 100% YSZ film. This made up for the slightly lower CTE mismatch and gave a slightly higher film stress.

Matrix Stress: The matrix stress was in tension for the low alumina compositions and in compression for the high alumina compositions. This was because the CTE for YSZ was higher than the alumina. When the YSZ was the matrix material (low alumina) and the film was formed at high temperature, the two phases were both expanded. Upon cooling the YSZ contracted more than the alumina, resulting in the compression of the alumina particles. Because of the many particles in the matrix (all under compression by the YSZ) and the necessity for the composite to be in equilibrium, the matrix must subsequently be in tension. The reverse was true when the alumina was the matrix material.

The matrix stress was zero at the extremes (100% YSZ and 100% alumina) as expected because there were no second phase particles present. The maximum was 211 MPa at 45 mol% alumina and the minimum was -322 MPa at 55 mol% alumina. Chapter VI will detail more on the matrix stress (and film stress) for application in the fracture toughness model.

Transmission Electron Microscopy

The TEM provided the necessary means for the determination of the presence of alumina in the films as well as the phase of that alumina. These studies were presented in Figures 31, 32 and 33. Recall the films were produced with flame temperatures of 1550EC and substrate temperatures of 1050EC. EDS on the YSZ-alumina films indicated the presence of aluminum as well as the presence of zirconium and yttrium consistent

with the SEM results. The electron diffraction of the YSZ-alumina films produced ring patterns when a large selected area aperture (500 μm) was used. Indexing of these rings confirmed the presence of zirconia and alumina. However, using the ring patterns alone could not distinguish between cubic or tetragonal zirconia nor could it distinguish between alpha or theta alumina.

Utilizing the microdiffraction allowed the isolation of very small areas for diffraction. After confirming a particle in the film contained zirconium using EDS, the electron beam was converged to a small point on the YSZ where a single crystal spot pattern was obtained, see Figure 33. Indexing this pattern showed that the phase of YSZ was indeed the non-transformable, TN, tetragonal phase. The tetragonal phase has the distinctive {1G2}-type reflections when on the [G11] zone axis [59]. Using a similar technique on the alumina part of the film also resulted in a single crystal electron diffraction pattern, but the indexing of those reflections did not exclude alpha or theta. It was concluded that both alpha and theta phases of alumina were present.

High resolution imaging by TEM provided the ability to view the small second phase (YSZ) of a 62.8mol% alumina (non-annealed) film which could not be resolved in the SEM. The micrograph showed that the sizes of the second phase particles were on the order of 25 nm in diameter for that particular film. Other 62.8 mol% alumina films had YSZ particles ranging in size from 40 to 240 nm. For those films the YSZ was large enough to be resolved in the SEM and so TEM imaging was not necessary.

Energy Dispersive Spectroscopy

EDS was performed on the films in the SEM, but the results were not conclusive due to the aluminum present in both the film and the substrate. The Lα peaks of yttrium and zirconium were located at 1.922 and 2.042 keV, respectively, and were not distinguishable from each other. Therefore high accelerating voltages (>25kV) were necessary to excite the separated Kα peaks of yttrium and zirconium, located at 14.957 and 15.774 keV, respectively. Attempts to perform EDS just on the film while in cross-section inherently included aluminum from the substrate because of the large interaction volume of the electrons due to the high accelerating voltages required.

EDS performed in the TEM allowed the quantification of the aluminum in the film without substrate contributions. It also permitted differentiation between the zirconium and yttrium because of the very high voltage (200 kV) exciting the Kα peaks. The TEM specimen prepared from the YSZ standard was used to provide a basis for the amount of yttria in the films. Because the amount of yttria in the films was relatively small, a more accurate measure of the yttria content was possible utilizing the standard. No YSZ-alumina standard was available. The resulting amount of the yttria (5.7 to 7.81 mol%) in the YSZ-alumina films was somewhat higher than the goal of 4.53 mol% (8 wt%) yttria to which the precursor solutions were prepared, indicating possibly a tendency for yttria to deposit more readily than zirconia. However the amount of alumina in each of the films was within 1.1% or less of the solution composition.

Quantitative Image analysis

Zeiss KS-400 computer software was used for the quantitative image analysis to determine average particle sizes, area percentages and nearest neighbor distances from the SEM backscatter electron images and the high resolution TEM images. The particle sizes for the 62.8 and 80 mol% alumina films were actual average diameters of the second phase particles. However for the 15, 30 and 45 mol% films, the particle sizes calculated were an effective size determined using the equivalent circle diameter method [60]. For a each second phase particle (alumina "swirl" for these mol%'s) this method found the area of that swirl, arranged it into a circle and calculated the effective diameter.

The average particle size decreased steadily as the amount of alumina in the film increased. The size increased for the 62.8 mol% alumina anneal series with increasing anneal time. This was expected as anneal time increases as there was sufficient time and driving force for diffusion in the matrix of alumina to cause coalesence into larger particles.

The nearest neighbor distances for the 62.8 mol% anneal series increased significantly as the anneal time increased. This was also attributed to the diffusion of the YSZ in the alumina matrix. At the lower anneal times there were some large particles present but still many small particles, which kept the nearest neighbor distance from becoming large. In the longest anneal of 10 hours at 1500EC there were many large particles and very few small particles in between. The diffusion of the YSZ from the

small particles was thus much more complete at the 10 hour point than after the 2.5 or 5 hour anneals. As discussed previously in this chapter, this was a coarsening behavior resulting in a diffusion-controlled coarsening rate of 0.0013 $\mu m^3/hr$.

The area percentage of YSZ particles determined by the quantitative image assumed to be analysis was approximately equal to their volume percentage. This follows from assuming uniform sizes and shapes of the microstructure in two dimensions and extending them into three dimensions. This gave volume percentages of YSZ particles that were all within 9% of the precursor starting amounts. For the eutectic composition (62.8 mol% alumina) anneal series each of the measured volume percentages were within 6% of the precursor amounts.

Nanoindentation

Bulk Material Specimens

The various bulk material specimens tested with the Nanoindenter® were selected because of their relationship to the film materials (alumina, YSZ) or because of their availability, see Table 13. The testing parameters, which include the indenter tip geometry, load ranges, indent spacing, number of indents per sample, etc., was the same for the bulk materials as for the films. The hardness and elastic modulus of the bulk materials were close to their literature values, which were obtained from large scale testing; for hardness, Vickers, Knoop, Brinell or Rockwell testing equipment were used,

and for elastic modulus, tensile tests, three point bend tests, etc. were used [48, 61, 62, 63]. The hardness and elastic modulus error bars were very tight compared to those of the films, compare Figure 36 with, for example, Figures 48 and 49. This was an indication of the greater homogeneity of the bulk materials versus the films.

Table 13: Bulk Materials Mechanical Properties, Nanoindentation and Literature

Material	**Hardness, GPa**		**Elastic Modulus, GPa**		**Fracture Toughness, MPa·m$^{0.5}$**	
	Nano.	**Lit.**	**Nano.**	**Lit.**	**Nano.**	**Lit.**
Al_2O_3	30.9	25.9[48]	481	433[48]	2.3	2.2[61]
SiO_2	8.7	8.3[48]	72.2	72.4[64]	0.70	0.58[48]
MgO	8.4	7[65]	290	300[62]	1.2	1.77[66]
ZrO_2 (9.5mol% Y_2O_3)	19	13[62]	309	200[62]	1.30	2.8[63]

Additional nanoindentation tests on different specimens of bulk materials performed at different times showed that the hardness and elastic modulus did not vary significantly, which was as expected. This showed that the nanoindentation equipment was stable. The a-plane alumina was tested on six different samples, three at random orientations and three at 0E, 30E and 90E rotations, see Figure 36c-f. The elastic moduli for the six orientations were not statistically different, but hardness for the 0E test was

significantly higher than the 30E and 90E orientations. The hardness value for the second a-plane alumina sample was closer to values for the 30E and 90E orientations while the hardeness for the first and third a-plane alumina samples were closer to the value for the 0E orientation. This leads to the conclusion that the second a-plane alumina sample was oriented closer to 30E or 90E while the first and third a-plane alumina samples were oriented near 0E.

Two amorphous silica samples were tested, see Figure 36c and d. Both the hardness and the elastic modulus were statistically identical. Because of the tight error bars and the closeness of the results from additional tests, it is concluded that the nanoindentation procedure and testing for hardness and modulus were repeatable and reliable.

The nanoindentation fracture toughnesses of the bulk materials were also similar to the literature values of fracture toughness obtained by larger scale testing. However, the r-plane alumina had a significantly higher measured toughness than the measured and literature values of the a-plane and polycrystalline aluminas. The error bars for fracture toughness were on the order of ± 0.5 $MPa \cdot m^{0.5}$ which was similar to fracture toughnesses reported in the literature [48, 67, 68].

YSZ-Alumina Films

Data from Indents: Large error bars in hardness and modulus for the films were an indication of inhomogeneities such as porosity or possibly surface roughness. When

the indenter encountered a pore just beneath the surface of the film, the indenter tip would be loaded briefly until the material above the pore gave way. This resulted in a displacement of the tip with no change in load, as shown in Figure 40.

Surface roughness of the film can cause the indenter tip to slip due to the contact angle being other than normal to the plane of the substrate, see Figure 41. The load was increased and once it reached a certain point the tip slipped, causing an abrupt displacement with no change in load. Depending on the geometry of the surface, slippage could occur several times during the indentation, as shown in Figure 41.

The 'bad' load-displacement curves result in values of hardness and elastic modulus for the films that were several orders of magnitude lower than expected. For example, hardnesses of 0.01 to 0.08 GPa were observed for 'bad" indents compared to 1 to 35 GPa for 'good' indents. 'Bad' indents such as this were not included in the final data presented in this thesis. Additionally, comparing the error bars for the bulk material nanoindentation tests to the error bars of the films studied, it was observed that the bulk materials' error bars were very tight relative to the films'. The combustion CVD technique used to grow the films inherently leaves small amounts of porosity and small variations in roughness. Because of this, even with the omission of the 'bad' indents, there is significant variability for the hardness and elastic modulus for the films (as compared with bulk standard materials).

Elastic Modulus/Hardness Ratio: The determination of the fracture toughness using equation (22) includes the ratio of elastic modulus to hardness of the film. It was found that this ratio was in the range of 20 to 25 for all of the YSZ-alumina films regardless of composition, deposition parameters or film morphology. Noting this fact can allow the replacement of the *E/H* term in equation (22) with a constant as shown here for a cube-corner indenter tip.

$$K_C = 0.1518\frac{P}{c^{3/2}} \tag{36}$$

Eliminating this term removes uncertainty in the results that originate from the large error bars of the elastic modulus and hardness values determined from the indents. It also helps nullify any influence the removal of 'bad' indents has on the calculated fracture toughness.

Solution Concentration: As reflected in the direct comparison of the 0.002 M and 0.005 M solution concentration films, the hardnesses and elastic moduli were substantially lower for the 0.005 M set of films, see Figure 43. The number of 'bad' indents (i.e. discontinuous load-displacement curves) was significantly higher for the 0.005 M set; out of 15 indents per sample over 50% of those indents were thrown out. Less than 15% of the indents were thrown out for the 0.002 M set of films. The lower the concentration of the precursor solution, the smoother appearing and denser appearing the YSZ-alumina combustion CVD film. It was concluded that nanoindentation for hardness

and elastic modulus determination for combustion CVD films was less reliable for rougher coatings (roughnesses on the order of the indenter tip size) and higher concentration precursor solutions. And the more homogeneous, smooth and dense-appearing the film, see Figure 42, the better the hardness and elastic modulus data obtained from the Nanoindenter®.

Fracture Toughness Crack Analysis: The fracture toughness values calculated from the cracks formed during nanoindentation also had significant error bars. These error bars were obtained directly from the differing crack lengths measured from each indent. There were cases where the indent created cracks in the film but the recorded crack length was not included in the results; these were designated 'bad' cracks because these types crack were not allowed under Lawn et al.'s [47] model for fracture toughness.

Two types of 'bad' cracks existed for all of the films tested. The first type was lateral cracking in the film, as seen, for example, in Figure 54. This particular sample was a 100% YSZ film grown for 30 minutes at 1550EC. Lateral cracking usually occurred when the indent depth was very large compared to the film thickness and caused delamination of the film from the substrate. For the lateral cracks are shown in Figure 54, the film thickness was ~ 0.7 μm and the indent depth was ~1.8 μm. Li et al. [69] observed the same phenomenon with when performing nanoindentation of 400 nm films of amorphous carbon on silicon substrates and theorized the lateral cracking was related to discontinuities in the load-displacement curves.

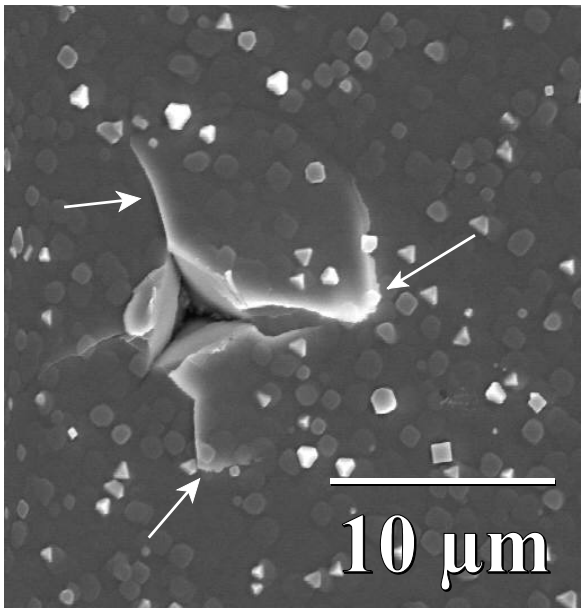

Figure 54 SEM micrograph showing lateral cracking and delaminating of the film.

The second type of 'bad' crack was short cracks that did not extends past the plastic deformation zone created by the indenter. Lawn et al. [47] showed that the plastic zone extends a certain distance around an indent and in order to provide a true measure of the films properties, the crack must propagate past this zone. As explained in Chapter II the procedure used was to include cracks lengths, c, greater than twice the indent size ($c > 2\ r_0$), where r_0 was the indent size (distance from the center of the indent to a point of the indent). Figure 55 shows an example of a short crack in a film that did not extend past the plastic zone. This particular film was a 45 mol% alumina film grown for 30 minutes at 1550EC.

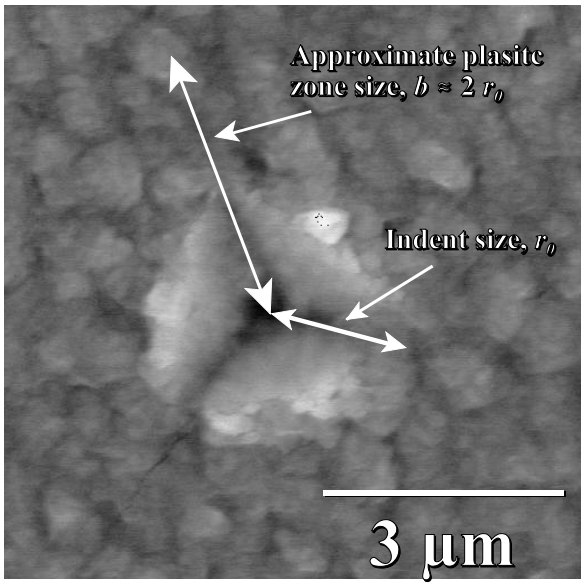

Figure 55 SEM micrograph showing short crack that does not extend past the plastic zone.

The direct comparison of the 0.002M and 0.005M solution concentration films' fracture toughnesses obtained from nanoindentation showed that the 0.005M set was tougher throughout the compositional range. This was attributed to the voids in the film which can slow or arrest the propagation of a crack. Recall that approximately 50% of the nanoindentation measurements were not used due to 'bad' indents such as those produced by encountering pores beneath the surface. Thus the observations of the films' morphology were consistent with the fracture toughness results.

It was also noted that the error bars for the poor quality films (the 0.005M set) were on the order of ± 1.5 to 2.0 $MPa \cdot m^{0.5}$ while the deviation for the better quality films

(the 0.002M set) was ± 0.5 MPa·$m^{0.5}$. Because the error in the fracture toughness of the higher quality films was similar to that of the bulk materials, it was concluded that the fracture toughness from the nanoindentations was an acceptable measure of the film's properties.

Repeatability Study: The films examined for the repeatability study were a set of 100% YSZ and 30 mol% alumina films deposited for 30 minutes at 1550EC. Each deposition was set up and performed with the same conditions. However, there were slight differences in the depositions due to the nature of the combustion CVD procedure as described in the Deposition Parameters section earlier in this section. The nozzle tips were not always the same; hence the aerosol size was not necessarily the same. The position of the substrate in the flame was not always exactly the same; therefore the temperatures of the depositions were not identical.

The hardness and elastic modulus that were measured were found to be statistically the same (using the t-test) for each of the five different depositions at each composition. The error bars for a particular specimen were based on the different values obtained from each of the fifteen indents that specimen.

The fracture toughness values for each set of five films were somewhat different, as shown in Figures 44 and 45. The error bars for all ten films in the repeatability study were on the order of ± 0.5 MPa·$m^{0.5}$. The magnitude of these error bars were similar to the error bars for the bulk materials' fracture toughness. It should be noted that the

average fracture toughnesses of each set of five films (100% YSZ set and 30 mol% alumina set) agrees with the average toughness of the final 100% YSZ films and 30 mol% alumina films, Table 14. This is encouraging since the ten reliability study films were deposited under different conditions than those of the final set of films (solution flowrate was 3 ml/min to 4 ml/min, oxygen flowrate was 18 liters/min to 20 liters/min, nozzle tips were different). It was concluded from the reasonable magnitude of the error bars and the fracture toughness agreement that the fracture toughness values of the repeatability study were reliable.

Table 14: Comparison of 100% YSZ and 30 mol% Alumina Fracture Toughness

mol% Al_2O_3	**Average Kc, MPa·m$^{0.5}$**	
	Repeatability Study	**Compositional Study**
0	1.75 ± 0.41	1.76 ± 0.46
30	2.73 ± 0.46	2.49 ± 0.32

Anneal Series: The fracture toughness of the eutectic composition (62.8 mol% alumina) anneal series resulted in an interesting trend: the toughness increased as the particle size grew, then dropped abrubtly, see Figure 46. Plotting the same fracture toughness versus the first nearest neighbor distance showed a similar drop in toughness but not as severe, Figure 56. This leads to the conclusion that not only was the particle size important in the fracture toughness, but that the distribution of the particles in the

matrix was also important. The succeeding section on fracture toughness modeling discusses this issue in more detail.

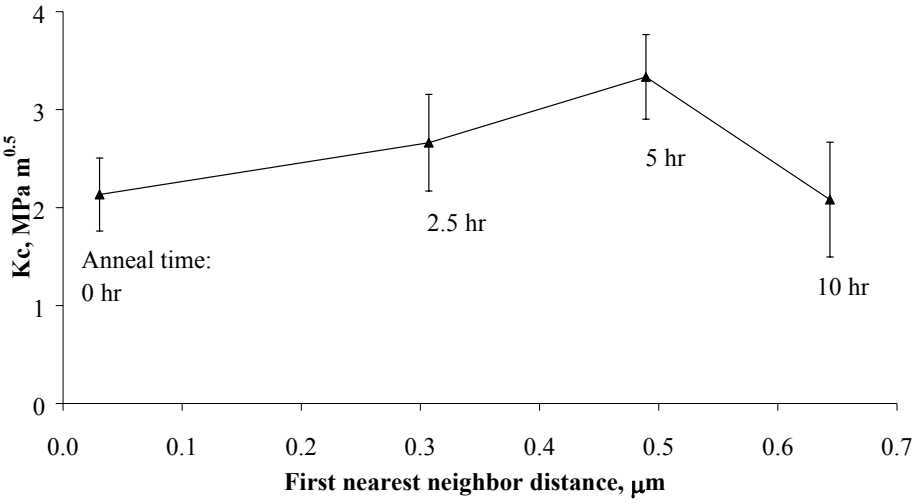

Figure 56 Fracture toughness versus the nearest neighbor distance for the 1500EC annealed series of 62.8 mol% Al_2O_3 films .

Hardness and Elastic Modulus, Compositional Study vs Indentation Depth: The hardness values for the range of compositions studied were relatively constant as the indentation depth increased. Hardnesses of several compositions (15, 30, 45 and 62.8 mol% alumina) increased slightly while those of three (100% YSZ, 80 mol% alumina and 100 mol% alumina) decreased. A significant increase in hardness with indentation depth is usually an indication of substrate effects influencing the measurement [36]; this occurs when the substrate (alumina) is harder than the film and plastic zone under the indenter reaches the

film-substrate interface. However, the change in the hardness for these films was not significant as determined by the t-test.

The elastic modulus for every composition increased as the indentation depth increased which is also an indication of substrate effects influencing the measurement. The elastic modulus at the largest indentation depth approached that of the substrate. With the thickness of the films between 0.7 and 1.0 μm, the two shallowest indentation depths of ~40 nm and ~75 nm were well within the rule-of-thumb being five to ten times less than the film thickness to allow no substrate influence. The depth of the largest indentation was approximately 175 nm (or 0.175 μm) which encroached on the rule-of-thumb value (film thickness for a 175 nm indentation should be 875 to 1750 nm thick). Therefore the elastic modulus for the deepest indentation depth was considered to be influenced (at least somewhat) by the substrate.

Hardness and Elastic Modulus, Compositional Study vs Alumina Content: The hardness of the films decreased as the amount of alumina increased (minimum at 30 mol%) then increased to maximum at 100% alumina, while the elastic modulus did not change significantly with the alumina content. Because hardness is similar to a stress, i.e. hardness is a load divided by an area as is stress, it was theorized [70] that the hardness followed the theoretical residual stress in the film. For example, at 100% YSZ, because the CTE for YSZ is greater than the substrate (alumina), the film is in tension and when the external stress (indenter tip) is applied, the resulting hardness is lower than the

hardness determined for an unstressed film. At the 100% alumina composition the CTE mismatch was the least (zero) which results in no thermal film stress contribution to the hardness and therefore a maximum hardness. The indentation was a compressive stress on the film and added to that was the tensile film stress resulting in a minimum hardness at 100% YSZ.

However, this was an over-simplification of the indentation mechanics. As detailed by Suresh et al. [71] the stresses involved must be resolved into forces by multiplying by the appropriate contact areas. For a tensile stress in the film, the force due to the indenter tip acts in the same direction as the differential force resulting from the tensile stress, effectively decreasing the load required to create the same size indent. This results in a lower hardness for materials with tensile residual stress. This coincides with that observed with the YSZ-alumina films.

This may not be the complete explanation because of the relative magnitude of the stresses (and forces) involved. The maximum theoretical thermal film stress calculated for the 100% YSZ film on alumina was 300 MPa tensile. Multiplying by a nominal area for an indent (0.9 μm^2) gives a force of 0.27 mN. The applied load to create for such an indent is on the order of 10-25 mN depending on the material. Based on these numbers the order of magnitude of the thermal stress alone would not be sufficient to affect the hardness. Additional stresses may be present in the films which could contribute to the measured hardness, such as the matrix stress caused by the mismatch of CTE's between

particles and the matrix. The order of magnitude for the matrix stress was similar to the thermal stress calculated from the film-substrate CTE mismatch, 0 to 239 MPa compressive. Summing the two forces from these stresses (thermal and matrix) yields a force of 0.49 mN. Based on these results, the residual stresses present in the film were still too small to cause a significant shift in the hardness. The actual film stresses may be different but at the present time their measurement has not been possible.

Additional insight into the residual stress effect on hardness is provided by Pharr et al. [72]. In their nanoindentation of aluminum they concluded that the hardness (and elastic modulus) were not functions of the stress in the material; the observation of a decrease in hardness with the presence of tensile stresses and an increase in hardness with compressive stress was a result of the method for determining the area of the indent used in the calculations. Nanoindentation uses the calculated area based on the geometry of the indenter tip. For a ductile material, like aluminum, there is substantial pile-up of material around the indenter tip while the load is applied; this makes the actual indent area during contact larger than that assumed by the calculated area. Pharr et al. applied various stress states to aluminum and compared hardnesses determined from the calculated area and from the actual area measured by examining the indents to arrive at their conclusion: hardnesses and modulii computed from actual contact area measurements are essentially independent of stress. They also found that compressive stresses had a much more significant effect on the pile-up (and hardness) than tensile

stresses. For the ceramic materials in this research, there was not significant pile-up around the indenter tips, leading to the conclusion that the calculated contact area used for the hardness and elastic modulus did not underestimate the actual contact area. Therefore it was inconclusive what the exact contribution the thermal or intrinsic film stress has on the hardness.

Fracture Toughness: The compositional study showed the fracture toughness initially increased with alumina content, reached a plateau and then decreases somewhat near the highest alumina percentages. Each composition in these results was an average of fracture toughnesses from two films, each with at least twenty indents and each indent with one to three cracks. The error bars for each of the compositions was a function of the various crack lengths measured. As with the previous films' fracture toughnesses, the error bars were close to that recorded for the bulk materials' fracture toughnesses, all were within ± 0.5 $MPa \cdot m^{0.5}$. The t-test on the fracture toughness for the compositional study showed that the low and high alumina films were statistically different, while the mid-range of compositions were statistically the same, as detailed in Table 11 of Chapter IV.

The matrix of indents for the cube-corner tip included five different loads ranging from 400 mN to 25 mN. As noted in Chapter III, the highest loads were used for locating the indents in the electron microscope so that measurement of the cracks could be performed. The cracks for the 400 mN indents were not included in the fracture

toughness results presented in the previous discussion because the size of those indents produced delamination of the film and penetrated completely through the film into the substrate. Depending on the film composition and the film thickness, the indenter depths for the 250 mN and 100 mN loads were close to the film thickness. The indents for the 50 mN and lower loads were always less than the film thickness. It is interesting to note that even though some of the 250 mN and 100 mN loads had indent depths on the order of the film thickness, the fracture toughnesses for the 250, 100, 50 and 25 mN loads do not differ significantly, see Figure 57. However, the fracture toughnesses determined from the 400 mN loads tend to be lower, possibly due to delamination of the film from the substrate. It was concluded that fracture toughness of the films was not a function of the applied load as long as the film and substrate was not penetrated to the extent that significant delamination occured.

CHAPTER VI

FRACTURE TOUGHNESS MODELING

For fracture toughness, several factors must be taken into account when analyzing the cracking of a material under a load, particularly a thin film. As discussed by Evans et al. [67, 73], Clarke and Faber [74], and Becher [75], several toughening mechanisms exist: crack deflection, grain bridging, residual stress, phase transformation toughening and micro-cracking. Depending on the material in question, some or all of these mechanisms may occur. For the system studied here, the first three (crack deflection,

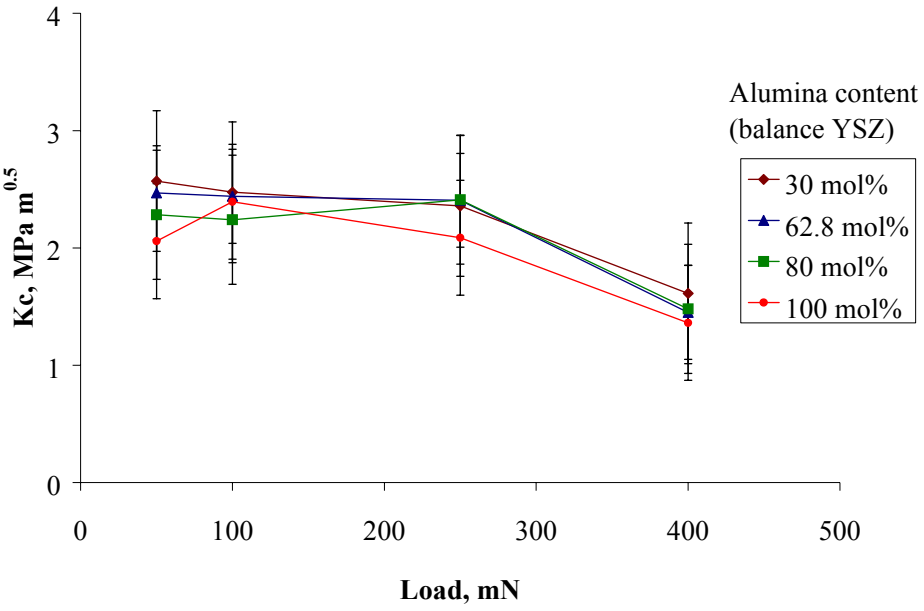

Figure 57 Fracture toughness versus indent load for several YSZ-Al_2O_3 films.

grain bridging and residual stress) were considered significant contributors to the toughening of the films. The last two mechanisms (phase transformation toughening and micro-cracking) were found to not contribute to the toughening of the films, as discussed below.

Many researchers have added particles of a second phase to materials for toughening; a few will be discussed here. In 1977, Claussen et al. [68] examined bulk materials of alumina dispersed with zirconia particles and found the fracture toughness to increase (on the order of 2 to 4 $MPa \cdot m^{0.5}$) with increasing volume percent of the second phase and increasing size of the particles. However, they attributed all of the toughening to microcracking and did not consider crack deflection. Also in 1977, Khaund et al. [76], developed a model for toughening based solely on the CTE difference between the matrix and particles and applied it to a system consisting of an alumina sphere in a glass. It was not until 1983, when crack deflection was used by Faber and Evans [77] to describe the toughening mechanism occurring as a result of a second phase addition to the matrix. Faber and Evans applied their model to describe the toughening of lithium-alumino-silicate glass containing $Li_2Si_2O_5$ crystal particles [78], SiC with Al_2O_3 particles and SiC with ZrO_2 particles [79]. Faber et al. [80] also examined MgO and found toughness increases with LiF additions from crack deflection. Additionally, Wei and Becher [81] studied SiC with TiC particles and found ~ 2 $MPa \cdot m^{0.5}$ increase in toughness all attributed to crack deflection.

Other researchers have achieved toughening on various ceramic composite systems. DePortu et al. [82] found an increase in toughness with the addition of YSZ to alumina and attributed it to transformation toughening and possible grain bridging but provided no model. Taya et al. [54] found toughness increased due to crack deflection and residual stress in a SiC matrix with TiB_2 additions, and developed an expression for the toughening due to residual stress in the matrix. This is to be used later in this chapter. Lawn et al. developed a model for microcracking [83] and for grain bridging [84], then applied both to Al_2O_3 with particles of Al_2TiO_5. Their grain bridging model is discussed later in this chapter. Li and Watanabe [3] detailed the increase of fracture toughness in YSZ with Al_2O_3 additions up to 30 vol%. Their model included the following toughening mechanisms: crack deflection, phase transformation, residual matrix stress and grain bridging. Their model was similar to that developed in this thesis for the toughening of combustion CVD YSZ films by the addition of alumina.

The toughening of ceramics continues to be heavily investigated, particularly by Faber who has continued to do extensive work in this field including the modeling of microcrack toughening [85] as well as studying grain/crack bridging, all in addition to the crack deflection work previously mentioned. Faber et al. has reported fracture toughening with TiB_2 particles in SiC by microcracking and crack deflection [86, 87, 88], Al_2O_3 in borosilicate glass by microcracking and crack deflection [89], SiC fiber in glass

[90] by grain bridging, SiC whiskers in Al_2O_3 by crack bridging [91] and Al_2O_3 in ZrO_2 by transformation toughening [92] to name several of many.

Phase Transformation Toughening

As described in Chapter II, one form of phase transformation toughening occurs when monoclinic YSZ is under stress and spontaneously changes phases to tetragonal. The accompanying volume change (an increase) can produce enough local compressive stresses near a crack tip to slow or stop growth of the crack.

For this research, the content of yttria in the zirconia was approximately 8wt% which meant that the YSZ was assumed to be the stable non-transformable tetragonal phase. This was also verified by electron diffraction in the TEM. Because the particular phase of YSZ in this study was tetragonal, no contribution due to phase transformation toughening was included in the modeling of the fracture toughness for the films.

Microcracking

On bulk materials tested with large scale indentations, it is was found by Claussen et al. [68] that the large cracks (on the order of millimeters long) originating from the points of the indent had smaller cracks branching off into increasingly smaller cracks. The nucleation and extension of these microcracks releases strain energy which slows the crack growth [68].

For the small cracks (on the order of microns long) involved in the nanoindentation of the films in this research, there was no occurrence of branching of the original crack from the indent point into smaller cracks. This includes the measurements from at least fifteen indents per sample for over twenty different YSZ-alumina films. Based on the observed lack of branching, no contribution from micro-cracking toughening was included in the fracture toughness model.

Crack Deflection

The addition of small second phase particles can increase the fracture toughness of a material by the phenomenon of crack deflection. Stated simply, when a crack tip encounters a second phase particle, one of three things will occur: the crack will cease propagating, the crack will continue to grow straight through the particle or the crack will divert around the particle and continue growing. Which occurs depends on the relative amount of the second phase present, the stress state surrounding the second phase and the strain energy driving the crack growth. In this research, upon encountering a particle, the crack continued propagating either through or around the particle. The complete arresting of a crack by a second phase particle only occurred after the crack had grown for a distance (2.2 and 1.6 μm for the two cracks shown in Figure 58a) and lost a significant amount of energy. In some cases the crack actually continued on its original path through

the second phase particle, Figure 58b. However, many cracks were influenced by second phase particles and only deflected somewhat around the particle, Figure 59.

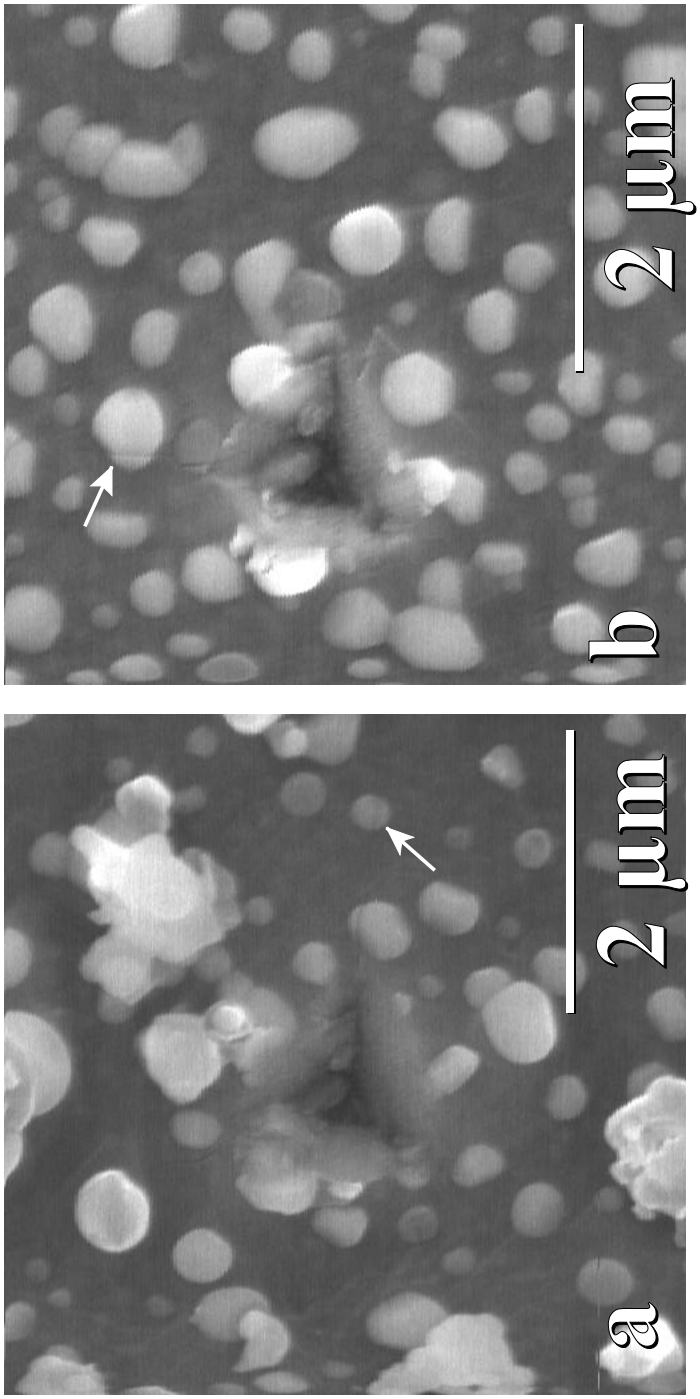

Figure 58 SEM micrograph of a 62.8 mol% Al_2O_3 annealed film showing a) the arresting of a crack at a second phase particle and b) a crack propagating through a second phase particle.

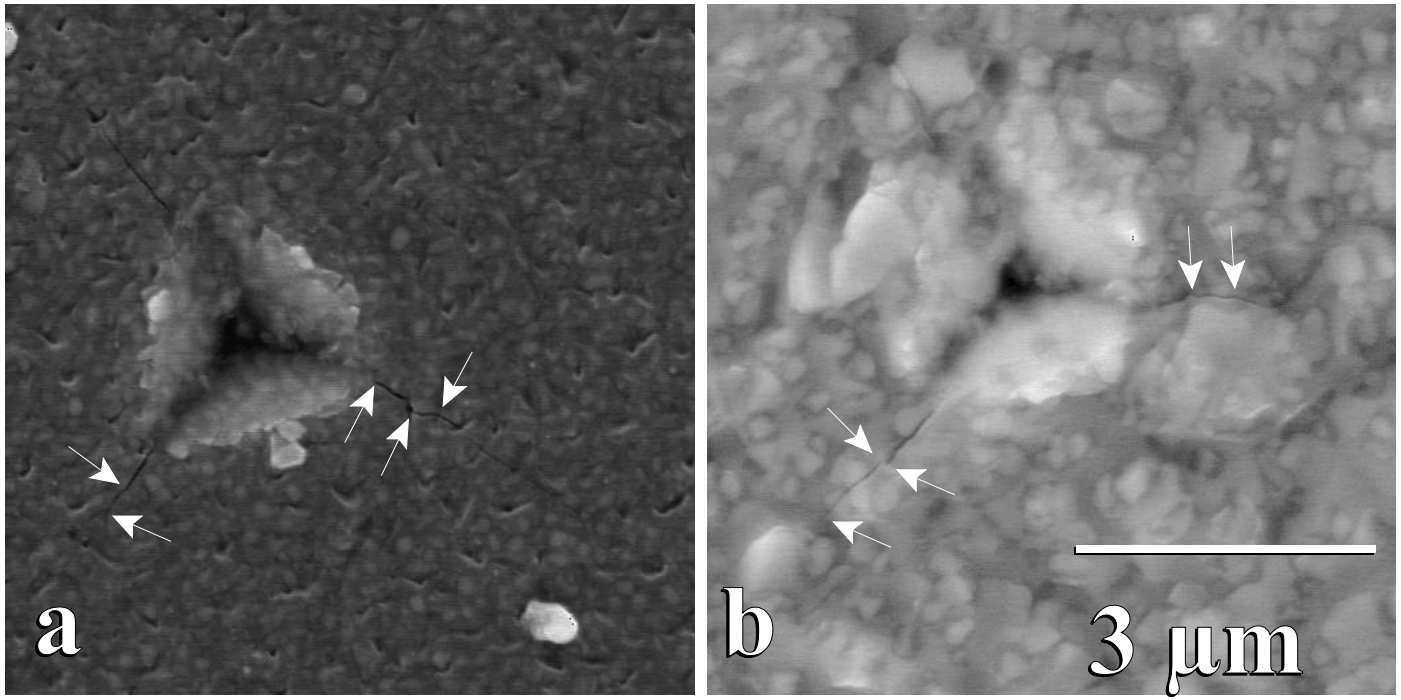

Figure 59 SEM micrograph showing the deflection of cracks about second phase particles; a) 62.8 mol% Al_2O_3 film and b) 30 mol% Al_2O_3 film.

Faber and Evans [77] developed their crack deflection model for four cases: spherical particles uniformly distributed, spherical particles with a spacing distribution (such as Gaussian), rod-shaped particles uniformly distributed and disc-shaped particles uniformly distributed in a matrix. The shape of the second phase particles for many of the films deposited in this research was essentially spherical (particularly for the higher alumina compositions). For this reason and for simplicity, this thesis used the two spherical particle cases for the crack deflection model.

The crack deflection model derived by Faber and Evans was based on the geometric approach of a crack deflected from its main crack plane with no consideration of the stresses induced because of the two different phases. Treatment of the influence of stress is discussed in subsequent sections. The crack deflection model was based on a relative toughness calculated from the strain energy release rates, G (N/m). The following equations describe the model by Faber and Evans.

$$G_c = \frac{G^m}{< G >} G_c^m \tag{37}$$

G_c = toughening due to crack deflection,

G^m = strain energy release rate for undeflected crack,

<G> = net crack driving force)or average strain energy release rate across the crack front,

$G^m{}_c$ = toughness of deflection free material.

The relative toughness $G^m/<G>$ is a function of the volume percent of the second phase material V_f, the twist angle of the crack φ, the tilt angle of the crack, θ and Poisson's ratio of the film, v. The superscripts t and T refer to tilt and twist, respectively. The following equation was derived for spherical second phase particles of uniform spacing,

$$\frac{<G>}{G^m} = \frac{1}{\phi_{\max}} \int_0^{\phi_{\max}} \frac{\sin\phi}{\sin\phi + \cot\phi} \left[\left(\kappa_1^t\right)^2 + \left(\kappa_2^t\right)^2 \right] d\phi + \frac{1}{\phi_{\max}} \int_0^{\phi_{\max}} \frac{\cot\phi\cos\phi}{\sin^2\phi + \cot\phi} \left[\left(\frac{1}{\phi} \int_0^{\phi} \kappa_1^T d\phi \right)^2 + \left(\frac{1}{\phi} \int_0^{\phi} \kappa_3^T d\phi \right)^2 \right] d\phi \quad (38)$$

Where φ_{max} is the maximum tilt angle given by

$$\phi_{\max} = \sin^{-1}\left(\frac{2r}{\lambda}\right) \quad (39)$$

r (m) is the second phase particle radius {d (m) is the diameter} and λ (m) is the average particle spacing. Figures 60 and 61 [77] show the geometry of cracks, σ is the stress in the matrix acting on the crack. The particle spacing can be measured or for a uniform spacing of particles, λ can be determined empirically from

$$\lambda = \frac{1.085d}{V_f^{1/2}} \quad (40)$$

The ratio of particle spacing to particle radius is

$$\frac{\lambda}{r} = \frac{e^{8V_f}}{V_f^{1/3}} \int_{8V_f}^{\infty} x^{1/3} e^{-x} dx \quad (41)$$

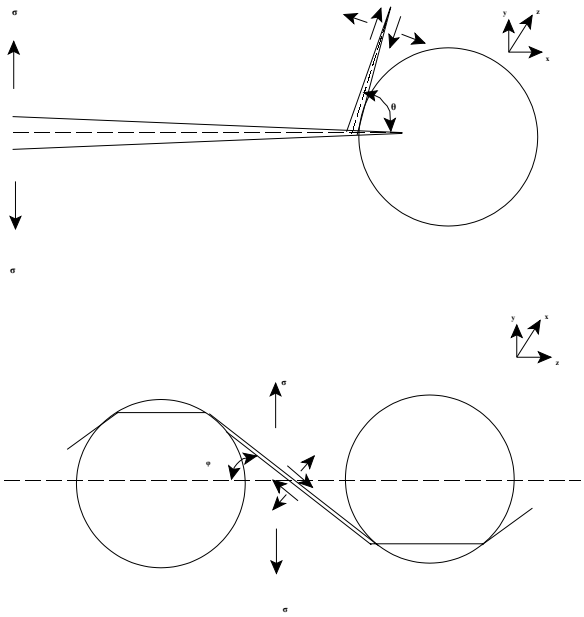

Figure 60 Schematic of typical crack deflection; top: tilt, and bottom: twist of the crack front.

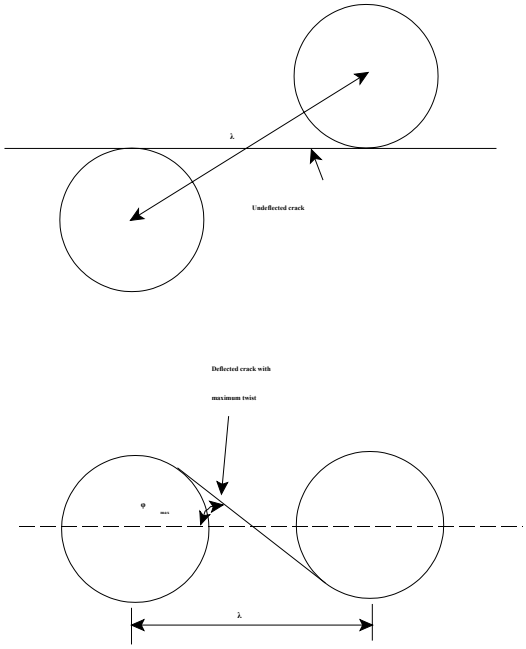

Figure 61 Schematic of two spheres showing top: minium twist and bottom: maximum twist of the crack.

The Mode I stress intensity is K_I (MPa·m$^{0.5}$) and the value of κ (dimensionless) is given by

$$\kappa_i^j = \frac{k_i^j}{K_I} \tag{42}$$

The local stress intensity factors, k_i^t (MPa·m$^{0.5}$), for a tilted crack subject to Mode I applied loading are

$$k_1^t = K_{11}(\theta) K_I \tag{43}$$

$$k_2^t = K_{21}(\theta) K_I \tag{44}$$

K_{11} and K_{21} (dimensionless) are angular functions associated with the tilted crack.

$$K_{11}(\theta) = \cos^3 \frac{\theta}{2} \tag{45}$$

$$K_{21}(\theta) = \sin \frac{\theta}{2} \cos^2 \frac{\theta}{2} \tag{46}$$

The stress intensity factors, k_i^t (MPa·m$^{0.5}$), for the twisted crack are

$$k_1^T = K_{11}(\phi) k_1^t + K_{12}(\phi) k_2^t \tag{47}$$

$$k_3^T = K_{31}(\phi) k_1^t + K_{32}(\phi) k_2^t \tag{48}$$

The associated dimensionless angular functions are

$$K_{11}(\phi) = \cos^4 \frac{\theta}{2}\left[2\nu \sin^2 \phi + \cos^2 \frac{\theta}{2} \cos^2 \phi \right] \tag{49}$$

$$K_{12}(\phi) = \sin^2 \frac{\theta}{2} \cos^2 \frac{\theta}{2}\left[2\nu \sin^2 \phi + 3\cos^2 \frac{\theta}{2} \cos^2 \phi \right] \tag{50}$$

$$K_{31}(\phi) = \cos^4 \frac{\theta}{2}\left[\sin\phi \cos\phi\left(\cos^2 \frac{\theta}{2} - 2\nu \right) \right] \tag{51}$$

$$K_{32}(\phi) = \sin^2 \frac{\theta}{2} \cos^2 \frac{\theta}{2}\left[\sin\phi \cos\phi\left(3\cos^2 \frac{\theta}{2} - 2\nu \right) \right] \tag{52}$$

The following equation was derived by Faber and Evans for spherical second phase particles with variable interparticle spacing incorporating a standard normal distribution:

$$\frac{< G >}{G^m} = \frac{1}{\sqrt{2\pi}}\left\{ \int_{-z_0}^{3} e^{-z^2/2}\left[G^T(z) + G^t(z) \right] dz + \left[G^T(z_0) + G^t(z_0) \right] \int_{-3}^{-z_0} e^{-z^2/2} dz \right\} \tag{53}$$

where

$$G^T = \frac{1}{\phi_{\max}} \int_0^{\phi_{\max}} \frac{\sin\phi}{\sin\phi + \cot\phi}\left[\left(\kappa_1^t\right)^2 + \left(\kappa_2^t\right)^2 \right] d\phi, \tag{54}$$

$$G^t = \frac{1}{\phi_{\max}} \int_0^{\phi_{\max}} \frac{\cot\phi}{\sin^2\phi + \cot\phi} \left[\left(\frac{1}{\phi} \int_0^{\phi} \kappa_1^T d\phi \right)^2 + \left(\frac{1}{\phi} \int_0^{\phi} \kappa_3^T d\phi \right)^2 \right] d\phi \tag{55}$$

and

$$z = \frac{x - \frac{\lambda}{r}}{S}, \qquad z_0 = \frac{2 - \frac{\lambda}{r}}{S}. \tag{56}$$

with S being the standard deviation of the particle spacing.

The strain energy release rates, G, are related to the stress intensity factor, K (MPa·m$^{0.5}$), by [93]

$$K^2 = EG\,. \tag{57}$$

This equation is for elastic materials under plane stress conditions where E is the elastic modulus. The incremental toughening due crack deflection by Faber-Evans, ΔK_{FE} (MPa·m$^{0.5}$), is the difference in fracture toughness of the material with the second phase particles, K, from equation (57) to the fracture toughness of the matrix material with no second phase present, K_m.

$$\Delta K_{FE} = K - K_m \tag{58}$$

It is interesting to note that the crack deflection model is not a function of the particle size. The ratio of interparticle spacing to the particle size (λ/r) was used in both equation (39) for φ_{max} and equation (41) for λ/r, which results in the crack deflection being a function of volume percent. Figure 62 shows the relative toughness, $G^m/\langle G\rangle$, versus the volume percent of the second phase for the uniform particle spacing and distributed particle spacing obtained from the above equations. The only material property involved in the crack deflection model was Poisson's ratio; those values used are shown in the Results chapter. The solution of the numerous integrals was performed a combination of symbolic integration using MathCad® where possible and numeric integration.

Converting the relative toughness, $G^m/\langle G\rangle$, into the incremental toughening, ΔK_{FE}, via equations (57) and (58), produces Figure 63. The discontinuity in these curves comes from the K_m value in equation (58). For the low alumina compositions (0 to 50 vol% Al_2O_3), YSZ was the matrix and therefore K_m = 1.76 MPa·m$^{0.5}$, the fracture toughness for 100% YSZ. Similarly for the high alumina compositions (50 to 100 vol% Al_2O_3), alumina was the matrix and therefore K_m = 2.20 MPa·m$^{0.5}$, the fracture toughness for 100% alumina. Thus the starting point for each end of the incremental toughening curve was different, producing the jump in the curves at 50 volume percent. Note: Because of the complexity of this model, the incremental toughening due to crack deflection was solved for discrete values of second phase volume percent (0, 5, 10, 15,

30, 45, 55, 62.8, 80, 90 and 100 vol% Al_2O_3), hence the slope at 50 vol% versus the expected vertical jump.

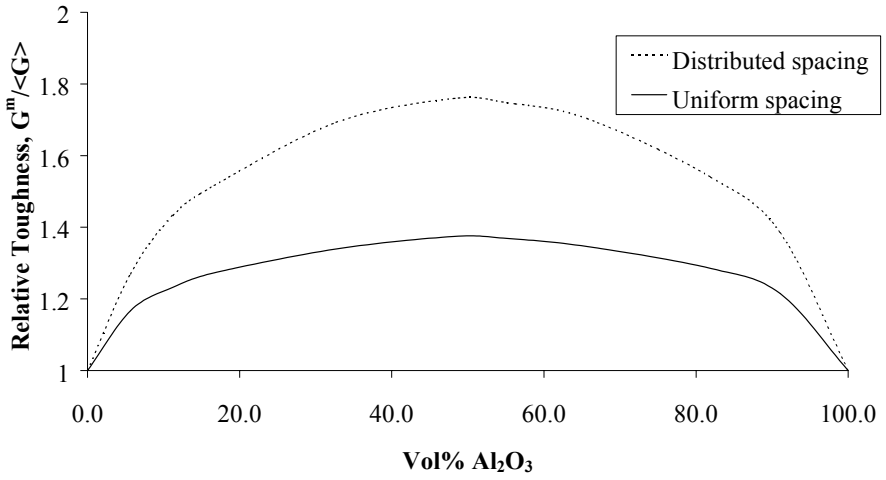

Figure 62 Crack deflection model showing relative toughness versus volume percent Al_2O_3 for both a uniform and distributed spacing.

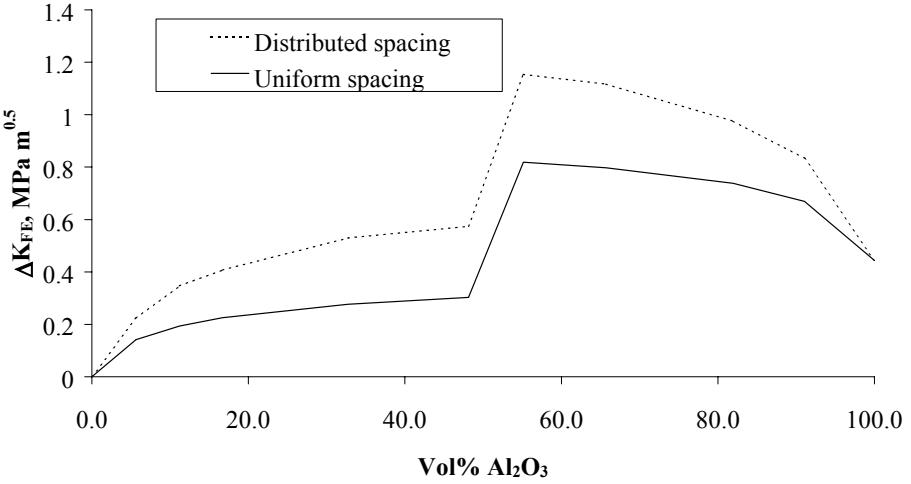

Figure 63 Incremental toughening versus volume percent Al_2O_3 for both a uniform and distributed spacing.

Residual Stress

The crack deflection model by Faber and Evans did not consider the local stresses at and near the interface between the particle and the matrix. The stresses that exist in the film are residual stresses due to thermal expansion mismatch between the two different phases, thermal mismatch between the substrate and the film and intrinsic stresses inherently created during the formation of the film. There is no direct way to quantify the exact amount of the intrinsic stresses in the film; however experiments involving the measurement of the total stress in the film via x-ray diffraction were investigated. The thermal stresses from the difference in coefficient of thermal expansion between the two phases present in the film, will be referred to as matrix stress, and the difference in coefficient of thermal expansion between the film and the substrate, will be referred to as film stress.

The effect of residual stress on the fracture toughness of a material can either promote or slow crack growth depending if the local stress around the crack is tensile or compressive. A crack propagating through a compressive zone will be slowed by that stress because of the closure action of the forces involved. In a tensile zone the crack growth will be encouraged because of the opening action imparted on the crack. Therefore, up to a point, compressive stresses will increase the film's fracture toughness while tensile stresses will decrease its fracture toughness.

Cutler and Vikar developed a model for the residual stress effects on the fracture toughness. However, their model was applicable to only a double cantilever beam test specimen. A more general model for a two-phase material was developed by Taya et al. [54]. Their expression for the incremental change in the fracture toughness was based on the coefficient of thermal expansion differences between the two phases. A brief description of their derivation is shown here. Their expression started with the fracture toughness of a particulate composite, K_{IC} (MPa·m$^{0.5}$), due to a periodic stress field from Evans et al. [67],

$$K_{IC} = K_{I0} + 2q\sqrt{\frac{2\lambda}{\pi}} \tag{59}$$

where K_{I0} (MPa·m$^{0.5}$) is the critical stress intensity factor of the matrix, λ is the length of the stress zone between particles (average particle spacing) and q is the matrix stress (MPa) in the film due to the misfit strain caused by the different coefficients of thermal expansion for the two phases present, as defined in Chapter IV. This was applicable to the two-phase film because of the periodic nature of the compressive and tensile zones in the film due to the CTE mismatch between the particles and the matrix. For example, if the CTE of the particle is greater than the CTE of the matrix at room temperature, there will be a local region of tensile stress in the particle and in its immediate vicinity and compressive stress in the remainder of the matrix, assuming the film was formed at a higher temperature.

The Eshelby model [94] for the determination of elastic fields with ellipsoidal inclusions modified for a finite volume of particles was included in Taya's derivation (refer to Taya et al. [54] for the complete derivation), resulting in the following expression for ΔK_σ (MPa·m$^{0.5}$):

$$\Delta K_\sigma = 2q\sqrt{\frac{2(\lambda - d)}{\pi}} \tag{60}$$

where d is the average particle size of the second phase material. This was the expression used by Li et al. [3] in their modeling of fracture toughness increase due to residual matrix stress.

Because of the additional thermal stress in the film from the CTE mismatch between the substrate and the film, an additional term was added to equation (60) resulting in a revised ΔK_σ (MPa·m$^{0.5}$):

$$\Delta K_\sigma = 2\left(q + \sigma_F\right)\sqrt{\frac{2(\lambda - d)}{\pi}} \tag{61}$$

The film stress, σ_F (MPa), is the same as defined previously in Chapter IV:

$$\sigma_F = \frac{\left(\alpha_s - \alpha_f\right)\Delta T\, E_f}{\left(1 - \nu_f\right)} \tag{23}$$

Compositional Study

Uniform Particle Size and Spacing: Figure 64 shows the results of this matrix stress model for YSZ-alumina composites using a uniform particle spacing as defined in Chapter IV. For this figure the incremental toughness of the film is negative for low alumina compositions and positive for high alumina compositions, resulting in a discontinuity at 50%. This was a direct result of the sign of the matrix stress, q, which was tensile at low alumina and compressive for high alumina (tensile stresses tend to open cracks thus decreasing the fracture toughness while compressive stresses close

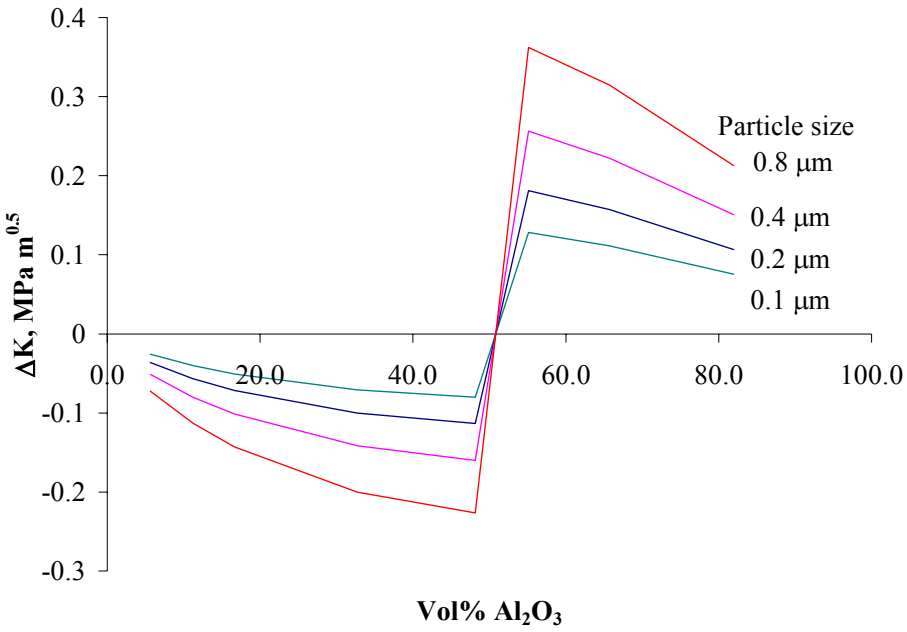

Figure 64 Model of matrix stress incremental fracture toughness versus volume percent Al_2O_3 (balance YSZ) for a range of particle sizes.

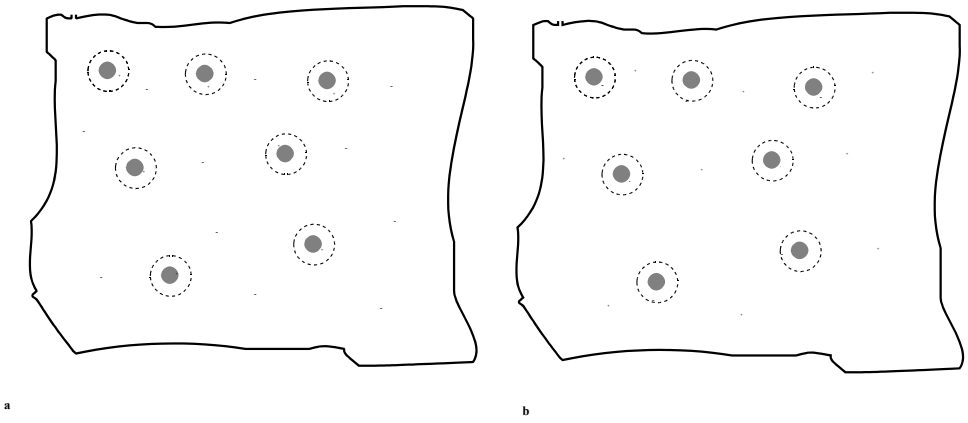

Figure 65 Schematic of stress regions in the matrix and the second phase particles and their immediate vicinity: a) high Al_2O_3 content and b) low Al_2O_3 content [54].

cracks and thus increasing the fracture toughness, see Figure 65. This large discontinuity is unreasonable for the actual film; it implies that toughening from residual stresses does not fully explain the toughening involved with second phase particle additions. Additionally, the actual films' particle sizes vary as the amount of alumina increases; this is shown in the following sections. For Figure 64, the largest particle size has the greatest influence on the toughening while the smallest size has the least, as expected.

Figure 66 shows the toughening increment for only the film stress versus the alumina content for several particle sizes. Because this stress was tensile for all compositions, the toughening increment was negative, decreasing the toughness. The greatest decrease in toughness was at the 100% YSZ composition because that film had the largest tensile stress due to the largest CTE mismatch between the film and the

substrate. The largest particle size had the greatest effect on the toughening while the smallest particle size had the least.

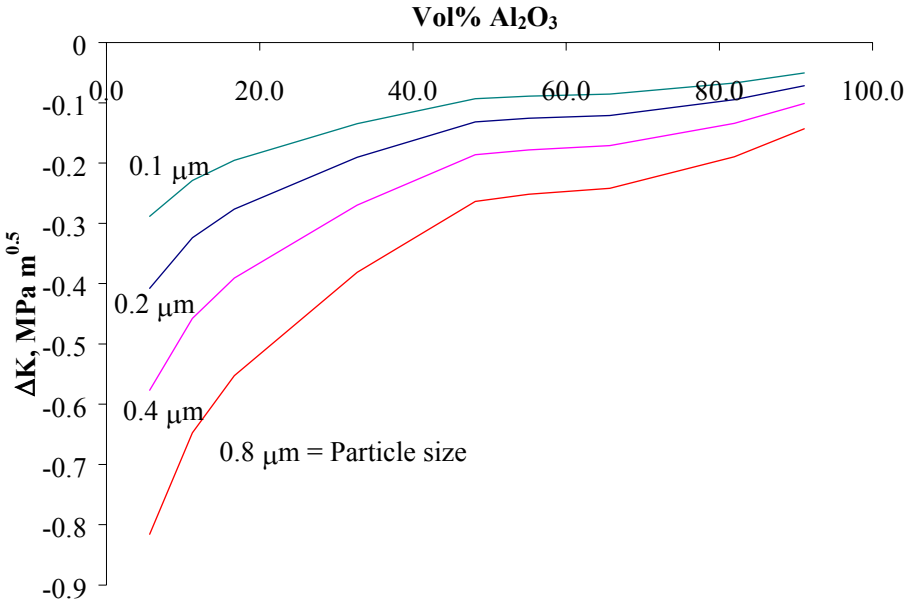

Figure 66 Model of film stress incremental fracture toughness versus volume percent Al_2O_3 (balance YSZ) for a range of particle sizes.

The overall contribution of the thermal stresses combined is shown in Figure 67. This model resulted in large negative toughening increments for the low alumina compositions and small (relatively) positive toughening increments for the high alumina composition films. Again the largest particle size had the greatest effect on the model while the smallest particle size had the least effect.

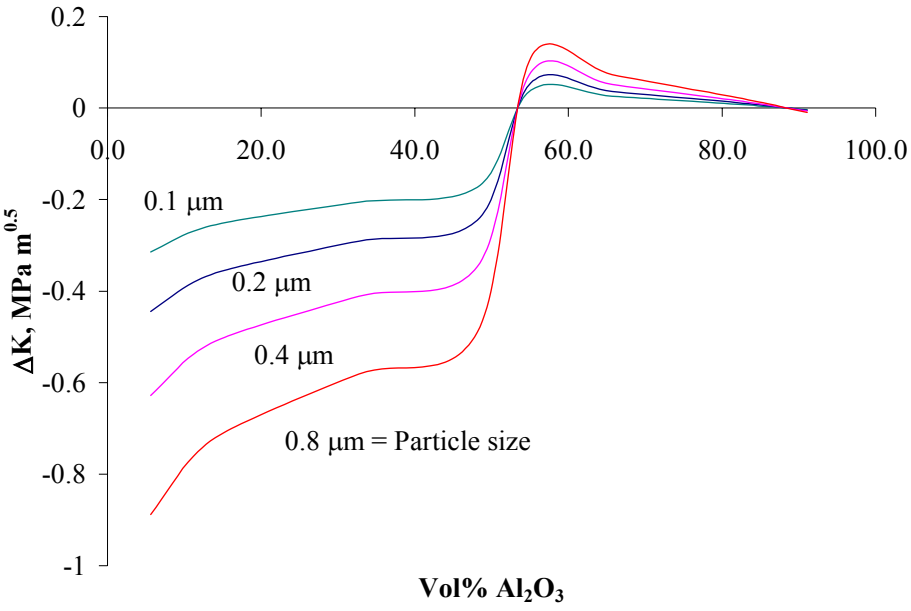

Figure 67 Total incremental fracture toughness of matrix stress and film stress versus volume percent Al_2O_3 (balance YSZ) for a range of particle sizes.

Measured Particle Size and Spacing: The previous figures show the general trend for the toughening due to stress in a film based on uniform particle sizes and spacings for each composition. The actual particle sizes and nearest neighbor distances were not uniform or constant for all compositions fabricated and tested in this work. Figure 68 shows the total model of stress effects on the fracture toughness using the measured particle sizes and nearest neighbor distances. Similar to the uniform particle size and spacing figures shown above, the matrix stress starts negative due to tensile stress and goes to positive values at high alumina content where the stresses were compressive. The

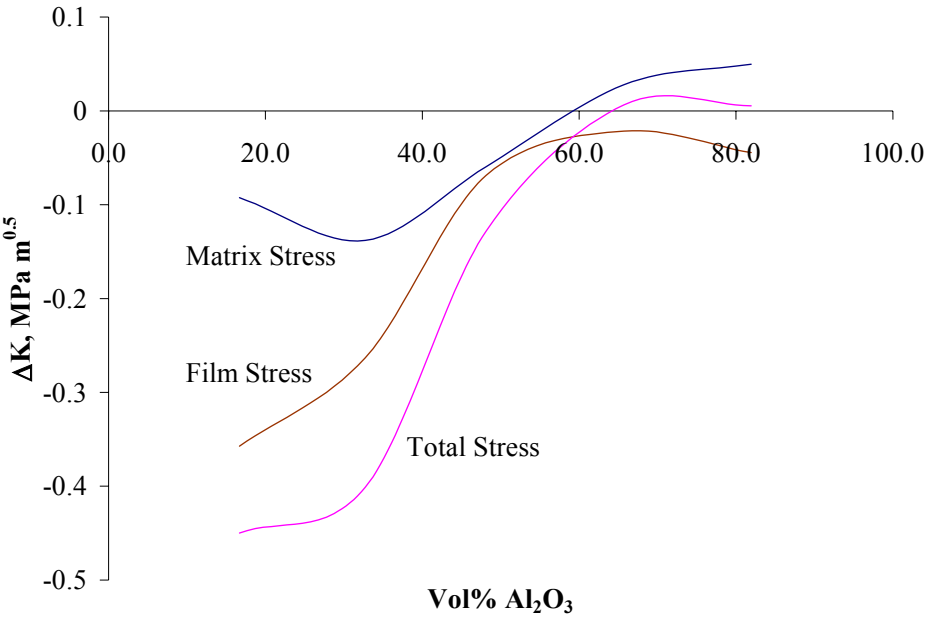

Figure 68 Model of incremental fracture toughness of matrix stress, film stress and their sum versus volume percent Al_2O_3 (balance YSZ) for measured particle sizes and spacings.

film stress was negative for all compositions due to the tensile film stress with the maximum effect on fracture toughness at the lowest alumina compositions. The combination of the matrix stress and the film stress toughening increments was very low at the lowest alumina compositions; a large negative value indicating weakening (or lower final fracture toughness) of the film. At the high alumina compositions the combined stresses acted to produce in a relatively small positive incremental toughness.

Anneal Series

The same matrix stress and film stress models were applied to the eutectic composition (62.8 mol% or 65.7 vol%) using the measured particle sizes and spacing for the series of films annealed at 1500EC. Figure 69 shows the calculated toughening due to the matrix stress, film stress and their total. The incremental toughness from the matrix stress for these films was all positive and it increased as the particle size of the second phase increased. However the film stress caused a negative incremental toughness and decreased as the particle size increased. The combined effect from these two stresses resulted in an overall increase in the incremental toughness as the particle size increased;

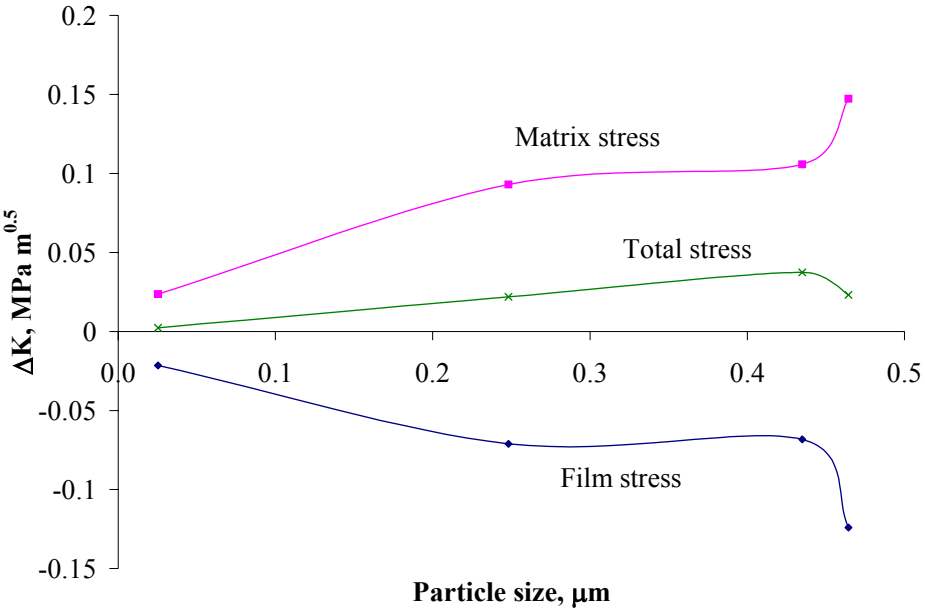

Figure 69 Model of incremental fracture toughness of matrix stress, film stress and their sum versus particle size for the 1500EC anneal series of 62.8 mol% Al_2O_3.

the total incremental toughness with this stress contribution is compared to the actual measurements later in this chapter.

Grain Bridging

The last factor included in the model for the fracture toughening of the thin films stems from the grain bridging phenomenon. This mechanism occurs where a second phase particle 'bridges' the crack and hinders the opening of the crack any further by the friction and adhesion of the particle with the matrix material, see Figure 70 [73]. There are several types of bridging mechanisms: ductile reinforcement, fiber or whisker reinforcement and large grains (or particles). The ductile reinforcement model was not applicable to this research since both phases present are brittle ceramics and the fiber

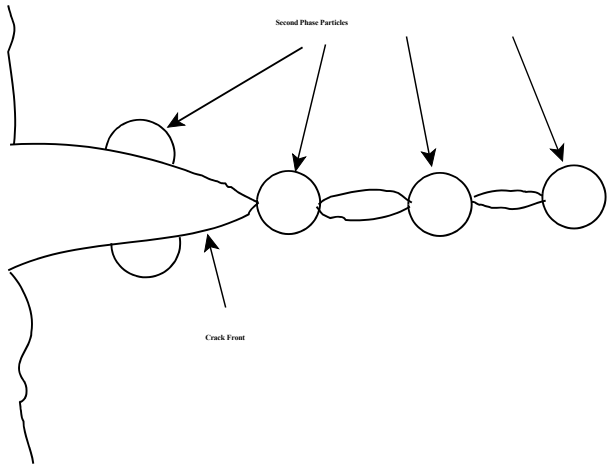

Figure 70 Schematic of the grain bridging toughening mechanism, where the crack is held together by the second phase particle or friction between the particle and the matrix.

(whisker) reinforcement model is applicable to only to short and continuous fiber composites.

The research for this thesis involved toughening by the addition of a brittle phase to another brittle phase. Several very detailed models for the fracture toughness effects of the bridging mechanism for ductile particles in a ceramic matrix exist; however there has not been much modeling of a brittle phase in brittle matrix. One model for grain bridging was developed by Shum [95] and has been used by several other researchers (e.g. Li et al. [3] and Becher [75]) for predicting the change in fracture toughness. The following expression used for this thesis was Shum's model for the incremental change in toughness due to grain bridging, ΔK_{GB} (MPa·m$^{0.5}$)

$$\Delta K_{GB} = 2.5 V_f E_p \left(\alpha_p - \alpha_m\right) \Delta T \left(\frac{d}{2}\right)^{1/2} \tag{62}$$

All of the terms in this equation have been defined in previous chapters. The expression for this mechanism is similar to that of the toughening due to residual stress; it is a function of the particle size but it is not a function of the particle spacing.

Anneal Series

Grain bridging was a possible mechanism involved in the annealed eutectic composition films. Figure 71 shows the modeled fracture toughness change due to grain bridging for these films. The incremental toughness was negative for this composition

because of the predicted local tensile stresses near the second phase particles. As the particle size increased the model shows a continued decrease because the predicted area of tensile stress increases with the particle size.

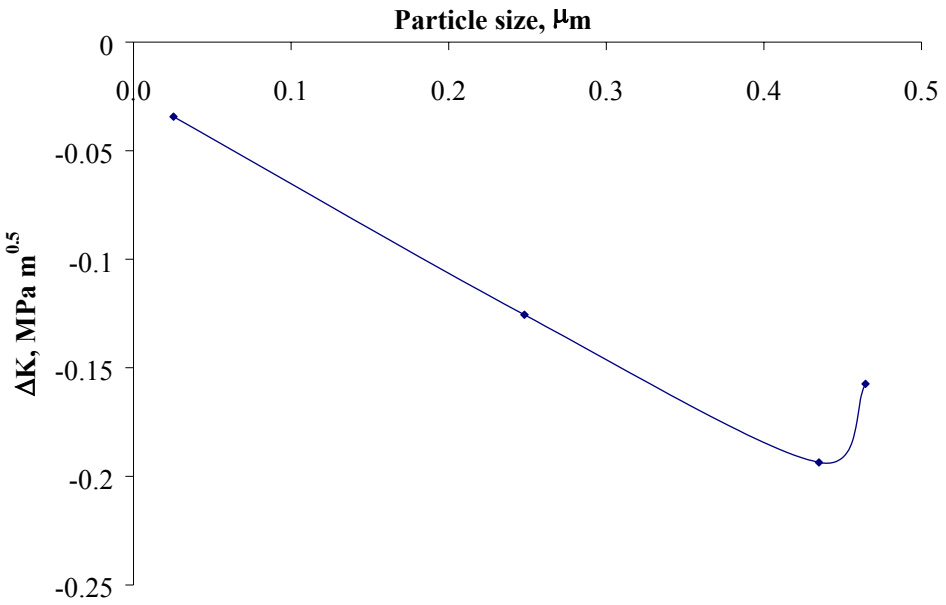

Figure 71 Model of incremental fracture toughness of grain bridging versus particle size for the 1500EC anneal series of 62.8 mol% Al_2O_3.

Compositional Study

The results of the grain bridging model for the full range of second phase compositions and various uniform particle sizes are shown in Figure 72. The incremental toughening is positive for alumina compositions up to 50 vol%. This region provides an increase in toughness due to the predicted local compressive stress near the second phase particles. This compressive stress acts to hold the particle by friction preventing further opening of the crack. For the alumina compositions above 50 vol% the incremental toughening is negative due to the predicted local tensile stress near the second phase particles. The large discontinuity is unreasonable for the actual film; it implies that grain bridging toughening does not fully explain the toughening involved with the second

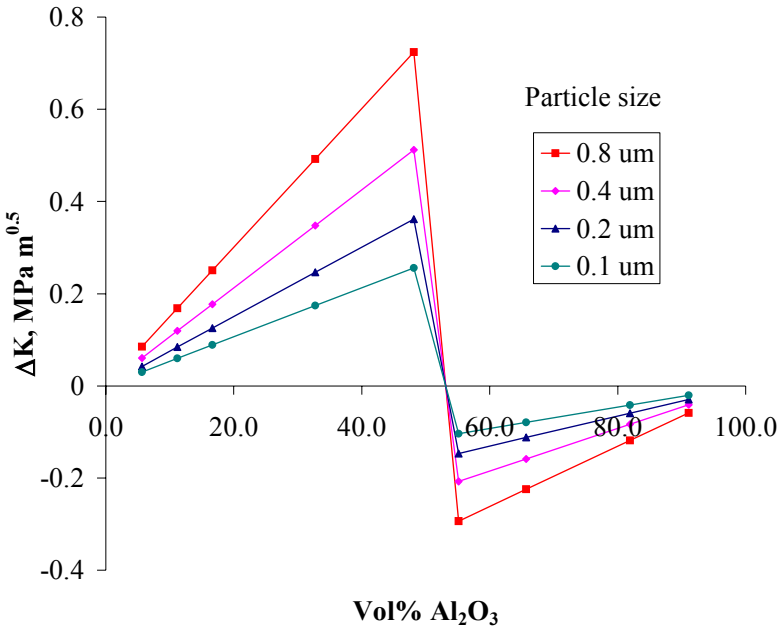

Figure 72 Model of incremental fracture toughness of grain bridging versus volume percent Al_2O_3 for various uniform particle sizes.

phase addition for these films. Additionally the actual films' particle sizes vary as the amount of alumina increases; this is shown in the following sections.

Using the actual particle sizes measured from the quantitative image analysis shown in Chapter IV produces the grain bridging results depicted in Figure 73. Similar to the uniform particle size plot, the incremental toughening for the measured particle sizes is positive for the low alumina compositions and negative for the high alumina compositions. Again this is due to the predicted compressive and tensile stresses, respectively, near the second phase particles.

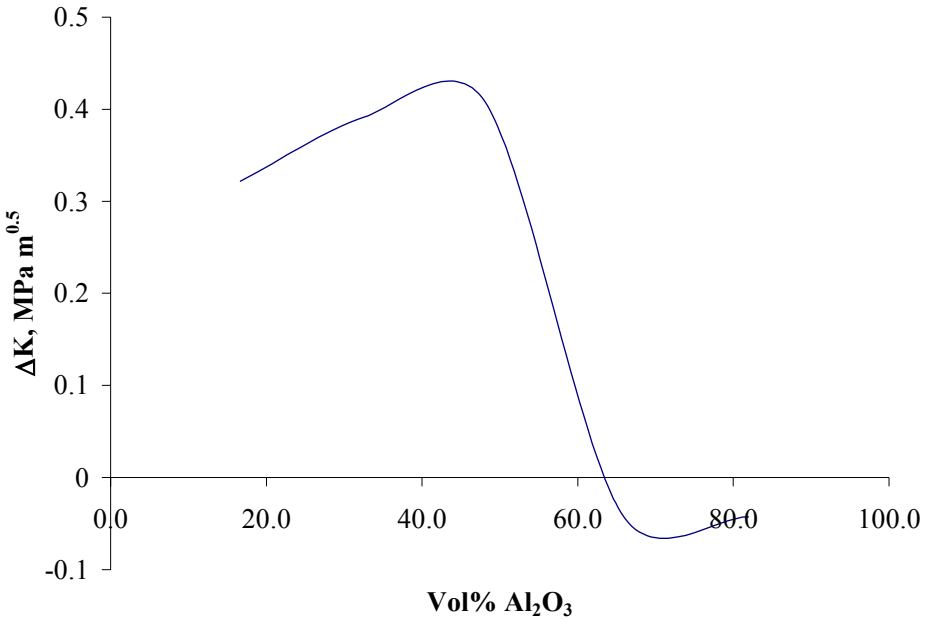

Figure 73 Model of incremental fracture toughness of grain bridging versus volume percent Al_2O_3 for measured particle sizes.

Model Total

The total fracture toughness model developed for this thesis was obtained by summing each of the toughening contributions from the various mechanisms detailed above. Equation (63) shows the sum of crack deflection, ΔK_{FE}, residual stress from both matrix stress and film stress, ΔK_{σ}, and grain bridging, ΔK_{GB}.

$$\Delta K_{total} = \Delta K_{FE} + \Delta K_{\sigma} + \Delta K_{GB} \tag{63}$$

The error bars on the model come from the possible range of substrate temperatures at which the depositions were made (750 to 950EC) and the range of different values provided in the literature for the various materials properties used in the model, E, v, and CTE. Table 15 shows the high, nominal and low values used in the model.

Anneal Series

For the annealed films the total toughness change is shown in Figure 74. This shows the general trend found in the measured data, however when both are plotted on the same axes, the magnitude of the slope of the model is substantially lower, Figure 75. The model is not as strong a function of the particle size as the measured toughness. One possible explanation for this large difference was that the anneal series consisted of only one specimen tested per anneal time. The repeatability for the annealed samples is not known. Another possibility is that the actual film stress is different than that determined from calculations; which may be reasonable because of the long anneal performed on these samples.

Table 15: Properties and Parameters Used in the Model

Property/Parameter	Low	Nominal	High
$\nu_{Al_2O_3}$	0.26	0.27	0.32
ν_{YSZ}	0.23	0.31	0.32
$E_{Al_2O_3}$, GPa	365	380	460
E_{YSZ}, GPa	151	200	220
CTE $_{Al_2O_3}$, x10^{-6} EC^{-1}	6.8	7.9	8.0
CTE $_{YSZ}$, x10^{-6} EC^{-1}	10.0	10.4	10.6
T, EC	750	850	950

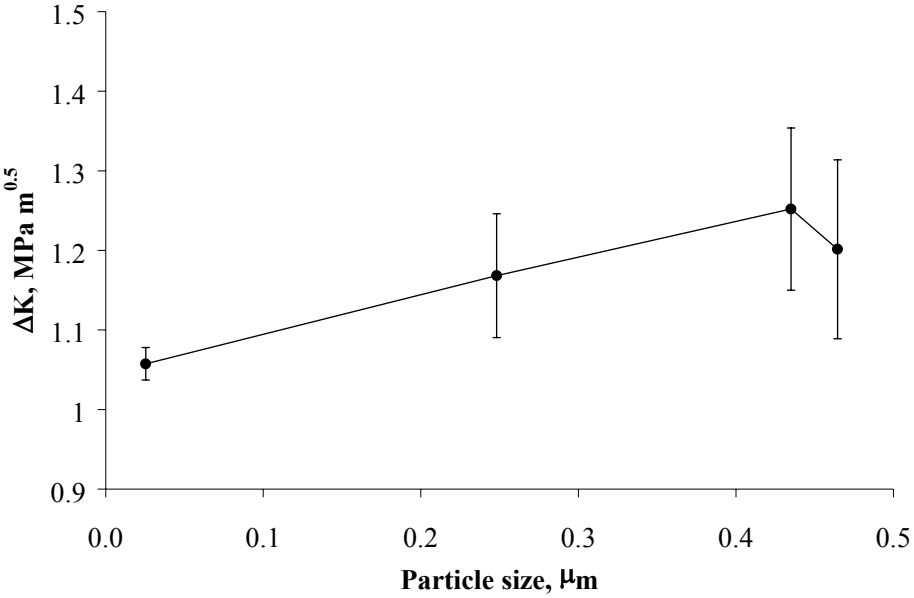

Figure 74 Total model of incremental fracture toughness versus particle size for the 1500EC anneal series of 62.8 mol% Al_2O_3.

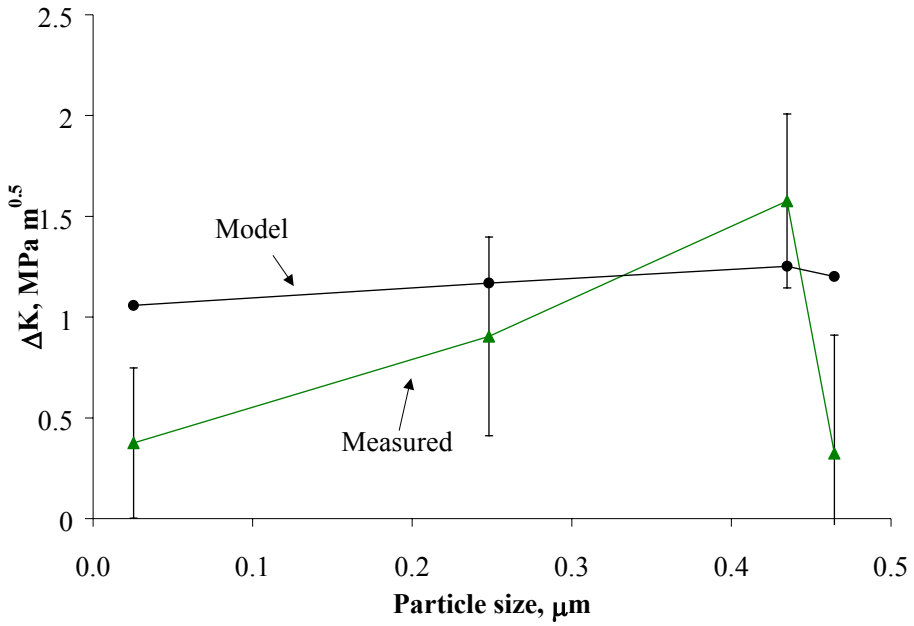

Figure 75 Total model of incremental fracture toughness and measured fracture toughness versus particle size for the 1500EC anneal series of 62.8 mol% Al_2O_3.

Compositional Study

The total model using uniform particle sizes and uniform spacing for the complete range of compositions is shown in Figure76 along with the measured toughening. This figure shows that the model agrees with the measured toughening for the high compositions of alumina, but it did not agree well for the low compositions of alumina. Substituting the distributed spacing crack deflection model into the total results in Figure 77. This model was closer to the measured toughening for the low alumina compositions but greater than the measured toughening for the high alumina compositions.

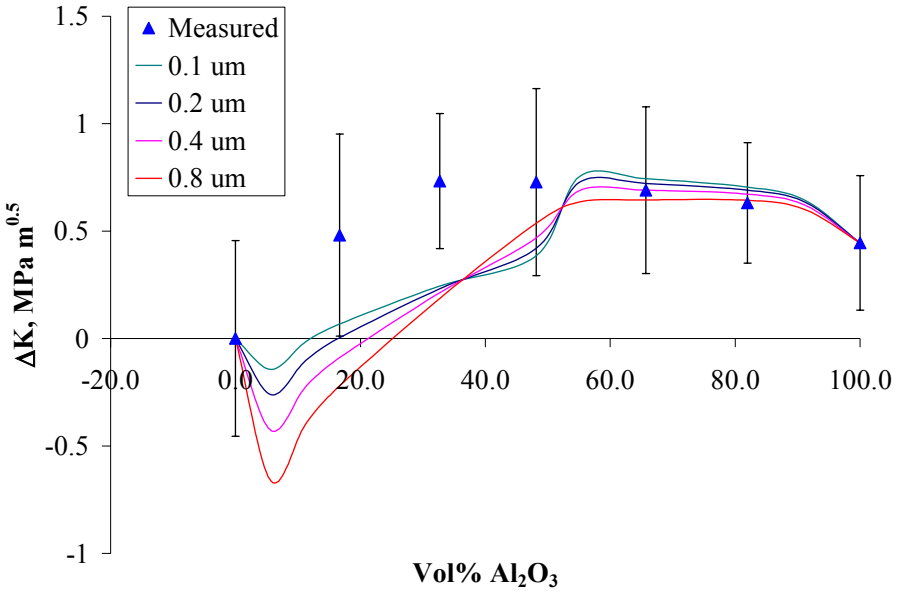

Figure 76 Total incremental fracture toughness model and measured toughening versus volume percent Al_2O_3 for uniform particle sizes and spacings with uniform spacing crack deflection model.

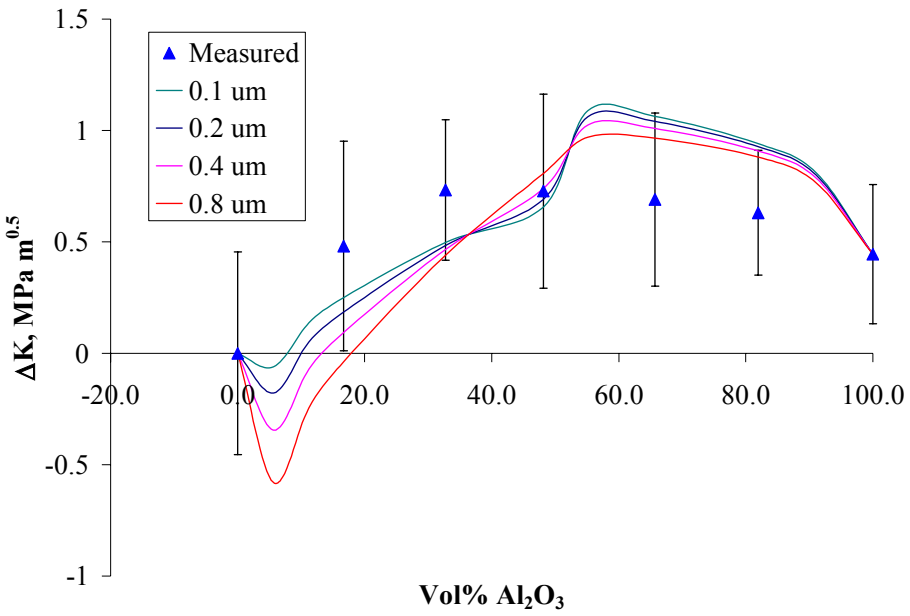

Figure 77 Total incremental fracture toughness model and measured toughening versus volume percent Al_2O_3 for uniform particle sizes and distributed spacing.

The total model using the measured particle size and spacing with the uniform spacing crack deflection model is shown in Figure 78. Similar to the model using the uniform particle size and uniform spacing, Figures 76 and 77, this model falls below the measured values in the lower alumina compositions while it is fairly close for the high alumina compositions. Using the measured particle size and spacing with the distributed spacing crack deflection model in the total model, Figure 79, shows close agreement in the low alumina compositions and poor agreement in the high alumina compositions.

An explanation for the low toughness prediction in the low alumina region for the model total with uniform spacing crack deflection, Figure 78, may be due to the

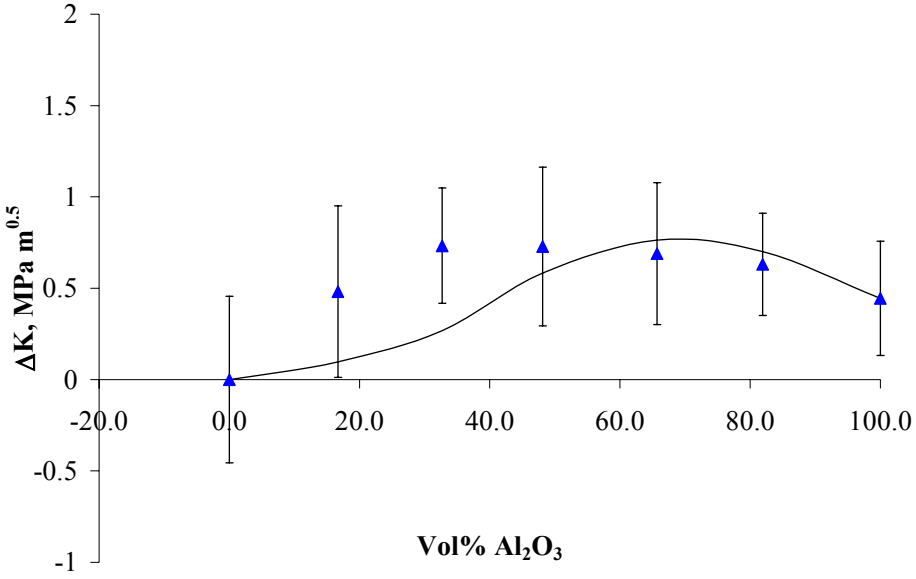

Figure 78 Total incremental fracture toughness model and measured toughening versus volume percent Al_2O_3 for measured particle sizes and spacings with the uniform-spacing crack deflection model.

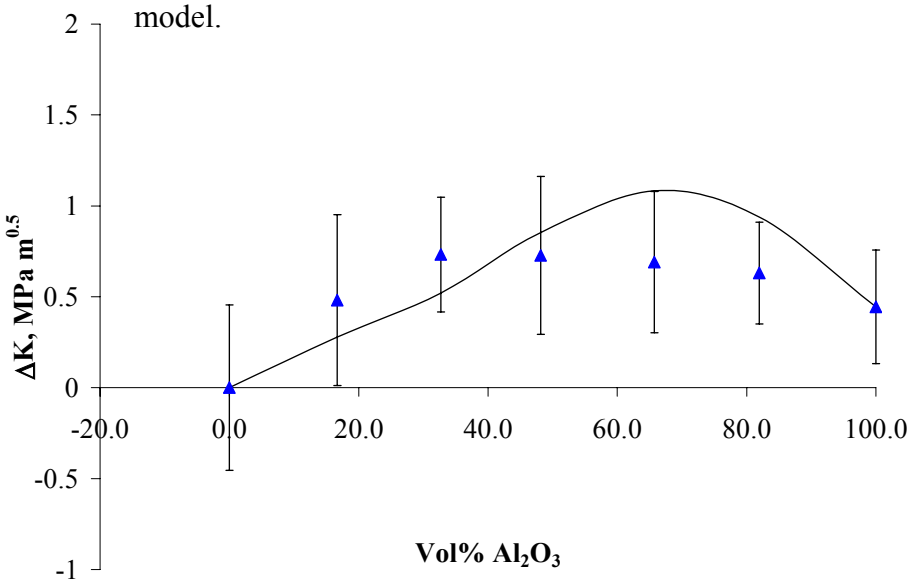

Figure 79 Total incremental fracture toughness model and measured toughening versus volume percent Al_2O_3 for measured particle sizes and spacings with the distributed-spacing crack deflection model.

assumption of spherical particles of uniform spacing. Recall from the SEM imaging that the low alumina compositions' second phase was randomly distributed swirls and not spheres, while the high alumina compositions' second phase (YSZ) were observed as uniformly distributed spheres; no swirls were present. With the swirl microstructure it can be assumed that the tortuosity experienced by the crack would be greater than that for spherical particles. Therefore, because of the swirls, the low alumina compositions have more toughening of the film from crack deflection than that predicted by the uniform spacing case, but by how much is unknown.

The distributed spacing crack deflection model reflects a reasonable increase in toughness and its assumed microstructure more closely resembles that of the actual swirl microstructure than the uniform spacing's assumed microstructure. For these microstructural observations the distributed spacing crack deflection model was applied to the low alumina range and the uniform spacing crack deflection model was applied to the high alumina range, Figure 80. This version of the model resulted in a close agreement between the model total and the measured toughening.

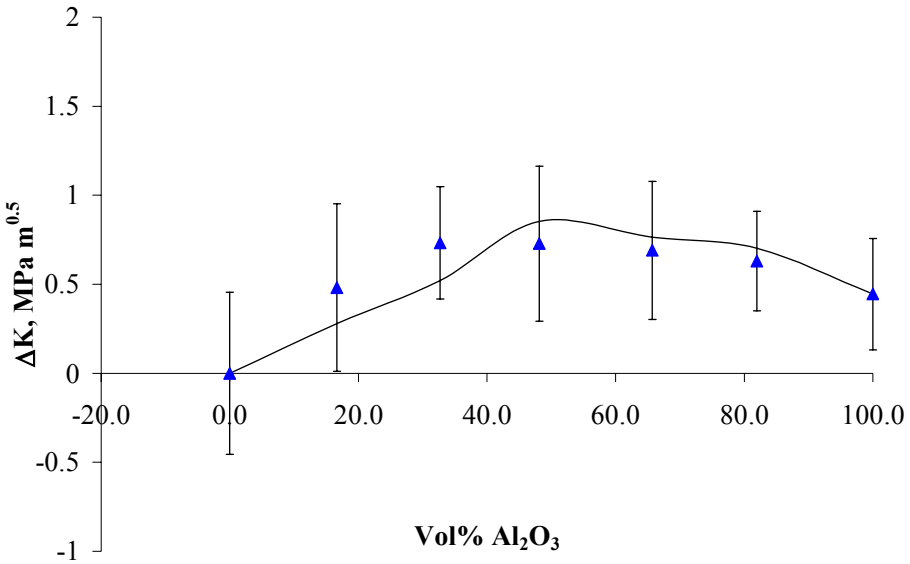

Figure 80 Total incremental fracture toughness model and measured toughening versus volume percent Al_2O_3 for measured particle sizes and spacings with the distributed-spacing crack deflection model (0-50 vol%) and the uniform-spacing crack deflection model (50-100 vol%).

CHAPTER VII

CONCLUSIONS

1. Yttria-stabilized zirconia-alumina composites can be deposited at the rate of ~ 1.5 μm/hr onto single crystal a-plane alumina substrates via combustion chemical vapor deposition using toluene as the flammable solvent with a Y 2-ethylhexanoate, Zr 2-ethylhexanoate and Al acetylacetonate as precursors in a concentration of 0.002 M.

2. The amounts of YSZ and alumina in the resulting combustion CVD YSZ-alumina films are equal to the stoichiometric amounts of YSZ and alumina in the precursor solutions.

3. A precursor amount of 4.5 mol% yttria results in approximately 6.8 mol% yttria in the final combustion CVD YSZ film.

4. Precursor solution concentrations of 0.002 M result in denser-appearing and smoother films than the higher concentration of 0.005 M with all other parameters constant.

5. Combustion CVD can be used to deposit YSZ particles sized 10 to 20 nm in diameter in an alumina matrix for the 62.8 mol% alumina composition.

6. Annealing the 62.8 mol% alumina film at temperatures up to 1500EC for up to 12 hrs has no detectible effect on the second phase (YSZ) particle sizes. Annealing the 62.8 mol% alumina film at 1500EC for as little as 2.5 hrs coarsens the microstructure.

7. Combustion CVD of YSZ-alumina films resulted in the formation of both the alpha and theta phases of alumina and the tetragonal phase of YSZ, although the cubic phase of YSZ could not be ruled out.

8. Nanoindentation for hardness and elastic modulus determination was a repeatable and reliable technique for bulk materials as verified by the small error bars and the repeatability of the results from multiple tests on the same material.

9. Nanoindentation for fracture toughness determination was a repeatable and reliable technique for bulk materials as verified by the repeatability of the results from multiple tests on the same material and by the consistent error bars comparable to those from large scale testing equipment (such as Vickers or Knoop indenters) on similar materials.

10. The fracture toughness of a-plane alumina was a function of the indenter tip orientation with respect to the primary cleavage plane of the alumina. The hardness and elastic modulus of a-plane alumina was not a function of indenter tip/crystal orientation.

11. Nanoindentation for hardness and elastic modulus determination for combustion CVD films is a feasible technique. The hardnesses and elastic moduli are less reliable for rougher coatings (roughnesses on the order of the indenter tip size) and for higher concentration precursor solutions. The 0.005 M solution produced films on which many indents (over 50% of the total) were unusable (i.e. discontinuous load-displacement curves) and the 0.002 M solutions produced films which had very few (less than 15% of the total) unusable indents.

12. The resulting elastic modulus to hardness ratios for all the YSZ-alumina films grown by combustion CVD were approximately 20 to 25 regardless of the differences in the deposition parameters and the nature of the load-displacement curves.

13. Nanoindentation for fracture toughness determination was a feasible, repeatable and reliable technique for combustion CVD films as verified by the repeatability of the results from tests on multiple specimens of the same film composition and the magnitude of their error bars. Repeatability was shown for the 100% YSZ films and 70 mol% YSZ/30 mol% alumina films. Additionally, the fracture toughnesses of the combustion CVD 100% YSZ films were comparable to literature values of conventional CVD YSZ films.

14. Fracture toughness of the films was not a function of the applied load as long as the film and substrate were not penetrated to the extent that significant delamination of the film occured.

15. 1500EC anneals in air performed for 0, 2.5, 5 and 10 hrs on the eutectic composition (62.8 mol% alumina) film resulted in fracture toughnesses that varied with the particle size and spacing. Fracture toughness increased with annealing time (and particle size and spacing) up to 5 hrs. Anneal times greater than 10 hours coarsened the film so much that the fracture toughness decreased.

16. Second phase particles of alumina grown into a YSZ matrix via combustion CVD increases the fracture toughness of the films on average, from 1.8 ± 0.5 $MPa \cdot m^{0.5}$ for 100% YSZ to 2.5 ± 0.3 $MPa \cdot m^{0.5}$ for 70 mol% YSZ/30 mol% alumina. Similarly, second phase particles of YSZ grown into an alumina matrix also increased the fracture toughness on average, from 2.2 ± 0.3 $MPa \cdot m^{0.5}$ for 100% alumina to 2.5 ± 0.4 $MPa \cdot m^{0.5}$ for 37.2 mol% YSZ/62.8 mol% alumina. Similarly, second phase particles of YSZ grown into an alumina matrix via combustion CVD also increase the fracture toughness of the films.

17. Fracture toughness for the YSZ-alumina films can be modeled using expressions developed for the following toughening mechanisms: crack deflection from the second phase particles, grain bridging around the particles and residual stress from the CTE mismatch of film to the substrate and CTE mismatch from the particles to the matrix of the film.

CHAPTER VIII

RECOMMENDATIONS FOR FUTURE WORK

There are several areas where additional work could be performed. Some of these are as follows:

1. Relate the load-displacement curve for individual cracks to the crack growth characteristics for each particular indentation.

2. Relate mechanical properties to deposition temperature.

3. Measure the residual stress versus process parameters.

4. Perform depositions with a different yttria composition and compare the resulting morphologies and properties.

5. Measure the porosity (or density) of the films and relate it to the measured hardness, elastic modulus and fracture toughness.

6. Determine coarsening behavior versus composition.

7. Deposit films on a different substrate other than a-plane alumina and determine the film's morphologies and properties.

REFERENCES

1. R.W. Hertzberg, Deformation and Fracture Mechanics of Engineering Materials, New York: John Wiley & Sons, Inc, 1996, 129.

2. M. Ohring, Thin Film Materials Science, San Diego, CA: Academic Press, 1992, 177-186.

3. J. Li and R. Watanabe, Journal of the American Ceramic Society, 78 [4] (1995), 1079-1082.

4. H. Tsubakino and R. Nozato, Journal of the American Ceramic Society, 74 [2] (1991) 440-443.

5. J. Li and R. Watanabe, Journal of Materials Science Letters, 15 (1996), 1264-1266.

6. K. Tsukama and M. Shimada, Journal of Materials Science Letters, 4 (1985), 857-861.

7. T. Sato and M. Shimada, Journal of Materials Science, 20 (1985), 3988-3992.

8. H. Yao-Yong, G. Ji-Qiang and Z. Hong-Tu, Journal of Materials Science Letters, 6 (1987), 246-248.

9. A. T. Hunt, W. B. Carter and J. K. Cochran, Jr., Applied Physics Letters, 63 [2] (1993), 266-268.

10. G. W. Book, W. B. Carter, T. A. Polley and K. J. Kozaczek, Thin Solid Films, 287, (1996) 32-35.

11. W.B. Carter, J.M. Hampikian, S.H. Godfrey and T.A. Polley, Materials and Manufacturing Processes, 10 [5] (1995), 1007-1020.

12. W.B. Carter, G.W. Book, T.A. Polley, D.W. Stollberg and J.M. Hampikian, Thin Solid Films, 347 (1999), 25-30.

13. J. M. Hampikian, A. T. Hunt and W. B. Carter, Processing and Fabrication of Advanced Materials III, (1994), 345-354.

14. M.R. Hendrick, J.M. Hampikian and W.B. Carter, Journal of Electrochemical Society, 145 [8] (1998).

15. D.W. Stollberg, W.B. Carter and J.M. Hampikian, Surface & Coatings Technology, 94-95 (1997), 137-143.

16. G.W. Book, Ph.D. Dissertation, School of Materials Science and Engineering, Georgia Institute of Technology.

17. L. Wang, Ph.D. Dissertation, School of Chemistry and Biochemistry, Georgia Institute of Technology.

18. M. Koguchi, Y. Matsuda, E. Kinoshita and K. Hirabayashi, Japanese Journal of Applied Physics, 29 [1] (1990), L33-35.

19. J. McHale, R.W. Schaeffer, A. Kebede and J. Macho, Journal of Superconductivity, 5 [6] (1992), 511-518.

20. Coatings for High-Temperature Structural Materials, Washington, D.C.: National Academy Press, 1996.

21. A.H. Heuer, R. Chaim and V. Lanteri, Science and Technology of Zirconia III, Advances in Ceramics, Vol. 24, Columbus, OH: American Ceramic Society, 1988, 3-20.

22. T.K. Gupta, F.F. Lange and J.H. Bechtold, Journal of Materials Science, 13 (1978), 1464-1470.

23. A.H. Heuer, Science and Technology of Zirconia, Advances in Ceramics, Vol. 3, Columbus, OH: American Ceramic Society, 1981, 98-115.

24. R.A. Miller, J.L. Smialek and R.G. Garlick, Science and Technology of Zirconia, Advances in Ceramics, Vol. 3, Columbus, OH: American Ceramic Society, 1987, 252.

25. R.C. Garvie, R.H. Hannink and R.T. Pascoe, "Ceramic Steel?," *Nature* (London), 258 (1975), 703-704.

26. D.L. Porter and A.H. Heuer, Journal of the American Ceramic Society-Discussions and Notes, 60 [3-4] (1977), 183-184.

27. R.M. McMeeking and A.G. Evans, Journal of the American Ceramic Society, 65 [5] (1982), 242-246.

28. K. Muraleedharan, J. Subrahmanyam and S.B. Bhaduri, Journal of the American Ceramic Society, 71 [5] (1988), C226-C227.

29. S.P. Baker and W.D. Nix, Proceedings of SPIE, Optical Thin Films III: New Developments, 1323 (1990), 263-276.

30. W.C. Oliver, R. Hutchings and J.B. Pethica, Microindentation Techniques in Materials Science and Engineering, STP 889, P.J. Blau and B.R. Lawn, eds., (Philadelphia, PA: ASTM, 1986), 90-108.

31. B. Bhushan, V.S. Williams and R.V. Shack, Journal of Tribology, 110 (1988), 563-571.

32. J.B. Pethica, R. Hutchings and W.C. Oliver, *Phil. Mag.*, A48 (1983), 593.

33. D. Tabor, The Hardness of Metals, Oxford, UK: Clarendon, 1951.

34. D.A. Hardwick, Thin Solid Films, 154 [1-2] (1987), 109-124.

35. W.C. Oliver and G.M. Pharr, Journal of Materials Research, 7 [6], Jun 1992, 1564-1583.

36. W.D. Nix, Metallurgical Transactions, 20A [11] (1989), 2217-2245.

37. A.V. Kulkarni and B. Bhushan, Thin Solid Films, 290-291 (1996), 206-210.

38. I.N. Sneddon, Int. J. Engng. Sci. 3 [47] (1965).

39. Nanoindenter® II Operating Instructions, Nanoinstruments of MTS, Oak Ridge, TN

40. Y. Tsukamoto, H. Yamaguchi and M. Yanagisawa, Thin Solid Films, 154 [1-2] (1987), 171-181.

41. D.T. Quinto, G.J. Wolfe and P.C. Jindal, Thin Solid Films, 153 (1997), 19-36.

42. T.C. Chou, T.G. Nieh, S.D. McAdams and G.M. Pharr, Scripta Metallurgica, 25 [10] (1991), 2203-2208.

43. T.J. Bell, J.S. Field and M.V. Swain, Materials Forum, 17 [2] (1993), 127-138.

44. K. Hjort, F. Ericson, J.-D. Schweitz, C. Hallin and E. Janzén, Thin Solid Films, 250 [1-2] (1994), 157-163.

45. V.A.C. Haanappel, D.v.d. Vendel, H.S.C. Metselaar, H.D. van Corbach, T. Fransen and P.J. Gellings, Thin Solid Films, 254 [1-2] (1995), 153-163.

46. J.L. Loubet, J.M. Georges, J.M. Marchesini and G. Meille, Journal of Tribology, 106 (1984) 43-48.

47. B.R. Lawn, A.G. Evans and D.B. Marshall, Journal of the American Ceramic Society, 63 (1980), 574.

48. D.S. Harding, W.C. Oliver and G.M. Pharr, Materials Research Society Symposium Proceedings, Thin Films: Stresses and Mechanical Properties V, 356 (1995), 663-668.

49. A. Kant, M.D. Drory and R.O. Ritchie, Materials Research Society Symposium Proceedings, Mechanical Behavior of Diamond and Other Forms of Carbon, 383 (1995), 289-294.

50. M.P. De Boer and W.W. Gerberich, Acta Materialia, 44 [8] (1996), 3177-3187.

51. E.R. Weppelmann, X.-Z. Hu and M.V. Swain, Journal of Adhesion Science and Technology, 8 [6] 3 (1994), 611-624.

52. R.L. Coble and W.D. Kingery, Journal of the American Ceramic Society, 39 [11] (1956), 377-85. 294

53. M. Yoshimura and S. Somiya, "Zirconia", Fine Ceramics Jiten., The Ceramic Society of Japan, Tokyo, Japan, (1987), 207-35.

54. M. Taya, S. Hayashi, A. S. Kobayashi and H. S. Yoon, Journal of the American Ceramic Society, 73 [5] (1990), 1382-1391.

55. S. Godfrey, M.S. Thesis, School of Materials Science and Engineering, Georgia Institute of Technology, Dec 1995.

56. M. R. Hendrick, M.S. Thesis, School of Materials Science and Engineering, Georgia Institute of Technology, May 1996.

57. H. Toraya, Journal of the American Ceramic Society, 72 [4] (1989), 662-664.

58. R.P. Ingel and D. Lewis, Journal of the American Ceramic Society, 69 [4] (1986), 325-332.

59. V. Lanteri, A.H. Heuer and T.E. Mitchell, Science and Technology of Zirconia II, Advances in Ceramics, Vol. 12, Columbus, OH: American Ceramic Society, 1984, 118-130.

60. E.E. Underwood, Quantitative Stereology, Reading, Mass.: Addison-Wesley Publishing Co., 1970.

61. G.M. Pharr, D.S. Harding and W.C. Oliver, Mechanical Properties and Deformation Behavior of Materials Having Ultra-Fine Microstructures, M. Nastasi, D.M. Parkin and H. Gleiter, Eds., NATO ASI Series, Series E: Applied Sciences, Vol 233, 1993, 449-462.

62. Matroc, Morgan Advanced Ceramics, 582 Monastery Dr, Latrobe, PA 15650.

63. Guide to Engineered Materials, Advanced Materials & Processes, M.W. Hunt ed., Materials Park, OH, 156 [6], December 1999, 143.

64. W.D. Kingery, H.K. Bowen and D.R. Uhlmann, Introduction to Ceramics, New York, NY: John Wiley & Sons, 1976.

65. Atlantic Equipment Engineers, 13 Foster St, Bergenfield, NJ, 07621.

66. D.G. Isaak, O.L. Anderson, and T. Goto, Physics and Chemistry of Minerals, 16 (1989), 704-713.

67. A. G. Evans, A. H. Heuer and D. L. Porter, Fracture, 1 (ICF4), Waterloo, Canada, Jun 19-24, 1977, 529-556.

68. N. Claussen, J. Steeb and R. F. Pabst, American Ceramic Society Bulletin, 56 [6] (1977), 559-562.

69. X. Li, D. Diao and B. Bhushan, Acta Metallurgica, 45 [11] (1997), 4453-4461.

70. Private Conversation with J.K. Cochran, Ph.D., School of Material Science and Engineering, Georgia Institute of Technology, Atlanta, GA.

71. S. Suresh and A. E. Giannakopoulos, Acta Metallurgica, 46 [16] (1998), 5755-67.

72. G. M. Pharr, T. Y. Tsui, A. Bolshakov and W. C. Oliver, Materials Research Society Symposium Proceedings, 338 (1994), 127-134.

73. A.G. Evans, Journal of the American Ceramic Society, 73 [2] (1990), 187-206.

74. D.R. Clarke and K.T. Faber, Journal of Physics and Chemistry of Solids, 48 [11] (1987), 1115-1117.

75. P. F. Becher, Journal of the American Ceramic Society, 74 [2] (1991), 255-69.

76. A. K. Khaund, V. D. Krstic and P. S. Nicholson, Journal of Materials Science, 12 (1977), 2269-2273.

77. K. T. Faber and A. G. Evans, Acta Metallurgica, 31 [4] (1983), 565-576.

78. K. T. Faber and A. G. Evans, Acta Metallurgica, 31 [4] (1983), 577-584.

79. K.T. Faber and A.G. Evans, Communications of the American Ceramic Society, (Jun 1983), C-94-C-96.

80. C.L. Conner and K.T. Faber, Journal of Materials Science, 25 [6] (Jun 1990), 2737-2742.

81. G. C. Wei and P. F. Becher, Journal of the American Ceramic Society, 67 [8] (1984), 571-574.

82. G. DePortu, C. Fiori and O. Sbaizero, Science and Technology of Zirconia III, Advances in Ceramics, Vol. 24B, Columbus, OH: American Ceramic Society, 1988, 1063-1073.

83. N. P. Padture, J. L. Runyan, S. J. Bennison, L. M. Braun and B. R. Lawn, Journal of the American Ceramic Society, 76 [9] (1993), 2241-47.

84. B. R. Lawn, N. P. Padture, L. M. Braun and S. J. Bennison, Journal of the American Ceramic Society, 76 [9] (1993), 2235-40.

85. H. Cai, B. Moran and K.T. Faber, Journal of the American Ceramic Society, 74 [7] (1991), 1695-1698.

86. D.J. Magley, R.A. Winholtz and K.T. Faber, Journal of the American Ceramic Society, 73 [6] (1990), 1641-1644.

87. W.-H. Gu, K.T. Faber and R.W. Steinbrech, Acta Metallurgica et Materialia, 40 [11] (Nov 1992), 3121-3128.

88. W.-H. Gu and K.T. Faber, Journal of the American Ceramic Society, 78 [6] (1995), 1507-1512.

89. K.T. Faber, T. Iwagoshi and Ghosh, Communications of the American Ceramic Society, (Sep 1988), C-399-C-401.

90. H. Cai, K.T. Faber and E.R. Fuller, Journal of the American Ceramic Society, 75 [11] (1992), 3111-3117.

91. T.E. Steyer and K.T. Faber, Journal of the American Ceramic Society, 78 [10] (1995), 2673-2679.

92. H. Cai and K.T. Faber, Scripta Metallurgica et Materialia, 28 [9] (1993), 1161-1166.

93. G.R. Irwin, Hanbuch der Physik, Vol. VI (Edited by Flugge S.) Springer-Verlag, Berlin (1958).

94. J.D. Eshelby, Proceedings of the Royal Society London, A, 241 (1957), 376-96.

95. W. Shum, "Bridging Effects on Toughness", Ph.D. Thesis, Harvard University, Cambridge, MA, (1989).